JOURNAL OF CAVE AND KARST STUDIES

December 2023
Volume 85, Numbers 3-4
ISSN 1090-6924
A Publication of the National Speleological Society

DEDICATED TO THE ADVANCEMENT OF SCIENCE, EDUCATION, EXPLORATION, AND CONSERVATION

Published By
The National Speleological Society

http://caves.org/pub/journal

Office
6001 Pulaski Pike NW
Huntsville, AL 35810 USA
Tel:256-852-1300
nss@caves.org

Editor-in-Chief
Malcolm S. Field
Washington, DC
703-347-8601
field.malcolm1@gmail.com

Production Editor
Scott A. Engel
Knoxville, TN
225-281-3914
saecaver@gmail.com

Copyeditor
Bert Ashbrook
caving.ashbrook@comcast.net

The *Journal of Cave and Karst Studies* , ISSN 1090-6924, CPM Number #40065056, is a multi-disciplinary, refereed journal published four times a year by the National Speleological Society. The *Journal* is available by open access on its website, or check the website for current print subscription rates. Back issues are available from the NSS office.

POSTMASTER: send address changes to the National Speleological Society Office listed above.

The Journal of Cave and Karst Studies is covered by the following ISI Thomson Services Science Citation Index Expanded, ISI Alerting Services, and Current Contents/Physical, Chemical, and Earth Sciences.

Front Cover: East Crater Cave, Mount Rainier, Washington, USA. See Stenner et al in this issue.

Christian Stenner, Lee J. Florea, Andreas Pflitsch, Eduardo Cartaya, David A. Riggs. Morphodynamics of glaciovolcanic caves—Mount Rainier, Washington, USA. *Journal of Cave and Karst Studies*, v. 85, nos. 3/4, p. 65-85. DOI:10.4311/2021EX0131

MORPHODYNAMICS OF GLACIOVOLCANIC CAVES – MOUNT RAINIER, WASHINGTON, USA

Christian Stenner[1,C], Lee J. Florea[2], Andreas Pflitsch[3], Eduardo Cartaya[4], and David A. Riggs[4]

Abstract

The twin summit craters of Mount Rainier, Washington, USA host the largest known glaciovolcanic caves in the world and at 4382 m, the highest elevation caves in the USA. The caves are formed in ice at the glacier-rock interface by volcanogenic gases and atmospheric advection. However, the way in which discrete caves are formed and evolve remains poorly understood. Surveys of the cave systems in 1970−1973 and 1997−1998 in both the West and East Craters documented cave passage morphology. Field expeditions from 2014−2017 comprehensively surveyed the Rainier summit caves and undertook thermal imaging and temperature monitoring. Significant changes had occurred. In the East Crater, documented cave length has nearly doubled since 1973 to 3593 m of passage spanning 144 m of depth, revealing a new subglacial lake, and now nearly circumnavigating the East Crater. Of the reported increase in length, some 600 m of the mapped passage is possibly newly formed. Across 47 years of observation, certain sections of the cave appear to be preserved in form and position through time, while others are more actively being lost or forming. Conserved passages are generally sub-horizontal, passages following the curvilinear crater contours, show low temperature variability, and are dependent on perennial fumarolic activity or distributed heat flux emanating from warm bedrock and sediment floors. Transient passages are smaller diameter dendritic passages following the slope of the ice-rock interface towards entrance zones and normal to the circum-crater passage. They also show higher variability in temperature and airflow and are subject to seasonal weather and mechanical collapse, which may contribute to transience. Additional research is required to confirm the mechanisms maintaining conserved passages and formation of transient passages.

INTRODUCTION

Explorable cavities (caves) within glacier ice arise when processes of enlargement locally exceed those leading to closure over a sustained distance. Latent heat in the form of liquid water or water vapor and sensible heat (warm water or air) are the predominant drivers of enlargement. Persistent glacier caves are typically associated with meltwater streams in thin, uncrevassed ice. Studies of glacier caves allow direct observations from a subglacial viewpoint which can calibrate models of rates of glacial melt or movement, bedrock weathering and transport, and glacial outburst floods (Benn et al., 2009).

Volcanoes present a distinct environment where high altitude (or latitude) can permit glaciers, while geothermal heat can cause melting by conduction, fumarole emission, or water flow. A subset of caves formed where glacial ice melts from underlying volcanism, glaciovolcanic caves are rare environments. Curtis and Kyle (2017) reported that of 1443 known subaerial Holocene volcanic centers, 20.3 % (291) are glaciated or have permanent snowfields, while Edwards et al., (2020) identified 245 volcanic centers with potential for impacts from ice. Despite this glaciovolcanism potential, locations with glaciovolcanic caves are not well known at these thermal centers. A review by Sobolewski, et al. (2022a) found limited examples in published literature. Summarized, published studies include sites in Antarctica (Giggenbach, 1976) and both the summit (Kiver and Mumma, 1971; Kiver and Steele, 1975) and Paradise Ice Field (Anderson et al., 1994) of Mount Rainier in Washington, USA (Halliday, 2007). Recent investigations have included discoveries at Mount St. Helens in Washington (Sobolewski, et al., 2022b; Anderson et al., 1998), additions to previous work at Mount Erebus in Antarctica (Curtis, 2010), the role of hydrothermal springs to the cave development at Mount Hood in Oregon (Pflitsch et al., 2017), and exploration on Mount Melbourne and Mount Rittman in Antarctica (Gambino et al., 2021). Curtis (2016) discussed global relevance of glaciovolcanic caves associated directly with fumaroles, derived from examples at Mount Erebus. A comparison of the cave systems compiled from published literature (Table 1) demonstrates the extent and location of the most prominent of the known examples.

The origin and shape of glaciovolcanic caves are intriguing; they originate from and are shaped by the balance between ice accumulation and ablation guided by variations in climate and volcanic heat flux. They are ephemeral landforms. At Mount Rainier, the Paradise Ice Caves disappeared when the ice field melted away from an area of thermal springs (Anderson et al., 1994). At Mount Hood, the Snow Dragon Cave System also largely disappeared as the Sandy Glacier retreated upslope of thermal springs (Pflitsch et al., 2017). In contrast, Crater Glacier and its associated caves

[1] Alberta Speleological Society, Calgary, Alberta, Canada
[2] Washington State Geological Survey, Department of Natural Resources, Olympia, Washington, USA
[3] Institute of Geography, Ruhr-University Bochum, Bochum, Germany
[4] Glacier Cave Explorers, Oregon High Desert Grotto of the National Speleological Society, Redmond, Oregon, USA
[C] Corresponding Author: cstenner@telus.net

Table 1. Comparison of known long and deep glaciovolcanic cave systems.

Cave System	Location	Length (m)	Depth (m)	Reference
East Crater Cave	Mount Rainier, USA	3593	144	Stenner et al., 2022
Mothra Cave	Mount St. Helens, USA	797	72	Unpublished result, 2022[a]
Rodan Cave	Mount St. Helens, USA	775	82	Sobolewski et al., 2022b
MC3 Ice Cave	Mount Melbourne, Antarctica	685	52	Liuzzo, et al., 2018
Warren Cave	Mount Erebus, Antarctica	524	23	Curtis, 2010; 2021[c]
Ghidorah Cave	Mount St. Helens, USA	434	30	Stenner et al., 2020
West Crater Cave	Mount Rainier, USA	308	33	Stenner et al., 2022
Crevasse Cave	Mount St. Helens, USA	276	56	Stenner et al., 2020
Hot Imagination Cave[b]	Mount Hood, USA	273	58	Pflitsch et al., 2017
MC1 Aurora Ice Cave	Mount Melbourne, Antarctica	223	35	Liuzzo, et al., 2018
The Igloo	Mount St. Helens, USA	191	8	Stenner et al., 2020
Kachina Cave	Mount Erebus, Antarctica	146	6	Curtis, 2010; 2021[c]
Snow Dragon System[b]	Mount Hood, USA	2185	292	Pflitsch et al., 2017
Mammoth/Cathedral[c]	Mount Erebus, Antarctica	···	···	Curtis, 2021
Anchor Cave[c]	Mount Erebus, Antarctica	···	···	Curtis, 2021

[a] As of July, 2022 (C. Stenner).
[b] Hot Imagination is a remnant of the Snow Dragon System which is now separately named. The Snow Dragon Cave system length and depth has been significantly reduced by glacial ablation since the reported survey from 2013.
[c] Mammoth/Cathedral system and Anchor Cave at Mount Erebus are likely the longest in the region but are not surveyed. They are reported to be less extensive than the Mount Rainier system (A. Curtis, personal communication, 2021).

in the crater of Mount St. Helens experienced cycles of expansion following the 1980−1986 (Anderson et al., 1998) and 2004−2008 lava dome emplacements (Stenner et al., 2020; Sobolewski et al., 2023). At Crater glacier, persistent low temperature fumaroles combined with glacial expansion contribute to ongoing cave development (Sobolewski et al., 2022b).

Our understanding of glaciovolcanic caves pales in comparison to caves in carbonate rocks (Ford and Williams, 2007), lava tubes (Sauro, et al., 2022; Holler, 2019 p. 836−849), or englacial conduits (Gulley and Fountain, 2019, p. 468−473). Rather, most studies are descriptive or taxonomic and do not focus on process. They represent iterative snapshots of a rapidly evolving environment in the cryosphere, with the six-year-long study on a single glaciovolcanic cave chamber of Mount Erebus (Curtis, 2016) representing the benchmark longitudinal study.

Glaciovolcanic cave morphodynamics suggested as an indicator for volcanic activity (Curtis, 2016; Zimbelman et al., 2000) remains an unproven hypothesis. Six years of observation in Warren Cave at Mount Erebus could not link dynamic morphology to changes in volcanic activity (Curtis, 2016). Rather, Curtis (2016) suggested that new glaciovolcanic cave development may indicate subnivean volcanic unrest. A recent example of glaciovolcanic cave genesis in the glacier at Mount Meager, Canada have raised concerns about renewed volcanic hazards (Roberti, 2018; Unnsteinsson, 2022).

Studies thus far demonstrate persistent warm gas emissions from fumaroles and spatial discrete air movement by convection or advection distribute heat from point sources along cave passages (Curtis and Kyle, 2011). Analytical and numerical modeling of glaciovolcanic void formation fitted functions of glacier thickness, heat flux, vertical ice velocity, and bed slope to the height of a void (Unnsteinsson, 2022). Suppression or closure of voids is predominantly due to ice flow (creep) (Unnsteinsson, 2022) or mechanical collapse (Sobolewski, et al., 2022b). However, results from glaciovolcanic cave studies have yet to understand and classify cave geometry and potential variability.

Table 1 reveals the disparity between the Mount Rainier cave system and others; it offers an extensive setting to observe glaciovolcanic processes among the limited known examples. Here, mapping and monitoring of glaciovolcanic caves on Mount Rainier are used to see if configuration changes at a decadal time scale.

PHYSICAL SETTING

Mount Rainier formed through successive eruptions over the past 840 ka; the current East and West Craters are nested in the remnants of an older and higher edifice that collapsed approximately 540 ka ago. Eruptions are documented throughout the Holocene along with recent activity in the 19th Century. Evidence of magmatic eruption from 1 ka BP exists while observers reported the most recent eruption in December 1894; this may have impacted summit ice though confirmation is lacking (Sisson and Vallance, 2009). A prior verifiable eruption impacting summit ice occurred between 1820 and 1840 along with observations of a subaerial crater lake (Frank, 1995). Past impacts to the surround-

ings include extensive lahars of up to 3 × 10^9 m^3 (Crandell, 1971; Scott et al., 1995) with the Osceola mudflow being the largest one in the volcano´s recent history (Vallance and Scott, 1997). An extensive glacial system is supported on the volcano flanks, however glacial ice volume has reduced 25 % overall since 1913, while 14 % volume loss occurred between 1970 and 2008, as mean annual temperatures increased and snowfall decreased (Hoffman et al., 2014, Nylen, 2004; Sisson et al., 2011).

With increasing glacial melt observed at Rainier comes the potential for enhanced hydrothermal activity as active snow and ice melt at the summit craters and alteration product deposition (Frank, 1995; Korosec, 1989) lead to increased bedrock alteration, weakening slope stability, leading to mass wasting (Finn et al., 2001). The culminating effects of reduced glacial mass and edifice stability may increase the probability of eruption (Capra, 2008; Tuffen, 2010). More than 100 fumaroles, driven by hydrothermal cycling of glacial melt, presently exist under the summit ice plugs and flanking glaciers (Frank, 1995). As a consequence, Mount Rainier has a need for increased hydrothermal and fumarole monitoring (National Research Council, 1994). Potential impact to nearby populations due to lahars, amongst other hazards, resulted in Mount Rainier's designation as a Decade Volcano in 1987 by the International Association of Volcanology and Chemistry of the Earth's Interior and a high risk site in the United States Geological Survey (USGS) National Volcanic Early Warning System (Ewert et al., 2018).

Glaciovolcanic Caves – Mount Rainier

The twin summit craters of Mount Rainier house the East Crater and West Crater Caves, the East Crater Cave being the longest and deepest known (Table 1; Fig. 1). These were first identified during the 1870 summit climb by Van Trump and Stevens (Stevens, 1876). Whittaker (1957) described his entry into the caves in 1954. Whittaker and Nelson

Figure 1. Base map of the Pacific Northwest, United States of America showing location of Mount Rainier and other Cascade volcanoes. Inset image of the surveyed extent of the East and West Crater cave system passages at the summit of Mount Rainier, marked in red and blue and overlaid on GIS satellite imagery (ESRI and Google Earth).

returned in 1970 and made a traverse to a second exit (Wilkins, 1970) and produced the first known grade 1 sketch (Fig. 2a). Project Crater (Kiver and Mumma, 1971; Lokey et al., 1972; Lokey, 1973) conducted a geophysical study and mapping effort of the East and West craters from 1970−1973 and produced the first detailed planform cave maps (Figs.

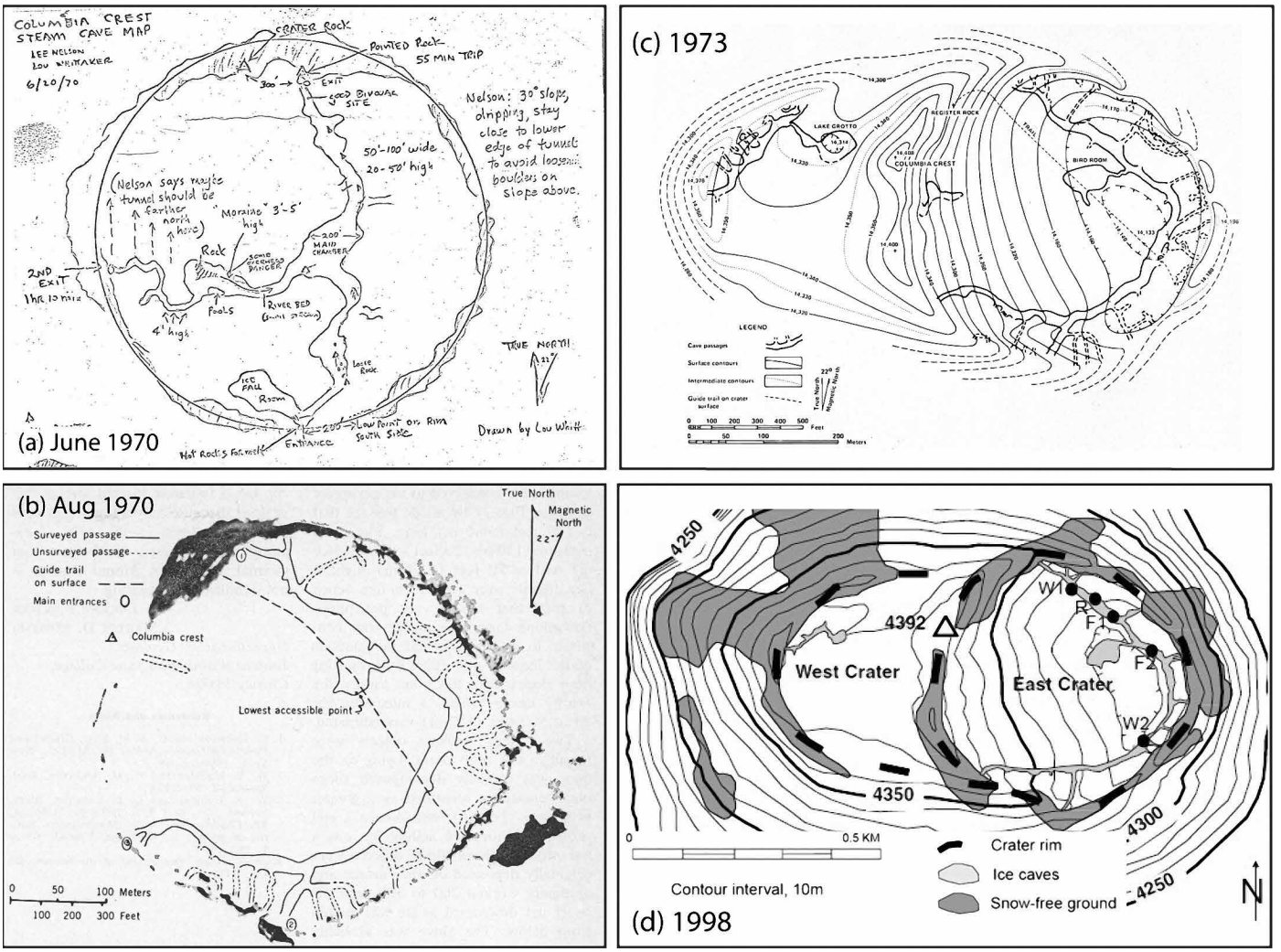

Figure 2. Historical planform surveys used for comparative analysis. (a) Grade 1 survey of East Crater Cave by Nelson and Whittaker (1970). (b) Survey reported in Kiver and Mumma (1971). (c) Surveys of East Crater Cave and West Crater Caves from Kiver and Steele (1975), and (d) Surveys of East Crater Cave and West Crater Caves from Zimbelman, et al., (2000).

2b and c) comprising 1800 m in the East Crater and 305 m of passages in the West Crater, including Lake Muriel below the West Crater ice (Kiver and Steele, 1975). These first tripod mounted compass surveys provide a baseline for comparisons. In 1997, a team of USGS and National Park Service scientists conducted studies (Le Guern et al., 2000; Zimbelman et al., 2000), and produced a fourth map iteration that included 700−1500 m of passage in the East Crater Cave and 155 m of passage in the West Crater Cave, (Fig. 2d).

We conducted sequential studies in the craters of Mount Rainier from 2015−2017. In August 2015, an expedition of 16 stayed on the summit for 9 days to study and map the East and West Crater Caves. In East Crater, 3170 m of passage were surveyed spanning 112 m of depth. In the West Crater, high CO_2 concentrations limited exploration to 137 m of surveyed passage. With over 50 personnel transporting gear and conducting studies on climatology, geochemistry, hydrology, microbiology, and glaciology, the 2015 expedition was the largest known operational event to occur in the history of Mount Rainier National Park (Cartaya, 2016). A smaller, five-day summit expedition in July−August 2016 placed and downloaded data from dataloggers, measured passage volume, collected thermal images, and monitored gas readings.

In July−August 2017, an expedition of 14 returned to the summit to support cave survey and research in climatology, geochemistry, as well as tests by NASA Jet Propulsion Laboratory of prototype robotic technologies for ice climbing and core sampling, given the utility of the cave as an ocean world analog. Eighty personnel were involved, carrying

680 kg of equipment to the summit and back over a span of 13 days. A replicate survey in the East Crater Cave included remaining leads, such as the Bird Room, the deepest point. In the West Crater, the cave was fully explored using Self-Contained Breathing Apparatus (SCBA). (Stenner, et al., 2022). A companion paper to this study, Stenner et al. (2022), discussed hazardous atmospheres due to fumarolic degassing in the Mount Rainier system, whereby turbulent and convectively rising gas and vapor plumes from the subglacial fumarole vents circulate within the cave system and cause CO_2 accumulations.

Mount Rainier Cave Morphodynamics and Volcanic Activity

Depictions of geometric changes have been proposed as indicators of volcanism in the Mount Rainier caves but have been anecdotal (e.g., Anon, 1972). Kiver and Steele (1975) noted enlargement of the cave passages over four years and suggested the system may not be in equilibrium, and that changes may be a normal condition. They proposed that changes in summit thermal activity would cause corresponding changes in cave passage location, size, and morphology, accompanied by an increase in micro-seismic activity. Hoblitt et al. (1998) noted a reawakening Mount Rainier would cause increased gas emissions in the caves. Zimbelman, et al., (2000, p. 462) further noted that "Because the caves act as condensers, traps, and calorimeters for magmatic volatiles and heat, their characterization and monitoring may represent powerful potential indicators of changes in the hydrovolcanic system which may not be readily apparent by surface surveys."

More recently Florea et al., (2021), using a year of continuous monitoring data, identified a dynamic equilibrium of the Rainier summit caves responding to seasonal weather patterns and temperature changes. During winter storms, entrances seal and advection diminishes, leading to increased temperatures and subglacial melt until entrances re-open. These observations lead to a hypothesis that changes in passage position and morphology are present in the dynamic equilibrium of the Mount Rainier cave system, but observable only over longer timescales.

In this study, we compare data from a review of literature and historical cave surveys on the Rainier summit to our most recent cave passage and fumarole location survey, passage ablation measurements, and vertical ice movement measurement to quantify passage characteristics and the potential degree and magnitude of change through time. This multi-decadal (47 year) comparison is the first of which we are aware and aims to add to our understanding of the morphodynamics of an understudied subset of speleology. Using available preliminary temperature and thermography data we support the comparison and discussion on mechanisms of observed changes. Our results lead toward a model for the origin and morphology of glaciovolcanic caves applicable to other glacial-mantled volcanic edifices.

METHODS

Survey and Cartography

Tacheometric cave surveying methods used fixed stations to map passage extent, cross-section, datalogger locations, ablation markers, fumaroles, and cave entrances during 2015−2017 fieldwork. In-cave reference stations provided fixed locations for connecting annual surveys. Nine surface stations at entrances were referenced using global navigation satellite systems (GNSS). A transect survey over the glacier surface from the Guide Rocks entrance to the crater rim adjacent to the Misery Crawl entrance connected ice surface elevation to the cave survey. All survey data were collected using calibrated DistoX2 (a custom Leica A3 rangefinder modified to provide distance, azimuth, and inclination) paired with a Windows Mobile Dell Axim X51 Personal Digital Assistant (PDA) using PocketTopo software (e.g., Heeb, 2009; n.d.).

Several challenges inhibited efficiency, and potentially, accuracy in this study. First, survey stations on unstable rocks disappeared between study years, as rocks themselves had fallen down passages or having degraded in the harsh environment, requiring creation of new stations. As mitigation, 1.5 mm × 6 mm aluminum rivets were installed in rocks with a reflective tag at nine stations. Next, visibility in the caves was sometimes obscured by thick steam from fumaroles, limiting DistoX2 measurements for passage cross section and volume. Additionally, volcanic boulders rich in mafic minerals caused magnetic interference and deflected azimuth measurements by up to 15 degrees, requiring offset (floating) stations as mitigation.

After reviewing the raw data, we calculated passage cross section and volume in East Crater Cave using the splay shots radiating from two recoverable reference stations at repeatable azimuths and inclinations in 2016 and again in 2017 (Fig. 3). Of the 195 splay shots at these reference locations, 53 were within a 1.5-degree range of their previous companion measurement and considered suitable for comparison.

Post processing of 2015−2017 survey data used Compass cave survey management software (Fish, 2020). Loop closure and GNSS reference points at entrances (Fig. 4a) helped mitigate any unknown survey errors, including magnetic interference. Using a script and a line-by-line review, splay measurements were converted to left, right, up, down distances normal to the direction of survey so that Compass could generate passage volume. We used Adobe Illustrator for cartography and CaveXO for 3D visualizations and produced a video visualization and 3D shapefile archive.

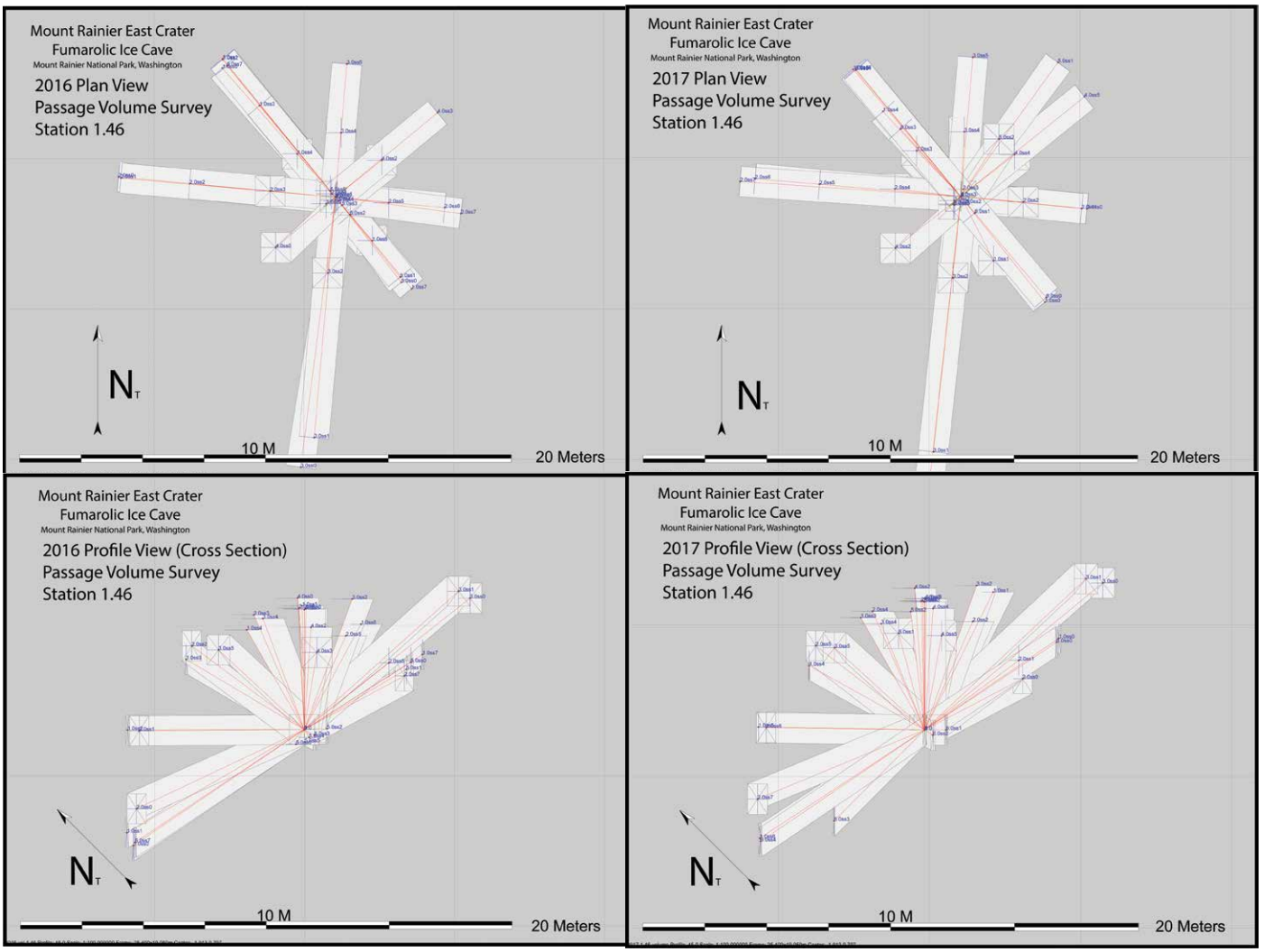

Figure 3. Imagery generated using Compass, representative of survey method used for passage volume surveys in 2016 and 2017 at stations 1.46 and 1.48. The images in plan and profile view, from station 1.46, represent 38 survey shots repeated in 2016 and 2017 with values reported in Table 5.

Surveys are graded UISv2 5-3 BCEF, which allows error ratios of 0.05 m for survey shot length, 1 degree for azimuth and inclinometer measurements, and 2 % overall as per Häuselmann (2012), while GNSS stations are estimated to be accurate within 2−3 m.

Longitudinal comparison was facilitated by a synthesis of reported refereed and historical literature related to the Mount Rainier summit cave system. Literature searches revealed refereed sources and related reports, which were included when observations or data existed regarding the cave system. For historical surveys of the Rainier caves, published planform maps were converted to vector graphics using Adobe Illustrator. Georeferencing and scaling those maps for comparative analysis required aligning crater rim landmarks between those surveys and our own, including the summit (Columbia Crest) and three prominent ridges of the crater rim on the North, West and East side. Stacking the sequential surveys in an overlay made changes easier to qualitatively visualize and communicate. From the overlay comparison, passages were considered potentially consistent if their overlaid positions overlapped, or not consistent if their positions did not. These segments were then isolated in Compass to generate characterization data on each.

Climate and Ablation Monitoring

Methods and equipment used for data collection by Florea et al. (2021) are described therein and supplement original, preliminary data in this manuscript, meant to support a longer-term climate monitoring synthesis. New to this paper are air temperatures measured every 10 minutes at nine locations using Geoprecision M-Log5W-CABLE dataloggers with accuracy: ±0.1 °C at 0 °C (Fig. 4a). Four of the sites were in the circumferential passage: Hobo Point between the passages that lead to the Yeti and Murphy's Law entrances, Main Passage 1 below the Aircrash Entrance, Main Passage 2 be-

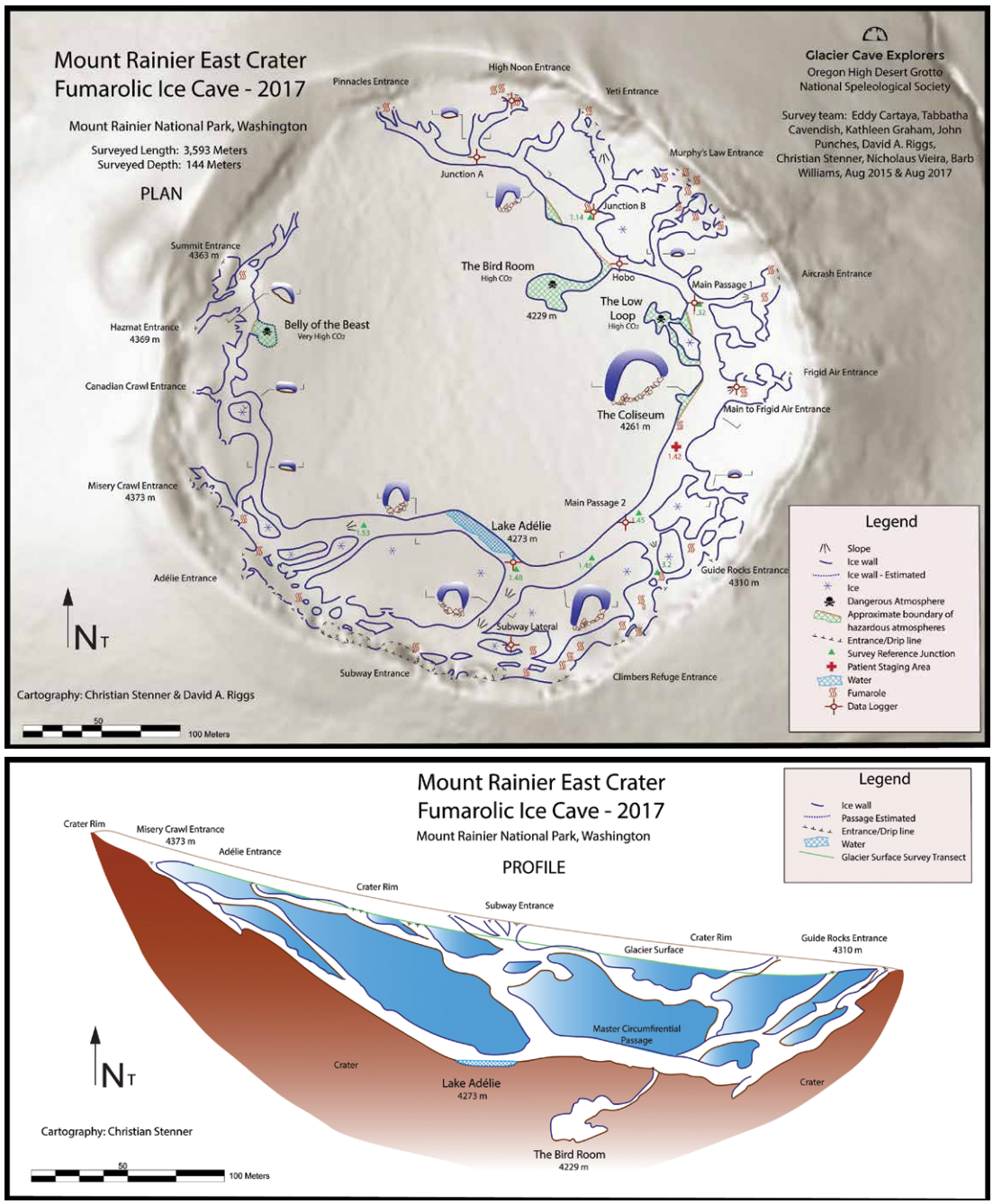

Figure 4. (a) Survey in plan view of the East Crater Cave. Map legend lists key features. Base map is a combination of digital elevation hillshade and satellite imagery (ESRI and Google Earth). Survey indicates locations of data loggers, passage survey reference stations including the locations of passage volume (1.48 and 1.46) and ice ablation studies (1.46). (b) East Crater cave profile looking north, indicating glacier surface transect and key entrances. Foreground passages are shown as viewed looking north. Northernmost entrance passages are omitted for clarity.

low the Guide Rocks Entrance, and near Lake Adélie. Five additional sites were situated near or in the passages leading to entrances: Pinnacles, Yeti, High Noon, Frigid, and Subway. One site recorded data from August 2015 to August 2016 (Subway Entrance,) five from August 2016 to August 2017 (Junction A, Junction B, High Noon, Lake, Frigid Air), and the remaining two from August 2015 to August 2017 (Aircrash, Guide Rocks). Thermographic cameras (VarioCam High Resolution, Jenoptik) recorded ordinal measurements of fumarole locations and cave floor temperatures. In 2015, we imaged the circumferential passage between the Yeti Entrance and Lake Adélie. In 2017, time-series images of a fumarole area near the High Noon Entrance were collected. Three individual fumaroles were instrumented with temperature dataloggers and those data are presented in Florea et al. (2021). Thermographic video is available upon request.

The vertical rate of crater ice ablation was challenging to measure during our expeditions despite various attempts and methods. In our only successful attempt, four plastic markers were installed in the wall of the East Crater Cave at two-meter intervals along with an ice-screw used to aid ice climbing at a maximum height of eight meters (Fig. 4a). All markers and the screw were referenced by survey shots to a nearby fixed station with remeasurement intended to calculate vertical movement and ice residence. All four plastic ablation markers were found on the cave floor the next year; ice squeezing and melt-out caused almost all types of markers to be ejected over time. However, the ice screw was intact in the ice but deformed by pressure against boulders on the cave floor.

RESULTS

Survey Statistics

The 2015−2017 East Crater Cave survey includes 6635 individual survey shots and comprises 3593.3 m of passage that nearly circumnavigates the crater rim and includes 20 separate entrances (Fig. 4a) (Table 2). The highest elevation entrance is at 4373 m and the lowest point is the Bird Room at 4229 m, a vertical range of 144 m (Fig. 4b). Using our ice surface transect, the ice thickness over the circumferential passage floor averaged 47.4 m with a maximum value of 64.6 m (visualized as a thin line across the cave passage in the video of 3D model, Appendix 1). The Bird Room was

Table 2. Survey data from Mount Rainier East and West Crater Cave expeditions, 2015−2017.

Parameter[a]	Units	East Crater	West Crater	Notes[b]
Cave Length	m	3,593.3	307.7	Total length of surveyed segments
Total Surveyed	m	37,303.1	2,487.5	Includes all splay measurements
Cave Depth	m	144.1	33.6	Difference between highest and lowest stations
Cave Volume	m^3	154,018.5	15,477.2	Volume of cave passages based on LRUD data
Average Diameter	m	6.6	7.1	Average passage diameter based on LRUD data
Highest Station	m	4,373.3	4,381.7	···
Lowest Station	m	4,228.5	4,348.1	···

a A 2 % overall error ratio is estimated as per Häuselmann (2012) given the survey methods used.
b Descriptive note regarding the statistical data from Compass derived from Fish (2020).

95 m below the surface transect. Using our single ablation measurement, vertical ice movement was 8.4 m y^{-1} and the residence time was ~7 years for the ice thickness of 57.3 m at the measurement location. Assuming the past estimate of 120 m total ice thickness in the crater (Table 3), and the same rate, the maximum residence time would be ~14 years. The cave includes a circumferential main passage following the strike of the crater with steeply dipping, and perpendicular entrance passages connecting this main passage to the crater rim, visualized in the profile (Fig. 4b), video and data file (Appendix 1).

Table 3. Comparison of Mount Rainier crater caves reported speleometric and morphology data, 1970−2017.

Feature	Cave Dimension per Study Date (m)				Notes
	1970[a]	1973[a, b]	1997[a]	2015−2017[c]	
			East Crater Cave		
East Crater Cave Length	1737	1800	>1500[d]	3593	
East Crater Cave Depth	···	123	···	144	
East Crater number of entrances	~24	~16	12[e]	20	
Main perimeter passage length	915	915	720[e]	999	
Main perimeter passage depth	61	70	···	64.6	
Main passage dimensions	7.6−10.6 × 4.6	15 × 6	15 × -[e]	15 × 6	W × H avg.
Highest point elevation (a.s.l.)	···	4338[e]	···	4373	
Deepest point elevation (a.s.l.)	4228	4215	···	4229	
Deepest point to crater bottom	31.7[e]	~16	···	···	
Deepest point to ice surface	91	~104	···	95	
			East Crater Cave features		
Bird Room dimensions	36.6 × 36.6 × 21.3	54 × 36 × 21	62 × 43 × ···[e]	34 × 30 × 22	L × W × H
Lake Adélie dimensions	···	···	···	50 × 5 × 7	L × W × D
Lake Adélie surface area	···	···	···	~250[f]	
Lake Adélie elevation a.s.l.	···	···	···	4273	

[a] A 2%-5% overall error ratio is estimated as per Häuselmann (2012) given the survey method.
[b] Vertical and horizontal passage position error ratios are ~10 m (Kiver and Steele, 1975).
[c] A 2% overall error ratio is estimated as per Häuselmann (2012) given the survey method.
[d] The 1997 efforts reported a total length of 700 m in the East Crater Cave (Le Guern et al., 2000) whereas Zimbelman (2000) reported more than 1500 m; 700 m is likely a reflection of the length of the main perimeter passage as it is estimated as 720 m long based on the published survey.
[e] Estimated values extrapolated from published survey/data.
[f] Surface area has units of m^2.

In the West Crater Cave, 364 individual survey shots encompass 307.8 m of passage (Table 2). The vertical range spans 33.6 m to the deepest point in the Canary Room. In this paper, we will focus on the East Crater.

Comparative Morphology

The vectorized cave maps from prior expeditions, cartographic plans from our expeditions, and passage volume measurements from 2015−2017 (Table 2) allow comparisons over a 47-year timeframe. As raw survey data were not available from expeditions in the 1970s and 1990s, comparisons were made by extrapolating from statistics and plan-form surveys available in Kiver and Mumma (1971), Kiver and Steele (1975), and Zimbelman et al., (2000) (Fig. 2; Table 3). Profile view surveys and passage cross sections were not published in those studies.

Classification of passage orientations were conducted to aid characterization. Glaciovolcanic passage orientation is constrained by the surface underlying the ice. Where the passage followed sub-horizontal direction, typically towards the center of the crater with downward inclination it was considered dip oriented. Strike-oriented passages were those following the curvilinear contour and not oriented downwards towards the crater center. Limited passage collections were grouped as mixed strike and dip where short sections of maze-like geometries were encountered.

An overlay of all cave surveys (Fig. 5) reveals areas of overlap; the heatmap indicates where passage position remained consistent over 47 years. Areas with three and with four surveys where overlap occurred were color coded and the passages were considered to have positional consistency. As previous surveys included many estimated passages (dashed lines, e.g., Figs. 2b and c) and survey precision could not be resolved they were excluded from these criteria.

To determine characteristics for the observed consistent and inconsistent passages (Fig. 5), the passages were then divided into segments based on their orientation classifications of either dip oriented or oriented along the curvilinear strike. As dip-oriented segments were typically adjoining the master curvilinear passage at their bottom end and crater entrances at the rim at their top end, these provided distinct segments that could be isolated to derive further speleometric data in Compass and align with temperature and fumarole survey data (Table 4).

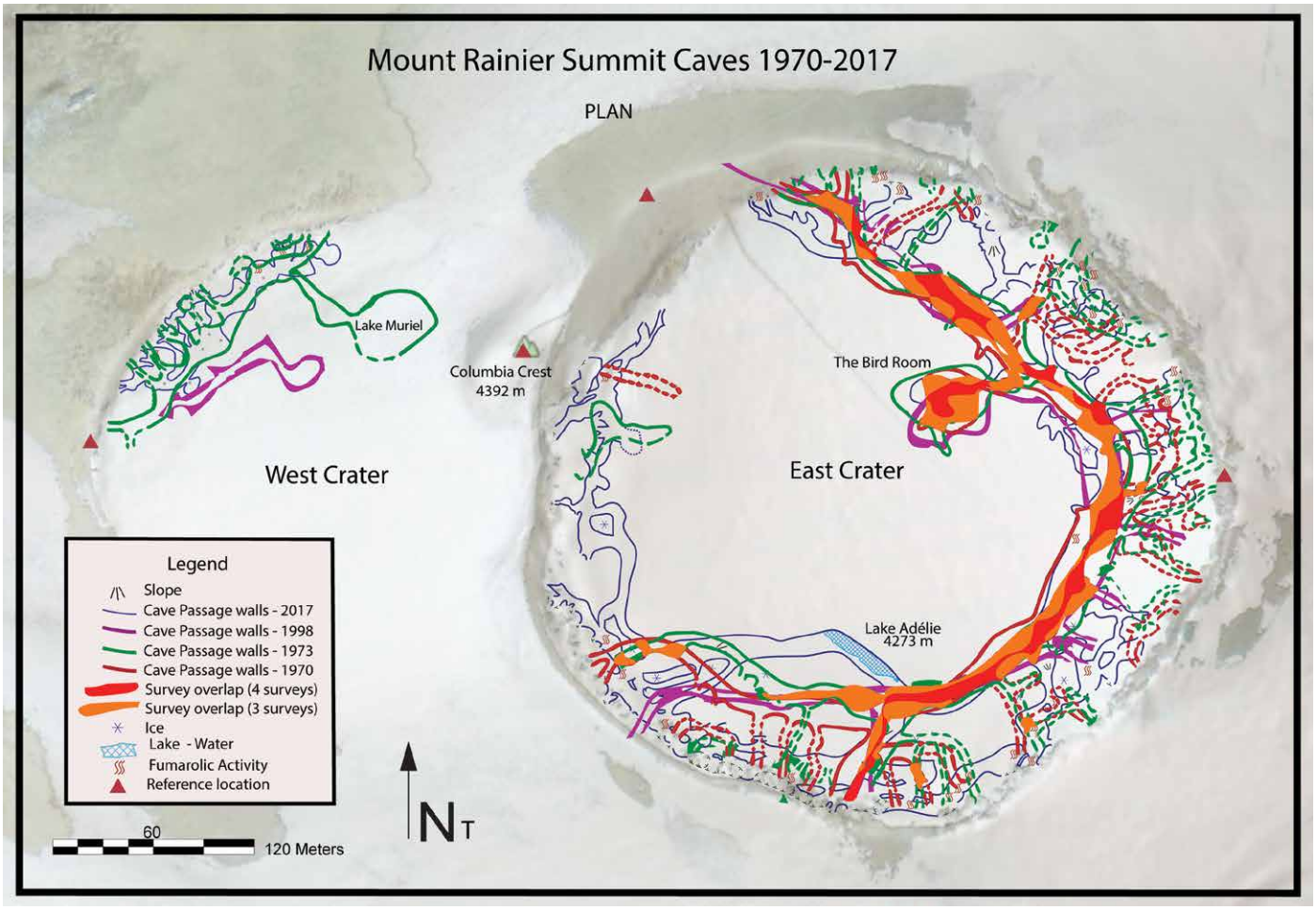

Figure 5. Overlay of corrected and georegistered passage wall planform surveys from 1970−2017. Red-orange heatmap indicates areas where passage overlap occurred between three or four surveys. Four reference locations shown were used to align surveys. Base map is from satellite imagery (Google Earth).

Table 4. Mount Rainier East Crater Cave segments and air temperature data.

Passage Name	Orientation Classification	Planform Consistency	Average Inclination (m)	Average Diameter (m)	Temperature			
					Min (°C)	Max (°C)	Mean (°C)	Variance[a] (C°)
Low Loop	Dip	Unresolved	19.8	2.1	···	···	···	···
Small lead Aircrash South	Dip	Unresolved	31.2	3.0	···	···	···	···
Coliseum to Guide Rocks	Dip	Unresolved	25.3	3.9	···	···	···	···
Small lead Aircrash North	Dip	Unresolved	30.0	3.5	···	···	···	···
Branch South of High Noon	Dip	Unresolved	21.0	1.9	···	···	···	···
Aircrash entrance connection	Dip	Unresolved	30.4	3.0	···	···	···	···
Yeti East (Junction B)	Dip	Unresolved	19.1	3.7	−14.7	9.6	2.8	13.7
High Noon entrance (2017)	Dip	Unresolved	21.2	3.9	−9.6	9.4	2.1	5.6
Yeti lower connection	Dip	Unresolved	30.2	4.8	···	···	···	···
Adélie small tributary	Dip	Unresolved	30.7	0.7	···	···	···	···
Lake Adélie entrance down	Dip	Unresolved	35.5	5.7	···	···	···	···
Subway Entrance down	Dip	Consistent 3−4 surveys	30.3	7.1	···	···	···	···
Bird Room and connection	Dip	Consistent 3−4 surveys	26.5	7.4	···	···	···	···
Adélie to subway upper maze	Mixed	Unresolved	21.0	3.6	···	···	···	···
West Extension	Mixed	Unresolved	19.4	2.3	···	···	···	···
Pinnacles entrance (Junction A)	Mixed	Unresolved	30.1	3.7	−12.4	6.8	1.4	8.2
Columbia Crest area	Mixed	Unresolved	18.7	4.2	···	···	···	···
Climbers Refuge maze	Mixed	Unresolved	25.8	6.0	···	···	···	···
Main borehole to Frigid ent. (2017)	Mixed	Unresolved	28.7	4.9	−9.5	10	0.8	7.8
Yeti upper lateral section	Strike	Unresolved	25.8	3.4	···	···	···	···
Belly of Beast near summit	Strike	Unresolved	24.5	2.3	···	···	···	···
Climbers refuge area	Strike	Unresolved	20.2	6.4	···	···	···	···
Subway lateral area (2016)	Strike	Unresolved	15.4	3.9	−15.5	3.3	0.1	4.6
Aircrash entrance lateral	Strike	Unresolved	25.8	6.0	···	···	···	···
Yeti to Murphy's law entrance	Strike	Unresolved	24.9	3.6	···	···	···	···
Master curvilinear passage	Strike	Consistent 3−4 surveys	14.7	7.8				
Hobo point (2017)	···	···	···	···	−9.5	6.4	1.7	3.8
Main passage 1 (2016)	···	···	···	···	−8.9	8.1	2.1	4.8
Main passage 1 (2017)	···	···	···	···	−8.9	7.7	2.3	4.7
Main passage 2 (2016)	···	···	···	···	−5.7	5.3	1.8	2.5
Main passage 2 (2017)	···	···	···	···	−4.5	5.6	1.9	1.8
Lake Adélie East	···	···	···	···	−6.9	5.4	1.2	1.4

[a] Average of the squared differences from the mean.

From these criteria, most of the master curvilinear passage showed consistency across multiple surveys, from the East side of Lake Adélie (Fig. 6a) until just before the 2017 Pinnacles entrance. The Bird Room (Fig. 6b), along with the passage connecting the East side of Lake Adélie to the Subway entrance also showed consistency across multiple surveys.

The remaining segments changed considerably from earlier planform surveys or could not be resolved to have positional consistency due to expected survey errors or in that previous surveys of those passages were estimates of position and geometry. Our comparison reveals three main areas of change in East Crater Cave. First, a shift in the circumferential passage at the southwest end of East Crater Cave where all historical surveys demonstrate the passage as higher up the crater rim; Lake Adélie is only represented on the most recent survey. Second, 598 m of additional passages were surveyed in 2015−2017 on the west side of East Crater starting from the westernmost limits of all previous

Figure 6. (a) East side of Lake Adélie, East Crater Cave. (b) The Bird Room, East Crater Cave, showing inclination of the floor surface and ablation scalloping difference on cave walls compared to master circumferential passages.

maps and nearly completing the crater circumnavigation, lacking 82 m of intervening distance (Figs. 4a and 5). At least three fumaroles were located in this extension, which had an average passage diameter of 4.7 m. The resulting passage extension wraps around the west side of the East Crater. Third, none of the dendritic passages radiating outward from the master curvilinear passage and entrances along the crater rim remained consistent across the surveys excepting the passage connecting Lake Adélie to the surface (Fig. 5).

Comparative cross section and planform measurements from two survey stations (Figs. 3 and 4a) across 2016−2017 are reported in Appendix 2 and summarized in Table 5. The mean increase in distance from station to the walls was 0.13 m across both locations.

Thermographic Survey

Thermal camera recordings clearly identified individual fumarole vents emitting vapor or gas in fumarole fields on the crater floor (Fig. 7a). Additionally, areas of heated sediment or rock were present. In the circumferential passage between the Yeti Entrance and Lake Adélie, we identified 9 areas of high heat flux each with more than 10 spots above 30 °C and up to 51 °C, and an additional 11 areas with 1−9 spots above 30 °C. These areas of heat flux alternate with zones with no or little fumarole activity to form a ring coincident with the circumferential passage (Fig. 7b). We documented another discontinuous ring of fumaroles above 30 °C near the crater rim (Fig. 4a) that, unlike the lower circumferential passage, no continuous passage connects those fumaroles but they are coincident with many entrances. Thermographic recordings in 2017 near the High Noon Entrance showed temperature variations of up to 15 °C on the crater floor over time spans of a few hours.

Air Temperature

Time-series graphs of the measured air temperature compiled from dataloggers are presented in Figure 8, with summary statistics in Table 4. Further descriptive information on the datalogger locations and influences are offered below.

Main Passage 2, offset from the passage that leads to the Guide Rocks Entrance, was not directly affected by fumaroles and remained mostly free of fog. At Main Passage 1, offset from the passage that leads to the Aircrash Entrance,

Table 5. Mount Rainier East Crater Cave main passage volume measurements, 2016−2017.

Azimuth measured (deg / deg)	Change (m)[a]
Lake East (station 1.48)	
65 / 245	0.28
155 / 335	0.58
290 / 110	−0.61
20 / 200	−0.40
200 / 20	0.13
Mean	−0.01
Change[a]	0.13
Coliseum (station 1.46)	
140 / 320	−0.00
320 / 140	0.21
95 / 275	0.09
5 / 185	0.40
50 / 230	0.72
Mean	0.24
Change[a]	0.13

[a] Mean difference in meters between comparative measurements made in 2016 and repeated in 2017.

numerous fumaroles were observed during fieldwork to cause a prevailing dense fog and airflow was toward the entrance. The Subway Entrance site is approximately five meters below the Subway Entrance in a larger space at the top of the vertical shaft extending to the main passage.

In 2016−2017 additional measurement sites were added (Table 4). Junction A is below the High Noon entrance, as well as the Pinnacles entrance, and is defined by two entrances to the outside as well as the connection to the main curvilinear passage. No fumaroles exist in the vicinity of the datalogger. Junction B is located in a large dome-like hall on a slope directly below the passage to the Yeti and the Murphy's Law entrances, and is thus influenced by two connections to the main passage and one entrance to the outside. In addition, several active fumaroles or fumarole fields exist in this hall, which explains the large size of the room. Here both the highest maximum and nearly the lowest minimum of all measurement locations were recorded. One of the strongest fumaroles found is located a few meters below the temperature sensor.

The Lakes site is immediately adjacent to Adélie Lake (Fig. 6a), approximately one meter above the water level; this area is also unaffected by fumaroles. Results here correspond predominantly with the neighboring Main Passage 2 site, but exhibit stronger overall cold air intrusions from the Subway Entrance, which is also underscored by the low annual mean temperature of 1.2 °C.

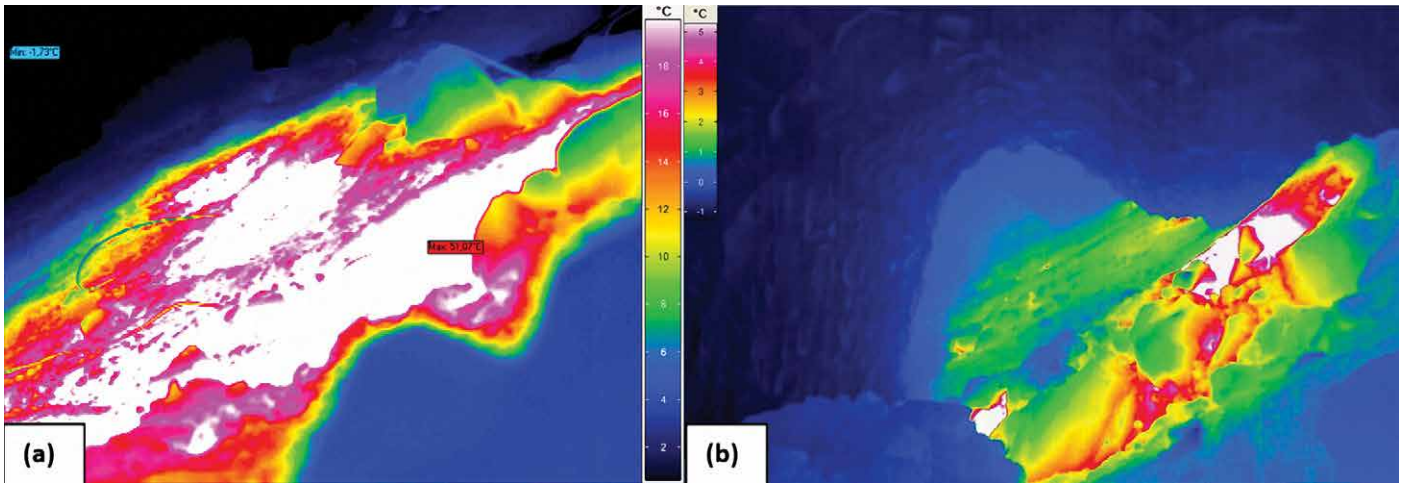

Figure 7. East Crater Cave thermographic investigations, observations, and fumarole information. (a) Representative thermographic image from video recording showing a 51 °C hot spot (labelled within image) on the crater floor inside East Crater Cave, located near the High Noon entrance. Temperature minima in the image is 1.7 °C. (b) Representative thermographic image from video recording of the laterally oriented main passage in East Crater Cave. Fumarolic heat and hot spots can be observed on the crater floor from 1 °C to 5 °C. The image shows two areas of heated ground separated by a colder area. The areas of heated ground correspond to wider dome shaped rooms that are interconnected by slightly narrower passages.

DISCUSSION

When glacial ice superimposes an active volcanic edifice, localized heat transfer causes ice melt. The result is glaciovolcanic caves (Sobolewski, et al., 2022a). *A priori*, the scope, scale, and shape of these glaciovolcanic caves very much depends upon the mode and magnitude of heat transfer, and the rate of accumulation and movement of the glacial ice. The persistence of a glaciovolcanic cave is therefore dependent upon continued volcanic heat flux and a favorable climate for glacial ice accumulation. When heat flux ends and fumaroles cease, plastic deformation of glacial

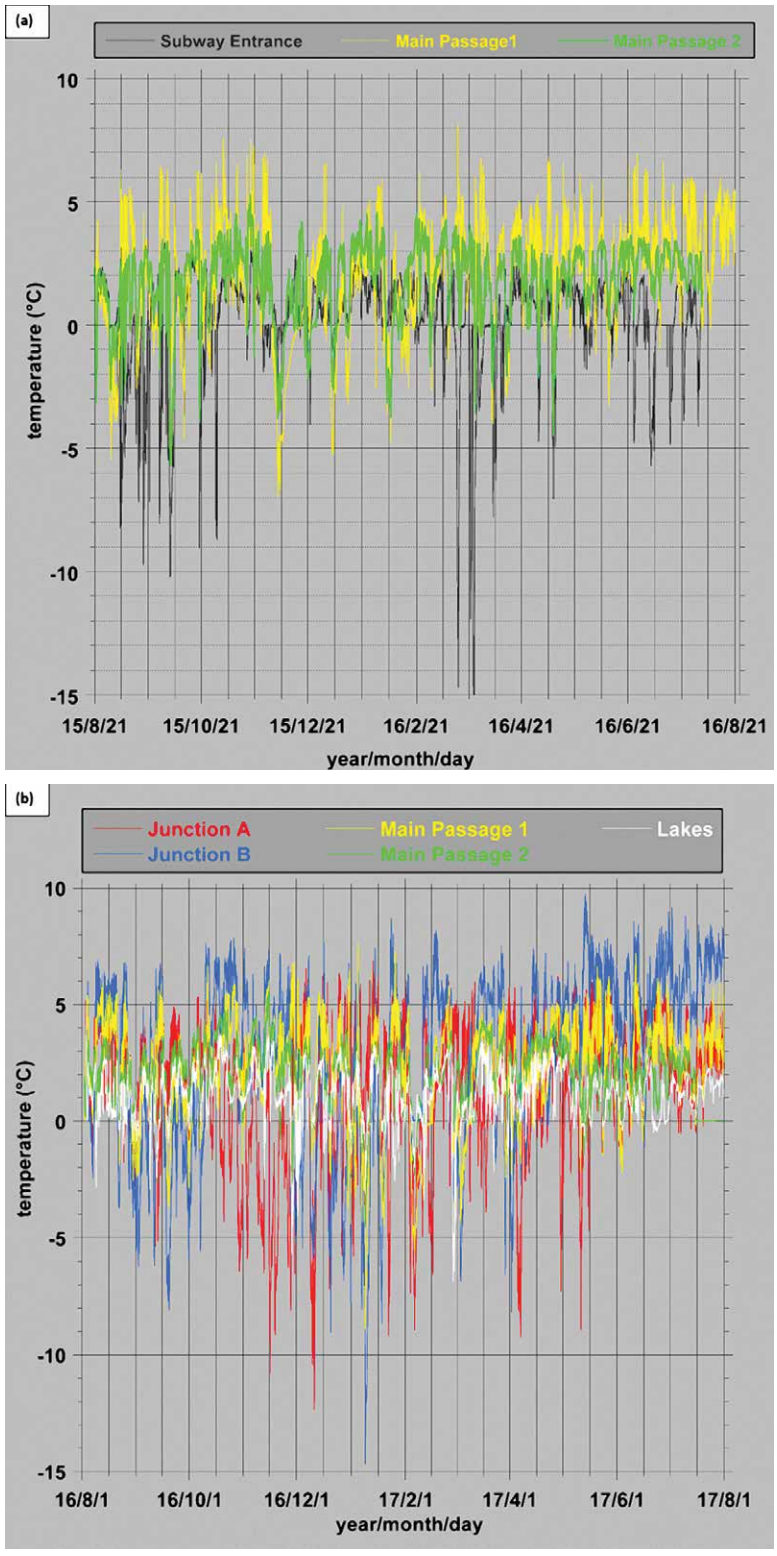

Figure 8. (a) Air temperature (°C) from the three cave passages measured from August 2015 to August 2016. (b) Air temperature (°C) from the five cave passages measured from August 2016 to August 2017.

ice will squeeze these caves closed. In contrast, when climate warms and snowfall ceases, melt will daylight and eventually eliminate these caves, such as those on the Paradise Ice Field of Mount Rainer (Anderson et al., 1994). In short, glaciovolcanic caves are ephemeral phenomena.

The Cascade Volcanic Arc in the Pacific Northwest of the United States is a valuable laboratory for investigations of glaciovolcanic caves. At Mount Hood, the caves in the Sandy Glacier are shrinking as the glacier retreats (Pflitsch et al., 2017). At Mount Saint Helens, the caves are expanding as Crater Glacier grows (Sobolewski et al., 2022b). In contrast, exploration at the summit of Mount Rainier reveals a system of glaciovolcanic caves that persist for at least a half-century. We suspect that the high elevation, bowl-like summit craters and persistent fumaroles have culminated in a stable setting for these glaciovolcanic caves. It is not evident that these caves at the summit of Mount Rainier are in equilibrium, however.

Glaciovolcanic Caves at the Mount Rainier Summit are in Dynamic Equilibrium

Direct measurements of passage cross section in the two measured areas of the circumferential passage, East of Lake Adélie and at the Coliseum, show no detectable change in passage dimensions from 2016 to 2017 (Table 5) given the expected survey error. Furthermore, the debris ridges along the bottom of the circumferential passage reported in Kiver and Steele, (1975) were present in 2015, 2016, and 2017 and of similar distance to the cave walls, conveying consistency in main passage size and position. (Fig. 9a). More generally, the scale and position of the circumferential passage shows consistency across all included maps. The one exception are the sections west of Lake Adélie where the circumferential passage alternates from shallower to deeper parts of the crater over the past half century in an area devoid of fumaroles during the 2015−2017 survey (Fig. 5).

Ice movement in the crater has not been accurately measured. Tephra layers and strain indicators in the East Crater Cave suggest a west to east horizontal direction of movement from Columbia Crest. Vertical rates of ice motion were estimated by Kiver and Steele (1975) to be 1.66 m y^{-1} to 2.65 m y^{-1} and 2.05 m y^{-1} to 3.48 m y^{-1} in the East Crater and West Crater Caves, respectively, using similar methodology but over a maximum 11 days' timeframe. Our single estimate of 8.4 m y^{-1}, while noteworthy, is not conclusive of an increase in ice motion since the 1970s despite higher rates of glacial retreat on the edifice flanks (Anderson and Shean, 2022).

Despite this ice motion, most of the circumferential passage has remained much the same over 47 years (Fig. 5); fumaroles and heated rock persisted at the same locations for decades and air flow maintains the connections between

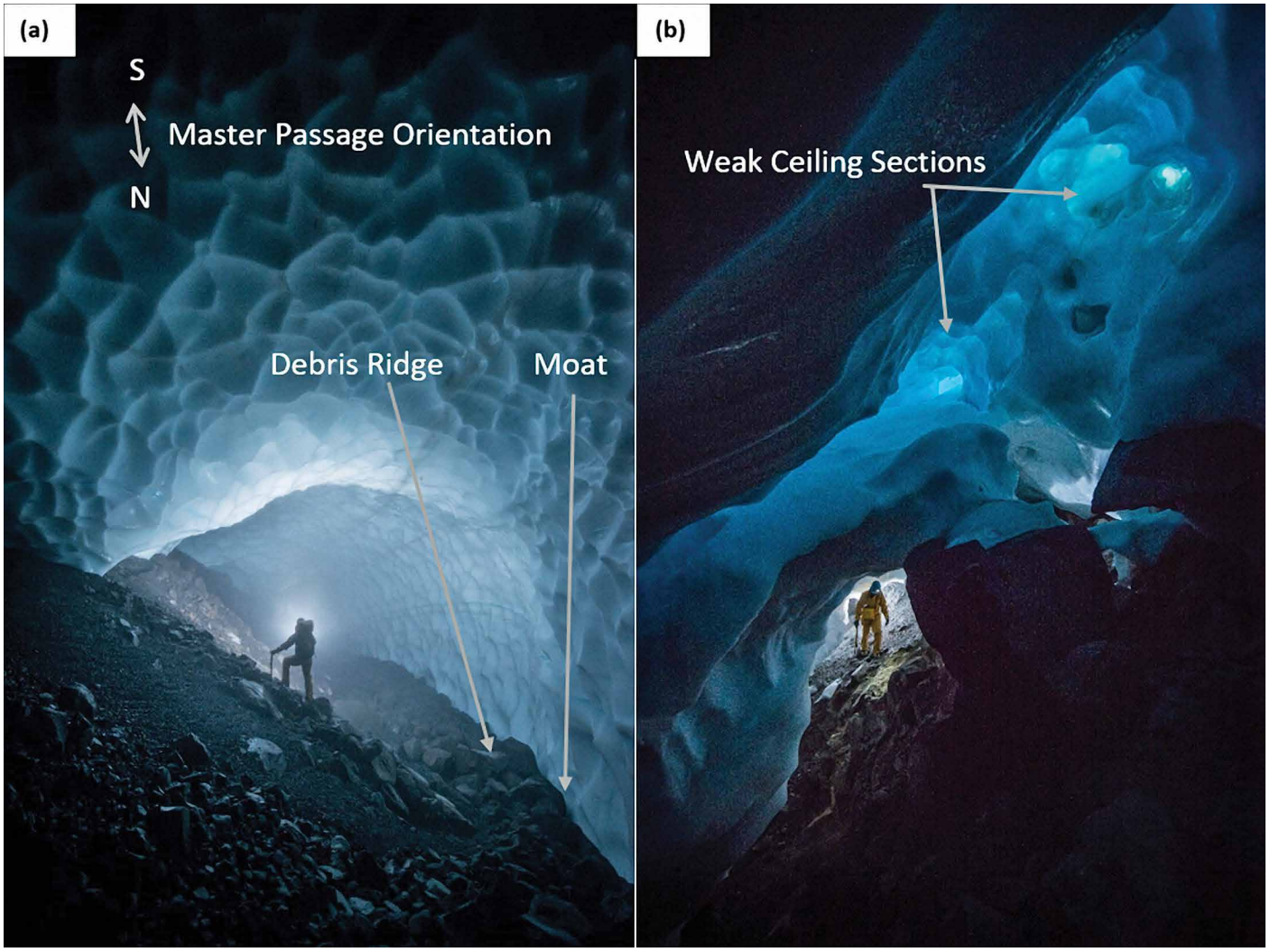

Figure 9. (a) Typical passage in the East Crater cave master circumferential passage. Debris build up against the inner side of the ring (right side) passage buttresses a small moat, as observed in 1973 (Kiver and Steele, 1975). (b) Upper-level cave passages display numerous skylights, weak spots in ceilings, and occasional debris collapse.

these areas of heat flux. As the glacial ice moves, it deforms around the open void and squeezes shut downslope of the zone of heat flux. Thus, most of the circumferential passage has achieved a dynamic equilibrium where the exact position and shape may vary from year to year below a threshold value as governed by sensitivities to external and internal forcing (Florea et al., 2021). These sections of cave contour the curvilinear strike of the crater (Appendix 1), are sub-horizontal (Table 4), and are more or less conserved in the decadal timespan of this synthesis (Fig. 5; Table 3).

Of interest is the absence of cave passage on the west side of East Crater prior to the 2015−2017 expeditions that added 598 m of mapped passage in that area (Fig. 4a). Also curious is the position of the circumferential passage connecting this western extension to Lake Adélie and points east (Figs. 4a and 5). In the case of the former, the increase may potentially source to previous inaccessibility of these passages or to increased fumarole activity near Columbia Crest. Smaller average passage diameters (4.8 m) than elsewhere in East Crater Cave (6.6 m) may suggest a younger state of development for the extension (Fig. 10a). In the case of the later, this connecting passage is dramatically different in all four surveys (Fig. 5), perhaps increased ice movement in this section sweeps passages at the crater rim away from their originating fumaroles where they are maintained only by significant advection until they squeeze shut and the process is repeated. These sections of cave, as well as most other passages steeply rising to or following the crater rim (Fig. 4; Appendix 1) are dendritic feeders or distributaries of fumarole advection and dynamically change throughout the timeline of this synthesis (Table 4).

Microclimates Influence Passage Equilibrium

The synthesis of a year-long dataset of cave and fumarole temperature, air pressure, and water level in Lake Adélie conducted by Florea et al. (2021) was a detailed look into high-frequency (15-minute) changes in the microclimate en-

Figure 10. (a) Typical passage in the East Crater cave, NW extension, passages trending upwards towards the crater rim display low, wide forms. (b) Hazmat Entrance, East Crater Cave, showing a passage collapse.

vironment of a small portion of the Mount Rainier glaciovolcanic caves. That study investigated the seasonality of these caves; as the winter snowfall season seals entrances, advection diminishes, and convection dominates until melt-out reopens the entrances and resets the system. That study, without direct evidence, inferred short term changes in the size of the circumferential passage linked to melt rate. It also noted the changing size and position of entrances through time. Maps and data from this study document those changes over a punctuated decadal timespan. Inter-annual temperature monitoring presented herein span the cave floorplan, and thus are more representative of system-wide variation through time.

At first glance (Table 4), the summary statistics reveal that conserved sections of cave that are in dynamic equilibrium (three dataloggers) have warmer average temperatures with smaller variation about the mean (T_{ave} = 1.8 °C, σ = 3.2 C°; T_{min} = −7.4 °C, and T_{max} = 6.4 °C). These passage segments are larger (D_{ave} = 7.4 m) and concentrate in the circumferential passage and the bigger persistent Subway entrance and Bird Room. In contrast, sections of cave that are transient (five dataloggers) have cooler average temperatures with greater variation about the mean (T_{ave} = 1.4 °C, σ = 8.0 C°; T_{min} = −12.3 °C, and T_{max} = 7.8 °C). These passage segments are smaller (D_{ave} = 3.8 m) and concentrate along the crater rim, including most entrances and the passages that connect to the deeper cave, including the circumferential passage west of Lake Adélie. In these sections of cave where solar insolation can be strong, oscillating ventilation of fumarole steam and incursions of cold air are interrupted by winter snowfall occlusion.

A deeper dive at a few datalogger sites provides additional context. The Subway Entrance (persistent across the suite of survey maps) experiences regular intrusions of cold outside air in the spring and autumn months and records the lowest minimum, maximum, and average temperatures among the sites (T_{ave} = 0.12 °C, σ = 4.6 C°; T_{min} = −15.5 °C, and T_{max} = 3.3 °C). These same intrusions are missing in the winter when they would be most expected. Instead, the winter data are relatively stable near 0 °C and support an entrance closure by snowpack described in Florea et al. (2021) using dataloggers at Lake Adélie.

In the circumferential passage, and below the Subway Entrance, air temperature data greatly stabilizes near Lake Adélie (T_{ave} = 1.2 °C, σ = 1.4 C°; T_{min} = −6.9 °C, and T_{max} = 5.4 °C). The cool but predominantly balanced temperature conditions are underlined by the low variance of 1.4 °C. Air warms counterclockwise along an eastward path of advection toward the Coliseum, fumarole areas, and the Main Passage 2 area below the Guide Rocks Entrance (T_{ave} = 2.3 °C, σ = 4.7 C°; T_{min} = −8.9 °C, and T_{max} = 7.7 °C) where pulses of cold air occasionally descend. Main Passage 2 showed the highest temperature peaks of the conserved passages. There, influence by air heated by fumarole outgassing from the neighboring hall is convectively led into the upper areas of the space and exhausted via the elevated connecting passage. The comparatively high variance of 4.8 C° within this hall is likely due to cold air infiltration from the Guide Rocks entrance.

Results rarely showed lower temperature minima than Main Passage 1, falling well below 5 °C only once. The maxima are lower than at Main Passage 1 almost year round but still often significantly higher than the values of the Subway Entrance.

Similarly, temperatures near the Pinnacles Entrance (T_{ave} = 1.4 °C, σ = 8.2 C°; T_{min} = −12.4 °C, and T_{max} = 6.8 °C) warm and stabilize along a clockwise path of advection past the fumarole field below the Yeti Entrance (T_{av} = 2.8 °C, σ = 13.7 C°; T_{min} = −14.7 °C, and T_{max} = 9.6 °C) toward Hobo Point (T_{ave} = 1.7 °C, σ = 3.8 C°; T_{min} = −9.5 °C, and T_{max} = 6.4 °C) and the area below the Aircrash Entrance (T_{ave} = 1.9 °C, σ = 1.8 C°; T_{min} = −4.5 °C, and T_{max} = 5.6 °C). The section of circumferential passage centered on the Coliseum, where advection paths converge and heated areas concentrate (Fig. 5), has remained exceptionally consistent for a half century.

Morphodynamic Model for Glaciovolcanic Caves

Glaciovolcanic cave morphology is minimally classified compared to the detail applied to caves formed in soluble rocks (e.g., Ford and Williams, 2007). We used this and similar studies at Mount Saint Helens (Sobolewski et al., 2022b) and Mount Hood (Pflitsch et al. 2017) to arrive at similar detailed characterizations. A key difference is the rate of change in these settings, which matches the pace of change in some coastal environments where the morphology is highly dynamic across decadal and shorter timescales. We borrow and apply the term morphodynamic from that literature to highlight the connection between the pace of change and the resultant morphology (Wright and Thom, 1977). This study is one window into that connection.

The balance between heat flux and climate guides the pace of development and the longevity of glaciovolcanic caves. When those two factors are balanced, passages that originate around and connect fumarole areas will persist, and the pace of ice ablation by melt matches the rate of ice replacement by glacial movement. In contrast, when those two factors are not balanced, melt will daylight the caves or ice movement will squeeze the passages closed. In reality, both processes occur in all glaciovolcanic settings; nowhere do these factors balance at the timescale of glaciovolcanic cave evolution, even on Mount Rainier where the summit caves have persisted for at least a half century.

In this study, and comparing our data to prior expeditions, we are able to divide the East Crater Cave on Mount Rainier into two primary categories, passages that are transient and those that are conserved in a dynamic equilibrium. Most of the circumferential passage has remained remarkably consistent, maintaining a similar position, scale, and morphology over a 47-year timespan. Consistency in reported main passage length, depth, and

Figure 11. Entrance zones of cave passages in East Crater Cave without direct fumarolic influence. (a) Snow and debris on floor extends into the cave. (b) Walking and crawling passages are shown while ice walls typically connect directly to the floor at the rock-ice margin with no airspace.

dimensions (Table 3), along with visual observation of debris ridges (Kiver and Steele, 1975) demonstrate the similarity. Our detailed cross-section measurements from one year to the next could not resolve any change in size and point to consistent passage scale. As west-to-east advection in this passage connects dome shaped rooms above heated rock and active fumaroles, temperatures warm (T_{ave} = 1.2–1.4 °C); and stabilize (σ = 1.4–4.7 C°) and passage equilibrium increases.

Passages that are transient tend to be smaller in diameter (3.8 m compared to 7.4 m) and are subject to higher temperature fluctuation (σ = 8.0 C° compared to 3.2 C°), and concentrate along the crater rim, but include some passages that connect the rim by advection to the deeper circumferential passage (Fig. 11a and b). Fumaroles maintain passage development here too (Fig. 12). Seasonal weather extremes, however, are not buffered by the heat capacity of the ice. In the summer, meltout can, and does, occur from fumarole heat and solar insolation (Fig. 9b), while mechanical collapse can occur as well, restricting airflow and potentially blocking entrances (Fig. 10b). In the winter, some entrances are sealed shut by accumulated snowfall and bitter cold. Disparate numbers of surveyed entrances across the study timeframe confirm the transience (Table 3). The compaction of firn to ice as snowfall maintains the glacial plug means that some passages are swept away from their heat source. The results point towards a situation where the deeper circumferential passages within the Mount Rainier system are not as influenced by seasonal weather and maintain a dynamic equilibrium (Florea et al., 2021). The upper ring of fumaroles, while they may maintain open passages, are too influenced by external factors to remain conserved over time. Fig. 13 visualizes these two primary categories and their existence within the dynamic equilibrium.

Broader Implications

The potential for Cascade volcanoes, such as Mount Rainier, to impact large population centers drives the need for longitudinal studies. Changes within a volcanic system causing alteration of glaciovolcanic void morphology can make them a volcano monitoring and hazard indicator (Curtis and Kyle, 2017). Longitudinal-morphology studies may identify conserved and transient glaciovolcanic cave passages as normal conditions on an edifice. Unlike nearby glaciovolcanic caves on Mount Saint Helens that are expanding (Sobolewski et al., 2022b) and Mount Hood that are retreating (Pflitsch et al., 2017) and not in dynamic equilibrium, any sudden and dramatic changes in glaciovolcanic cave morphology on

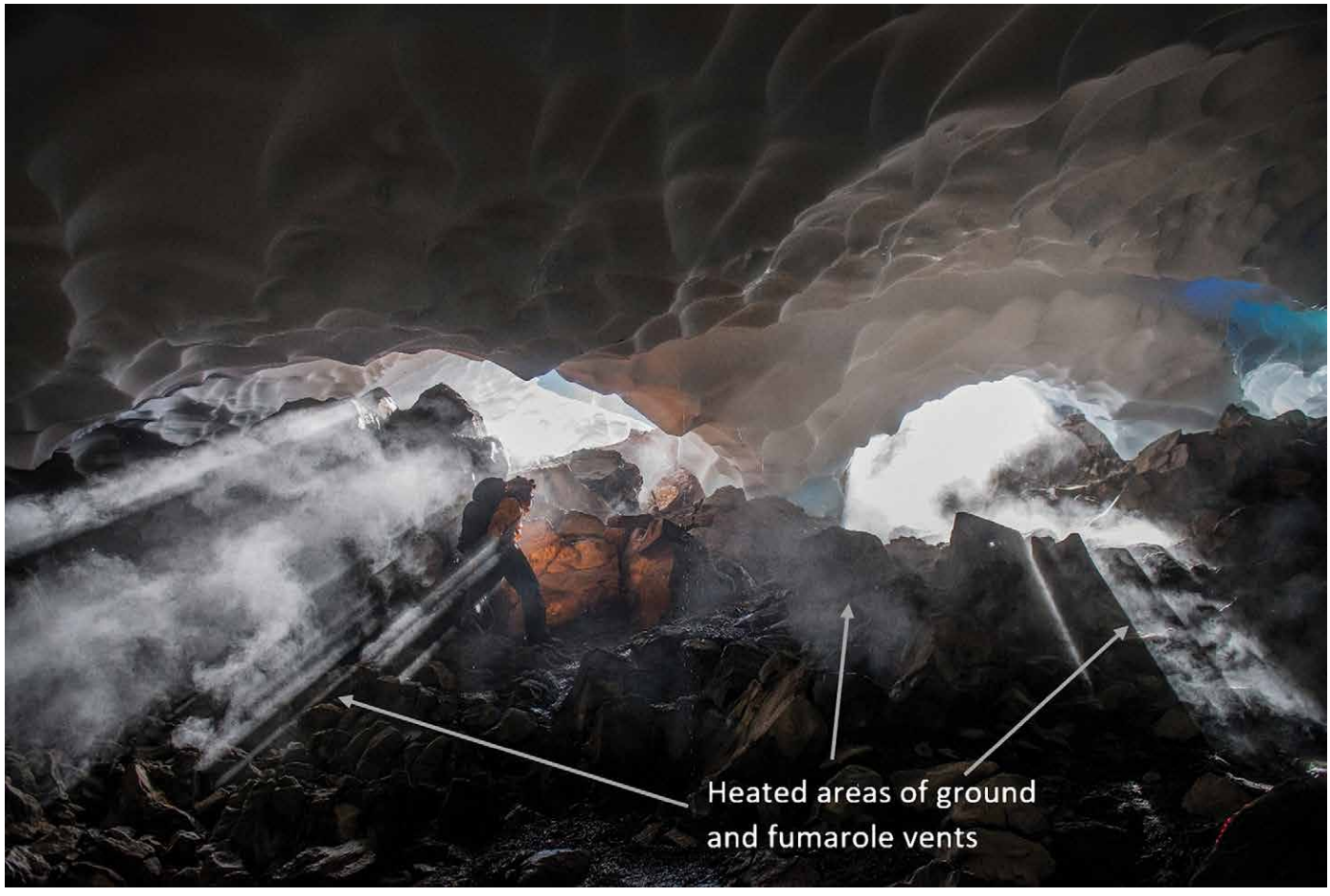

Figure 12. Entrance zones of cave passages in East Crater Cave with direct fumarolic influence (Murphy's Law entrances).

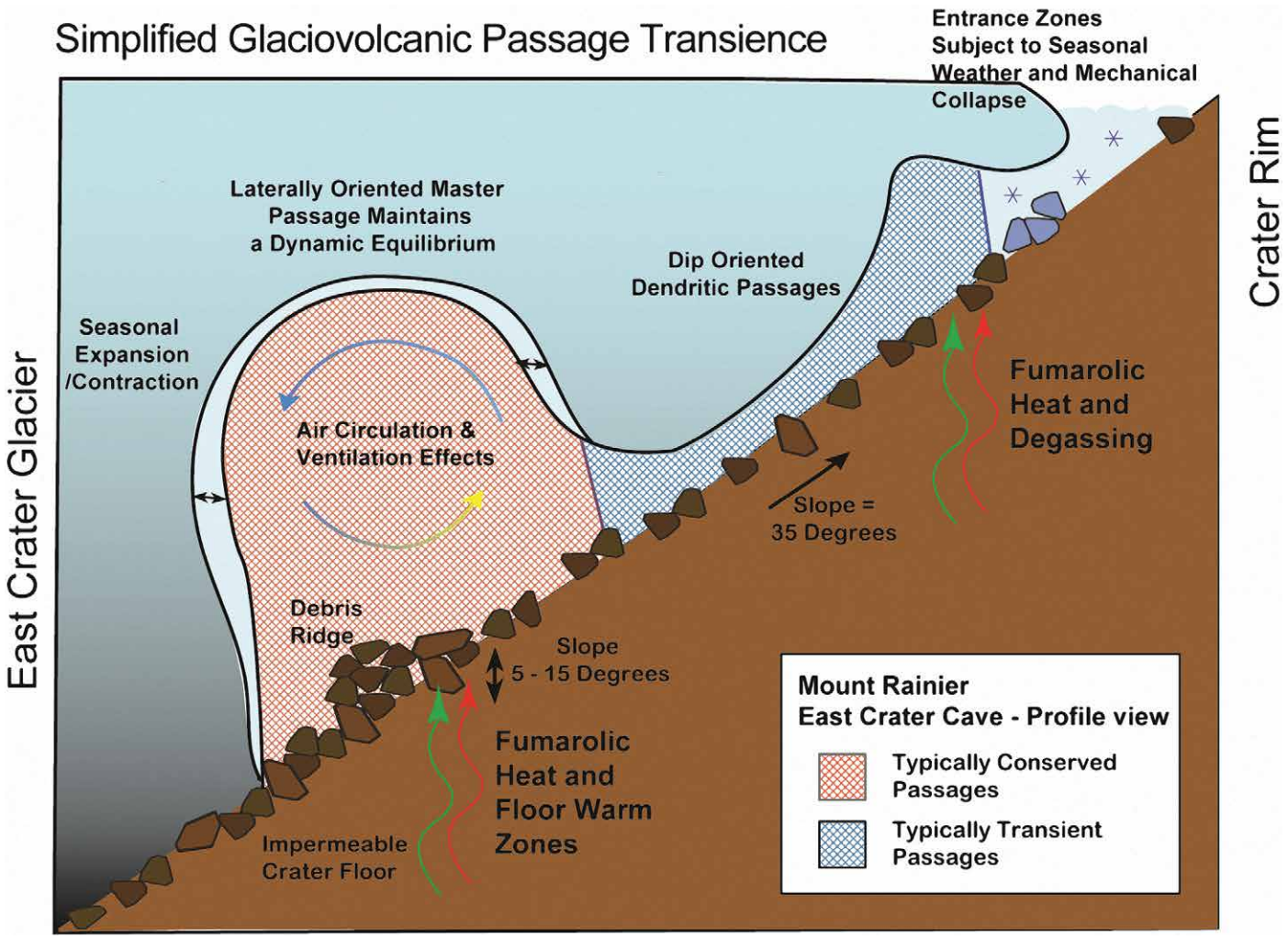

Figure 13. Cross-section diagram of the passages within the Mount Rainier system showing typical lateral and dip-oriented passages. Master circumferential passage with dynamic equilibrium is conserved while transient passages radiate from the master passage towards ephemeral entrances and entrance zones.

the Mount Rainier summit or similar edifices are a heightened cause for concern and worthy of further investigations. Accurate detection of changes to volcanic activity by other methods (e.g., aerial and satellite remote sensing, deformation monitoring, or increased seismicity) may not always capture early changes to heat flux on a glaciated edifice where the ice may absorb considerable heat output; the direct sublimation 1 g of ice at 0 °C to water vapor or the phase change of that ice to fumarole steam at 100 °C requires heat inputs of 2838 J or 6750 J, respectively. Put another way, existing conserved glaciovolcanic cave passages and other subglacial voids may enlarge substantially, and/or transient passages may multiply. These potential observations can be made before other changes on the edifice are measurable or before externally visible changes occur due to increased heat input.

Limitations of this study include the reliance on historical data with disparate collection and survey methodologies. To accurately demonstrate the changes observed in passages with rapidly evolving position and morphology, and to compute ablation rates in relatively stable passages (Florea et al., 2021) will take sequential mapping over several years, using techniques such as LiDAR or Simultaneous localization and mapping (SLAM), to produce timelapse 3D maps. Collecting a full inventory of temperature, relative humidity, and airflow data along with ice ablation and calculated heat flux will assist to explain formation mechanisms and verify new analytical and numerical models (e.g., Unnsteinsson, 2022) Such evolution in mapping and understanding glaciovolcanic environments has further implications as we look beyond terrestrial examples to thermal influences on ice-covered ocean worlds. The microclimates and morphologies of glaciovolcanic caves can leverage hypotheses of similar environments elsewhere in the solar system and provide insight into perennially cold, dark, oligotrophic ecosystems like frozen Martian cave systems hypothesized to be the most accessible location of current life or intact biomarkers. (Sobolewski, et al., 2022a; Curtis, 2020; Davis et al., 2020; Tebo et al, 2015). Understanding the factors influencing long term longevity of void spaces in ice can play a role in these investigations.

CONCLUSIONS

The East Crater Cave at Mount Rainier, at 3593 m in length and 144 m in depth is a significant example of a glaciovolcanic cave that provides insight into the dynamics of this subset of speleology. Comparative measurements of statistical information and historical surveys of the Mount Rainier glaciovolcanic caves over decadal timescales, from 1970−2017, provided insight into glaciovolcanic cave passage morphodynamics. The caves exhibit distinct morphology patterns and have expanded in the 47 years since the first reported survey results.

Comparisons revealed persistent circumferential master passages with characteristically similar low gradient sub-horizontal lateral orientations following the curvilinear crater contour. Two persistent entrances and the cave low point were also characterized. These passages are considered conserved given positional and geometric similarity over time but with vertical ice advection around a consistent passage form. Persistent passages displayed stable temperatures, or where temperatures varied, were influenced by adjacent fumarole activity. Persistent fumaroles and heated floors assist in maintaining the master passage in position and form.

Transient passages were revealed with smaller average diameters and larger temperature variances. A previously undocumented extension of 598 m on the west side of the East Crater had smaller diameter passages. Transient passages were the most thermally unstable and were potentially influenced by snowpack accumulation and entrance collapses. Entrance zones exhibit seasonal and long-term transient morphology, whereby snowpack and collapse combined with persistent fumarolic output and pressure drive competitive development of new outlet passages originating radially from the conserved source passages. Morphodynamic factors influencing these glaciovolcanic cave passage types include non-linear ice dynamics and point source and area heat fluxes and require additional research to understand.

ACKNOWLEDGEMENTS

Financial and equipment support from National Geographic Expeditions Council, the Mazamas Research Grant, the Mountain Rescue Association, Petzl, REI, Alberta Speleological Society and National Speleological Society. Aaron Messinger and Special Projects Operations, supplier of SCBA equipment. Eugene Kiver, Bill Lokey, and Aaron Curtis for helpful advice and support. Additional cave surveyors 2015−2017, Tabbatha Cavendish, Kathleen Graham, John Punches, Nick Vieira, and Barb Williams. Tom Wood, Tom Gall, and Woody Peeples for their safety and medical support. Cracker Jack First Response Specialists facilitated logistics for the 2015 field portion. John Meyers and Dave Clarke coordinated porter teams. The over 100 personnel who facilitated the studies by portering scientific and expedition equipment to the summit and back, supported by Corvallis Mountain Rescue (OR), Deschutes Mountain Rescue (OR), Everett Mountain Rescue (WA), Hood River Crag Rats (OR), Olympic Mountain Rescue (WA), Portland Mountain Rescue (OR), Volcano Rescue Team (WA), Douglas County Sheriff's Mountain Rescue Unit (OR). Research and collecting permit from the United States Department of the Interior National Park Service–Mount Rainier.

REFEENCES

Anon., 1972, Climber reports change, Mount Rainier steam tunnels heating up, *in* Halliday, W.R., ed., The Cascade Caver, v. 12, no. 8, p. A-13.

Anderson, S.W., and Shean, D., 2022, Spatial and temporal controls on proglacial erosion rates: A comparison of four basins on Mount Rainier, 1960 to 2017: Earth Surface Processes and Landforms, v. 47, no. 2, p.596−617. https://doi.org/10.1002/esp.5274

Anderson, C.H., Vining, M.R., and Nichols, C.M., 1994, Evolution of the Paradise/Stevens Glacier Ice Caves: Bulletin of the National Speleological Society, v. 56, no. 2, p. 70–81.

Anderson, C. H., Behrens. C. J., Floyd, G. A., and Vining, M. R., 1998, Crater Firn Caves of Mount St. Helens, Washington: Journal of Cave and Karst Studies, v. 60, no. 1, p. 44–50.

Benn, D., Gulley, J., Luckman, A., Adamek, A., and Glowacki, P. S., 2009, Englacial drainage systems formed by hydrologically driven crevasse propagation: Journal of Glaciology, v. 55, no. 191, p. 513−523.

Capra, L., 2008, Abrupt climatic changes as triggering mechanisms of massive volcanic collapses: Journal of Volcanology and Geothermal Research, v. 155, p. 329–333. https://doi.org/10.1016/j.jvolgeores.2006.04.009

Cartaya, E., 2016, MRA Coalition Supports International Mount Rainier Cave Study: Meridian, San Diego, CA. p. 5−10.

Crandell, D. R., 1971, Postglacial lahars from Mount Rainier volcano, Washington: U.S. Geological Survey Professional Paper 677, Washington, DC: United States Government Printing Office, p. 75.

Curtis, A., 2020, Comparison of Earth's fumarolic ice caves, with implications for icy voids on other worlds [abs.]: 3rd International Planetary Caves Conference, San Antonio, Texas. 1 p.

Curtis, A., 2016, Dynamics and global relevance of fumarolic ice caves on Erebus Volcano, Antarctica [Ph.D. thesis]: Socorro, New Mexico Institute of Mining and Technology, https://aaroncurt.is/paper/curtis2016-phd_diss.pdf (Accessed 28 August, 2020).

Curtis, A., 2010, Erebus Cave and Fumarole Database. Available from: http://erebuscaves.nMountedu/ (Accessed April 12, 2021).

Curtis, A. and Kyle, P., 2017, Methods for mapping and monitoring global glaciovolcanism: Journal of Volcanology and Geothermal Research, v. 333–334, p. 134–144. https://doi.org/10.1016/j.jvolgeores.2017.01.017

Curtis, A. and Kyle, P., 2011, Geothermal point sources identified in a fumarolic ice cave on Erebus volcano, Antarctica using fiber optic distributed temperature sensing: Geophysical Research Letters, v. 38, no. 16, p. L16802. doi: 10.1029/2011GL048272

Davis, R., Anitori, R., Stenner, C., Smith, J., and Cartaya, E., 2020, Fumarolic glacial and firn ice caves on Mount St. Helens may provide insight into Martian subsurface microbial communities [abs.]: Analog Field Sites Mini Symposium, Houston, Texas. The Lunar and Planetary Institute, Open University Astrobiology, and NASA Johnson Space Center.

Edwards, B., Kochtitzky, W., Battersby, S., 2020, Global mapping of future glaciovolcanism: Global and Planetary Change, v. 195, p. 103356. https://doi.org/10.1016/j.gloplacha.2020.103356

Ewert, J.W., Diefenbach, A.K., and Ramsey, D.W., 2018, 2018 update to the U.S. Geological Survey national volcanic threat assessment: U.S. Geological Survey Scientific Investigations Report 2018–5140, 40 p. https://doi.org/10.3133/sir20185140

Finn, C. A., Sisson, T. W., and Deszcz-Pan, M., 2001, Aerogeophysical measurements of collapse-prone hydrothermally altered zones at Mount Rainier volcano: Nature, v. 409, p. 600–603. https://doi.org/10.1038/35054533

Fish, L., 2020, Compass Cave Survey Software for Windows [Computer software]. https://fountainware.com/compass/index.htm (Accessed August 28, 2020).

Florea, L., Pflitsch, A., Cartaya, E., and Stenner, C., 2021, Microclimates in fumarole ice caves on volcanic edifices—Mount Rainier, Washington, USA: Journal of Geophysical Research Atmospheres. v. 126, no. 4, p. 1−15. https://doi.org/10.1029/2020JD033565

Ford, D., and Williams, P. D., 2007, Karst Hydrogeology and Geomorphology: Chichester, West Sussex, England, John Wiley & Sons.

Frank, D., 1995, Surficial extent and conceptual model of hydrothermal system at Mount Rainier, Washington: Journal of Volcanology and Geothermal Research, v. 65, no. 1, p. 51−80. https://doi.org/10.1016/0377-0273(94)00081-Q

Gambino, S., Armienti, P., Cannata, A., Del Carlo, P., Giudice, G., Giuffrida, G., and Pompilio, M., 2021, Mount Melbourne and Mount Rittmann: Geological Society, London, Memoirs, v. 55, no.1, p. 741−758.

Giggenbach, W. F., 1976, Geothermal ice caves on Mt Erebus, Ross Island, Antarctica: New Zealand Journal of Geology and Geophysics, v. 19, no. 3, p. 365–372. https://doi.org/10.1080/00288306.1976.10423566

Gulley, J.D., and Fountain, A.G., 2019, Glacier Caves, *in* White, W.B., Culver, D.C., Pipan, T., eds., Encyclopedia of Caves, 3rd edition: Cambridge, Mass., Academic Press. https://doi.org/10.1016/B978-0-12-814124-3.00056-X.

Halliday, W.R., 2007. Pseudokarst in the 21st century: Journal of Cave and Karst Studies, v. 69, no. 1, p. 103−113.

Häuselmann, P., ed., 2012, UIS Mapping Grades. Version 2. Survey and Mapping Working Group, UIS Informatics Commission http://www.uisic.uis-speleo.org/UISmappingGrades.pdf (Accessed June 14, 2020).

Heeb B., 2009, An all-in-one electronic cave surveying device: Cave Radio and Electronics Group Journal, v. 72, p. 8-10.

Heeb, B., n.d., Paperless Cave Surveying. https://paperless.bheeb.ch/ (Accessed June 14, 2020).

Holler, C., 2019. Chapter 101 – Pseudokarst. *in* White, W.B., Culver, D.C., Pipan, T, eds., Encyclopedia of Caves, 3rd edition: Cambridge, Mass., Academic Press. https://doi.org/10.1016/B978-0-12-814124-3.00101-1

Hoblitt, R.P., Walder, J.S., Driedger, C.L., Scott, K.M., Pringle, P.T., and Vallance, J.W., 1998, Volcano hazards from Mount Rainier, Washington, revised 1998: U.S Geological Survey Open-File Report p. 98–428. https://pubs.usgs.gov/of/1998/0428/.

Hoffman, R., Woodward, A., Haggerty, P., Jenkins, K. J., Griffin, P. C., Adams, M.J., Hagar, J., Cummings, T., Duriscoe, D., Kopper, K., Riedel, J.L., Marin, L., Mauger, G., Bumbaco, K., and Littell, J.S., 2014, Mount Rainier National Park—Natural resource condition assessment: National Park Service, Natural Resource Report NPS/MORA/NRR-2014/894, 380 p.

Kiver, E.P., and Mumma, M.D., 1971, Summit firn caves, Mount Rainier, Washington. Science, v. 173. p. 320−322. https://doi.org/10.1126/science.173.3994.320

Kiver, E.P., and Steele, W.K., 1975, Firn caves in the volcanic craters of Mount Rainier: The National Speleological Society Bulletin. v. 37, no. 3. p. 45−55.

Korosec, M.A., 1989, Geothermal resource evaluation of Mount Rainier. Lacey, WA: U.S. Department of Interior, Bureau of Land Management, p. 61.

Le Guern, F., Ponzevera, E., Lokey, W, and Schroedel, R.D., 2000, Mount Rainier summit caves volcanic activity: Washington Geology, v. 28, no. 1/2, p. 25.

Liuzzo, M., Giudice, G., Giuffrida, A.C., 2018, Investigation of Ice-Caves on Melbourne and Rittman volcanoes, Antarctica [presentation]. European Geosciences Union General Assembly 2018, Vienna, Austria, 8−13 Apr. https://www.icevolc-project.com/presentations (Accessed April 8, 2021).

Lokey, W.M., 1973, Crater studies at a sleeping volcano: Explorers Journal., v. 51, p. 167−170.

Lokey, W.M., Mack, R., Miller, M.M., Prather, B.W. and Kiver, E.P., 1972, Project Crater: Mount Rainier glacio-volcanological research, 1970−72. [abs.]: Arctic and Mountain Environments Symposium, Michigan State University.

National Research Council, 1994, Mount Rainier: Active Cascade Volcano. Washington, D.C., The National Academies Press. https://doi.org/10.17226/4546

Nylen, T. H., 2004, Spatial and temporal variations of glaciers (1913−1994) on Mount Rainier and the relation with climate [Master's thesis]: Portland, OR, Portland State University.

Pflitsch, A., Cartaya, E., McGregor, B., Holmgren, D., and Steinhöfel, B., 2017, Climatologic studies inside Sandy Glacier at Mount Hood Volcano in Oregon, USA: Journal of Cave and Karst Studies, v. 79, no. 3, p. 189-206. http://dx.doi.org/10.4311/2015IC0135

Roberti, G., 2018, Mount Meager, a glaciated volcano in a changing cryosphere: hazards and risk challenges. [PhD. Thesis]: Earth Sciences, Université Clermont Auvergne. https://www.researchgate.net/publication/330980980_Mount_Meager_a_glaciated_volcano_in_a_changing_cryosphere_hazards_and_risk_challenges (Accessed August 18, 2020).

Sauro, F., Pozzobon, R., Massironi, M., De Berardinis, P., Santagata, T., De Waele, J., 2020, Lava tubes on Earth, Moon and Mars: A review on their size and morphology revealed by comparative planetology: Earth-Science Reviews, v. 209, p. 103288. https://doi.org/10.1016/j.earscirev.2020.103288

Scott, K.M., Vallance, J.W., and Pringle, P.T., 1995, Sedimentology, behavior, and hazards of debris flows at Mount Rainier: U.S. Geological Survey Professional Paper 1547, Washington, D.C.: U.S. Geological Survey, 56, p.

Sisson, T.W., Robinson, J.E., and Swinney, D.D., 2011, Whole-edifice ice volume change A.D. 1970 to 2007/2008 at Mount Rainier, Washington, based on LiDAR surveying: Geology, v. 39, p. 639–642. https://doi.org/10.1130/G31902.1

Sisson, T.W. and Vallance, J.W., 2009. Frequent eruptions of Mount Rainier over the last ~2,600 years: Bulletin of Volcanology, v. 71, no. 6, p. 595−618. https://doi.org/10.1007/s00445-008-0245-7

Sobolewski, L., Hansteen, T., Zorn, E., Stenner, C., Florea, L., Burgess, S., Ionescu, A., Cartaya, E., and Pflitsch, A., 2023, The evolving volcano-ice interactions of Crater Glacier, Mount St. Helens, Washington (USA): Bulletin of Volcanology, v. 85, no. 22. https://doi.org/10.1007/s00445-023-01632-5

Sobolewski, L., Stenner, C., Williams-Jones, G., Anitori, R., Davis, R., 2022a, Implications of the study of subglacial volcanism and glaciovolcanic cave systems: Bulletin of Volcanology, v. 84, no. 21. https://doi.org/10.1007/s00445-022-01525-z

Sobolewski, L., Stenner, C., Hüser, C., Berghaus, T., Cartaya, E., and Pflitsch, A., 2022b, Ongoing genesis of a novel glaciovolcanic cave system in the crater of Mount St. Helens, Washington, USA: Journal of Cave and Karst Studies, v. 84, no. 2, p. 51−65. https://doi.org/10.4311/2021ES0113

Stenner, C., Pflitsch, A., Florea, L., Graham, K., Cartaya, E., 2022, Development and persistence of hazardous atmospheres within a glaciovolcanic cave system—Mount Rainier, Washington, USA: Journal of Cave and Karst Studies, v. 84, no. 2, p. 66−82. https://doi.org/10.4311/2021EX0102

Stenner, C., Sobolewski, L., Pflitsch, A. and Cartaya, E., 2020, Morphology of a new system of glaciovolcanic caves—Mount St. Helens, Washington, USA, [C038-0001], American Geophysical Union, 2020 Fall meeting. https://www.essoar.org/doi/10.1002/essoar.10505755.1

Stevens, H., 1876, The ascent of Takhoma: Atlantic Monthly, Nov., p. 511−530.

Tebo, B. M., Davis, R. E., Anitori, R. P., Connell, L. B., Schiffman, P., and Staudigel, H., 2015, Microbial communities in dark oligotrophic volcanic ice cave ecosystems of Mount Erebus, Antarctica: Frontiers in Microbiology, v. 6, no. 179. https://doi.org/10.3389/fmicb.2015.00179

Tuffen, H., 2010, How will melting of ice affect volcanic hazards in the twenty-first century?, Philosophical Transactions of the Royal Society A, v. 368, p. 2535–2558. https://doi.org/10.1098/rsta.2010.0063

Unnsteinsson, T., 2022, Modelling glaciovolcanic caves and chimneys [M.Sc. thesis]: Burnaby, Simon Fraser University. https://www.sfu.ca/content/dam/sfu/volcanology/pdfs/Theses/Unnsteinsson_MSc'22.pdf (Accessed October 10, 2022).

Vallance J.W., Scott K.M., 1997, The Osceola mudflow from Mount Rainier: Sedimentology and hazards implications of a huge clay-rich debris flow: Geological Society of America Bulletin, v. 109, p. 143–163. https://www.morageology.com/pubs/59.pdf (Accessed July 5, 2023).

Wilkins, J., 1970, 2 Climbers Thread Needle, Penetrate Rainier Tunnels: Tacoma News Tribune, June 21, 1970: Tacoma, Washington USA.

Whittaker, J., 1957, Jim Whittaker letter to Dee Molenaar regarding exploration of Mount Rainier steam cave, January 15, 1957 https://www.omnia.ie/index.php?navigation_function=2andnavigation_item=04d5d055dee795a53479ec24bacf2b63andrepid=2 (Accessed May 4, 2021).

Wright, L.D., and Thom, B.G., 1977, Coastal depositional landforms: a morphodynamic approach: Progress in Physical Geography, v. 1, no. 3, p. 412−459.

Zimbelman, D.R., Rye, R.O., and Landis, G.P., 2000, Fumaroles in ice caves on the summit of Mount Rainier—preliminary stable isotope, gas, and geochemical studies: Journal of Volcanology and Geothermal Research, v. 97, p. 457–473, https://doi.org/10.1016/S0377-0273(99)00180-8

Julian J. Lewis and Salisa L. Lewis. Freshwater isopods of the genus *Lirceus* from caves and springs of the Interior Highlands, USA, with description of three new species (Isopoda: Asellidae). *Journal of Cave and Karst Studies*, v. 85, nos. 3/4, p. 86-101. DOI:10.4311/2022LSC0113

FRESHWATER ISOPODS OF THE GENUS *LIRCEUS* FROM CAVES AND SPRINGS OF THE INTERIOR HIGHLANDS, USA, WITH DESCRIPTION OF THREE NEW SPECIES (ISOPODA: ASELLIDAE)

Julian J. Lewis[1,2,C] and Salisa L. Lewis[2]

ABSTRACT

Eleven species of the freshwater isopod genus *Lirceus* occur in the Interior Highlands, a region of the south-central United States comprised of the Ozark and Ouachita physiographic provinces. As part of research on the morphology and molecular genetics of eastern North American asellid isopods, three new species of *Lirceus* were discovered in the Interior Highlands. *Lirceus slayorum*, n. sp., is described from Greathouse Spring, Washington County, Arkansas and occurs in caves and springs associated with the Ozark Springfield Plateau. *Lirceus ozarkensis*, n. sp., is described from Maxey Cave, Pulaski County, Missouri and was originally identified in 1949 by Hubricht and Mackin as a subspecies of *Lirceus hoppinae*. In actuality, *L. ozarkensis* is quite distinct from *L. hoppinae*, and occurs allopatrically in caves and springs of the southern Ozark Salem Plateau in southern Missouri. *Lirceus robisoni*, n. sp., is described from Abernathy Spring, Polk County, Arkansas and is found in only a few springs in a narrow area of the Ouachita Mountains in western Arkansas. Eight other species of *Lirceus* occur in the Interior Highlands, most of which are confined to springs and caves. New localities are presented and the ranges of the species are established. Illustrations of the genital pleopods demonstrate a common theme across the species of the Interior Highlands, with all possessing a sperm-transfer cannula arising adjacent to a variously papillate or dentate digitiform lateral process, and nestled under a dominant broadly rounded or subtriangular apex. Within this morphological template, some of the Ozark species, like *Lirceus bidentatus*, are among the most anatomically bizarre in North America.

INTRODUCTION

The isopod crustaceans of the genus *Lirceus* generally prefer cool, lotic waters and thus gravitate toward the groundwaters of caves, springs, and seeps. The region known as the Interior Highlands (Fig. 1), comprised of the Ozark and Ouachita physiographic provinces (Hunt, 1967), abounds in these habitats. The first *Lirceus* discovered in the Ozarks was described as *Asellus hoppinae* (Faxon, 1889). The species was discovered in a cave in Jasper County, Missouri by the remarkable Ruth Hoppin, who was also attributed with discovery of the Ozark cavefish *Troglichthys rosae*. Subsequently, Mackin and Hubricht (1938), described *Mancasellus ouachitaensis* from streams in the Ouachita Mountains of eastern Oklahoma, and documented *Asellus hoppinae* (Faxon) from several new sites in the Ozarks of northern Arkansas. Included in the publication of the new species by Mackin and Hubricht (1938) were descriptions and illustrations of the male second (genital) pleopod endopodite tip. By that point in time, it had been recognized that description of the male genitalia of isopods of the Family Asellidae was crucial in any characterization of a new species (Racovitza, 1920).

The largest contribution to the literature concerning *Lirceus* in the Interior Highlands was the monograph by Hubricht and Mackin (1949), who described five new species from the region.

It was their belief that *Asellus hoppinae* was a widespread species in the Interior Highlands, which was transferred to the genus *Lirceus,* with description of three subspecies: (1) *Lirceus hoppinae hoppinae*, occurring in southwestern Missouri and northwestern Arkansas; (2) *L. h. ouachitaensis* received *Mancasellus ouachitaensis*, in eastern Oklahoma; and (3) *L. h. ozarkensis* for populations in southcentral Missouri. All records of *Asellus hoppinae* from Mackin and Hubricht (1938) were assigned to *Lirceus bicuspidatus*, a new species described by Hubricht and Mackin (1949). The other species described by Hubricht and Mackin (1949) from the Interior Highlands were *Lirceus megapodus, L. bidentatus, L. trilobus* and *L. garmani*.

For reasons that now elude us, Hubricht and Mackin (1949) did not include the morphology of the male second (genital) pleopod in their species descriptions. This was problematic, as none of the species described by Hubricht and Mackin (1949) could be recognized or identified, and distribution patterns were impossible to ascertain for *Lirceus* species. Thus, this important group of isopods became a morass of unidentifiable species.

The purpose of this paper is to describe three new species of *Lirceus*, plus supplement the work of Hubricht and Mackin (1949) with illustrations of the male second pleopod endopodite for species of the Interior Highlands. This characterization of the species now allows accurate identification and delimitation of the ranges. This paper is a companion

[1]Research Associate, Department of Invertebrate Zoology, National Museum of Natural History, Smithsonian Institution, Washington, D.C. lewisbioconsult@gmail.com
[2]Lewis and Associates—Cave, Karst and Groundwater Biological Consulting, Borden, Indiana, thefirstfeed@gmail.com
[C]Corresponding Author

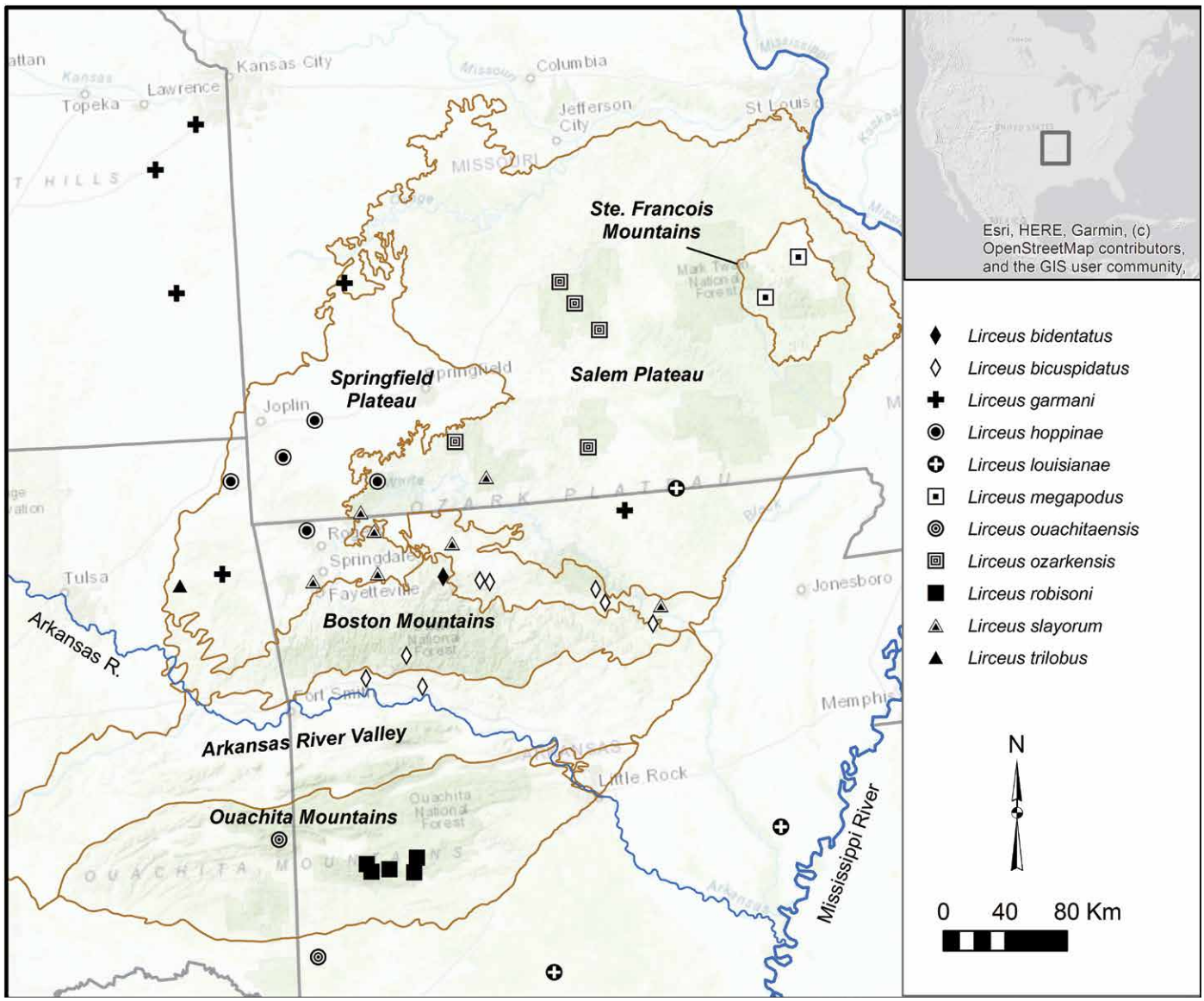

Figure 1. Map of occurrence of *Lirceus* species in the Interior Highlands.

to a monograph of the groundwater isopods of Virginia and the surrounding Appalachian region (Lewis, et al., 2023). Molecular phylogenetic analysis of the asellids of eastern North America, which is included in the Virginia monograph, confirms the status of the genus *Lirceus* as a monophyletic group. Fresh material was collected for all Interior Highland species except *Lirceus trilobus,* and molecular analysis demonstrated divergence greater than 0.16 substitution per site in the mitochondrial cytochrome oxidase 1 gene, as measured by patristic distances (Douady, C.J. and Malard, F., unpublished data). Thus, not only are all taxa herein morphologically distinct species, the molecular genetic analysis strongly supports these species (Lefébure et al., 2006).

MATERIALS AND METHODS

Specimens for this research were obtained from several sources, the richest of which was the collection of the National Museum of Natural History (USNM), Smithsonian Institution, maintained at the Smithsonian Museum Support Center in Suitland, Maryland. There we found the type specimens and other material collected by Leslie Hubricht and utilized in the monograph of Hubricht and Mackin (1949). The type specimens of *Lirceus hoppinae* were obtained on loan from the Museum of Comparative Zoology, Harvard University, in Cambridge, Massachusetts.

Other specimens were contributed by Henry W. Robison (Professor Emeritus, Southern Arkansas University), Michael Slay (The Nature Conservancy), Michael Sutton (Cave Research Foundation), and collections of the authors. All new material was placed in the collection of the Smithsonian Institution.

The precision of some cave-associated localities is restricted per state cave surveys (National Speleological Society internal organizations) to county level to protect the security of cave entrance location information. Where distances were included in localities, the collection vial label information was copied verbatim for clarity in future retrieval of the specimens, with the English system if measurement retained when used by the collector ("mile" was abbreviated as "mi.").

The isopods were examined using a Leica stereo dissecting microscope, with appendages for illustration removed and placed in temporary glycerin mounts on glass microscope slides. These were then placed on a Leica compound microscope with an optical drawing tube, with which pencil drawings were prepared. The drawings were then inked, scanned, and placed into plates with Adobe Illustrator.

DNA sequencing of the asellid species of the Interior Highlands discussed herein was conducted as part of the extensive molecular phylogenetic work presented by Lewis et al. (2023), and detailed procedures are included there. Inferences presented here are from sequencing of the mitochondrial 16S and CO1 genes, plus nuclear Fast2 and 28S rDNA genes. The sequences were deposited in Genbank (National Center for Biotechnology Information (NCBI), National Institutes of Health (NIH)) and accession numbers are presented with the new species descriptions. The molecular phylogeny of the *Lirceus* species of the Interior Highlands is included in Lewis, et al. (Fig. 8, 2023), including references to the molecular operational taxonomic units (MOTUs).

Figure 2. S. L. Lewis using a dipnet to collect the type series of *Lirceus slayorum* from organic debris in the spring run of Greathouse Springs, Washington Co., Arkansas.

SYSTEMATICS

Lirceus Rafinesque, 1820

Lirceus slayorum, new species

Lirceus hoppinae ozarkensis.—Hubricht and Mackin, 1949: 344 [Bear Creek Springs record]

Lirceus hoppinae sensu latu.—Graening, et al., 2007: 9 [in part]

Material examined: ARKANSAS: Benton Co.: Electric Springs, 1.2 mi. NE Rogers, M. E. Slay, C. M. Slay, 12 Nov 2004, 1♂1♀; Boone Co.: Bear Creek Springs, J. J. Lewis, S. L. Lewis, 18 Jun 2016, 11♂♀; Carroll Co.: Sweet Spring, on Spring Street, Eureka Springs, J. J. Lewis, S. L. Lewis, 17 Oct 2017, 1♂; same locality and collectors, 19 Oct 2017, 2♀; Independence Co.: Spring Mill Run (Big Spring), 6.2 mi. NW Batesville, J. J. Lewis, S. L. Lewis, 11 May 2022; Madison Co.: Withrow Springs, 4.9 mi. N Huntsville, J. J. Lewis, S. L. Lewis, 18 Jun 2016, 1♀. Washington Co.: Greathouse Springs, 5.7 mi. NNW Fayetteville, J. J. Lewis, S. L. Lewis, 16 Jun 2016, 60♂♀; same locality, M. E. Slay, 7 Aug 2018, 42♂♀. MISSOURI: Barry Co.: spring branch below entrance of Twilight Joint Cave, M. Sutton, 25 Aug 2001, 1♂1♀; Taney Co.: Spring Cave, stream in entrance zone, M. Sutton, 11 Dec 2004, 1♂.

Type material: Holotype ♂ (USNM 1508058) and 59♂♀ paratypes (USNM 1436126) collected 16 June 2016, and 42♂♀ paratypes (USNM 1607414) collected 7 August 2018, from Greathouse Springs, Washington Co., Arkansas (Figs. 1 and 2) located at N36.13951 W94.19803, deposited in the collection of the Smithsonian Institution. Genbank (NCBI) accession numbers of material sequenced from the type-locality at Greathouse Springs are 16S: OX383329, OX383330, OX383331; CO1: OX383323, OX383324; 28S: OX383342, OX383343; Fast2: OX383337, OX383338.

Diagnosis: Separated from its geographic neighbors by its 1-merous mandibular palp, which is 3-merous in *L. hoppinae* and *L. bicuspidatus*. The pleopod 2 endopodite tip of *L. slayorum* and *L. hoppinae* possesses a subtriangular caudal

process in both species, but the cannula in *L. slayorum* is short and emerges from the center of the space between the mesial and lateral processes, while it is longer and emerges from the side of the lateral process in *L. hoppinae*. The closest genetic relative of *L. slayorum* (indicated as MOTU 452 *Lirceus* undescribed species by Lewis, et al., Figure 8, 2023) is *L. hoppinae*.

Description: Length to 8.0 mm, body 2.8× as long as wide, grayish-brown pigmentation dorsally, darkest on anterior of head, head and pereonites with stippled appearance along lateral margins, otherwise with mottled pattern darkest along midline, pleotelson with stippled, granular appearance (Fig. 3). Head with distinct eyes, lateral margins entire, incisions not apparent in dorsal view, lateral incision suture line visible in ventral view. Antenna 1 flagellum of 7 articles, reaching to distal margin of penultimate article of antenna 2, distal five articles with one aesthetasc each. Mandibular palp 1-merous with apical seta (Fig. 4).

Figure 3. Living specimen of *Lirceus slayorum*, length approximately 8 mm, from Greathouse Springs, Washington Co., Arkansas illustrating dorsal pigmentation pattern and relative proportions of appendages (photo by Michael Slay, The Nature Conservancy).

Pereopod 1, propodus about 1.6× as long as wide, palmar margin with stout proximal spine, medial process large, subtriangular, apically blunt, distal process low, broadly rounded; dactylus, flexor margin weakly spinose, 3−4 larger spines distally, decreasing in size proximally.

Pleotelson broader proximally, tapering distally, about 1.1× wider than long; caudomedial lobe modestly produced, broadly rounded, uropodal sinuses present. Pleopod 1, protopod with 4−5 retinaculae, exopod about 1.3× longer than protopod, about 0.67× as wide as long, setae longest on lateral margin, decreasing in length then increasing at apex. Pleopod 2, protopod with single seta on distal-mesial margin; exopod, proximal article without setae; distal article subtriangular, relatively elongate, about 1.4× as long as wide, apex blunt, about 11 elongate setae along lateral and apical margins; endopod tip subtriangular, tapering to a rounded caudal process, cannula small but distinct, cylindrical, extending from bowl formed between base of lateral and mesial processes, base of cannula obscured by lateral dentate/papillate curved digitiform process, mesial process with a short knob at base, main process a broad lobe slightly longer than lateral process. Pleopod 3, exopod with many setae along lateral and apical margins, longest distolaterally, shortest setae along apical margin, anterior surface sparsely setose with smaller setae. Pleopod 4, exopod with sigmoid suture with weak lines dividing lateral and apical margins into four parts; proximal section with 15 setae, mesial section with 18 setae, distolateral section with 7 setae, apical margin without setae. Pleopod 5, exopod with 4 proximolateral setae proximal to weak lateral false suture.

Uropods equal or slightly longer than pleotelson, protopod flattened, exopod and endopod slightly flattened; endopod equal in length to protopod, exopod about 0.75× length of endopod.

Etymology: This species is named in honor of Christy Melhart Slay (The Sustainability Consortium) and Michael Slay (The Nature Conservancy), in recognition of their dedication to environmental conservation and sustainability. Suggested vernacular name is Slays' spring isopod.

Habitat and range: This species is endemic to the karst of the Ozark Springfield Plain in northern Arkansas and the adjacent part of the southwestern Salem Plateau in Missouri, spanning a range of about 140 miles (225 km). Preliminary analysis of the 16S mitochondrial gene of a sample from the eastern edge of the range (Independence County) suggests that population is an undescribed cryptic species included here within the morphospecies *L. slayorum*.

At Greathouse Spring (Fig. 2) the isopods were abundant on rocks and sticks in the spring run along Arkansas State Highway 112. Elsewhere *L. slayorum* occurs in cave entrances and springs, where it typically inhabits stream gravels and the undersides of stones

***Lirceus ozarkensis* Hubricht and Mackin, 1949, new status, new species**

Lirceus hoppinae ozarkensis Hubricht and Mackin, 1949: 336, 344; Williams, 1972: 14.

Material examined: MISSOURI: Christian Co.: Cascade Spring Cave, M. Sutton, 19 Feb 2000, 2♂; Rattlesnake Cave, M. Sutton, 19 Feb 2000, 1♂; Ozark Co.: Bat Cave, M. Sutton, 20 Sep 2003, 1♂; same locality and collector, 6 Mar 2004, 1♂; Pulaski Co.: stream at mouth of Maxey Cave, 2 mi. N Hanna, L. Hubricht, 8 Oct 1939, 78♂♀; Fort Leonard Wood: Sand Boil Spring, M. E. Slay, S. Taylor, 12 May 2004, 5♂ 1 juvenile; *Lirceus* Shelter, M. E. Slay, S. Taylor, 13 May 2004, 2♂2♀; Defile Spring, S. Taylor, M. E. Slay, V. R. Block, 19 Apr 2003, 5♂2♀; Kerr Cave, S. Taylor, V. R. Block, 26 Mar 2003,

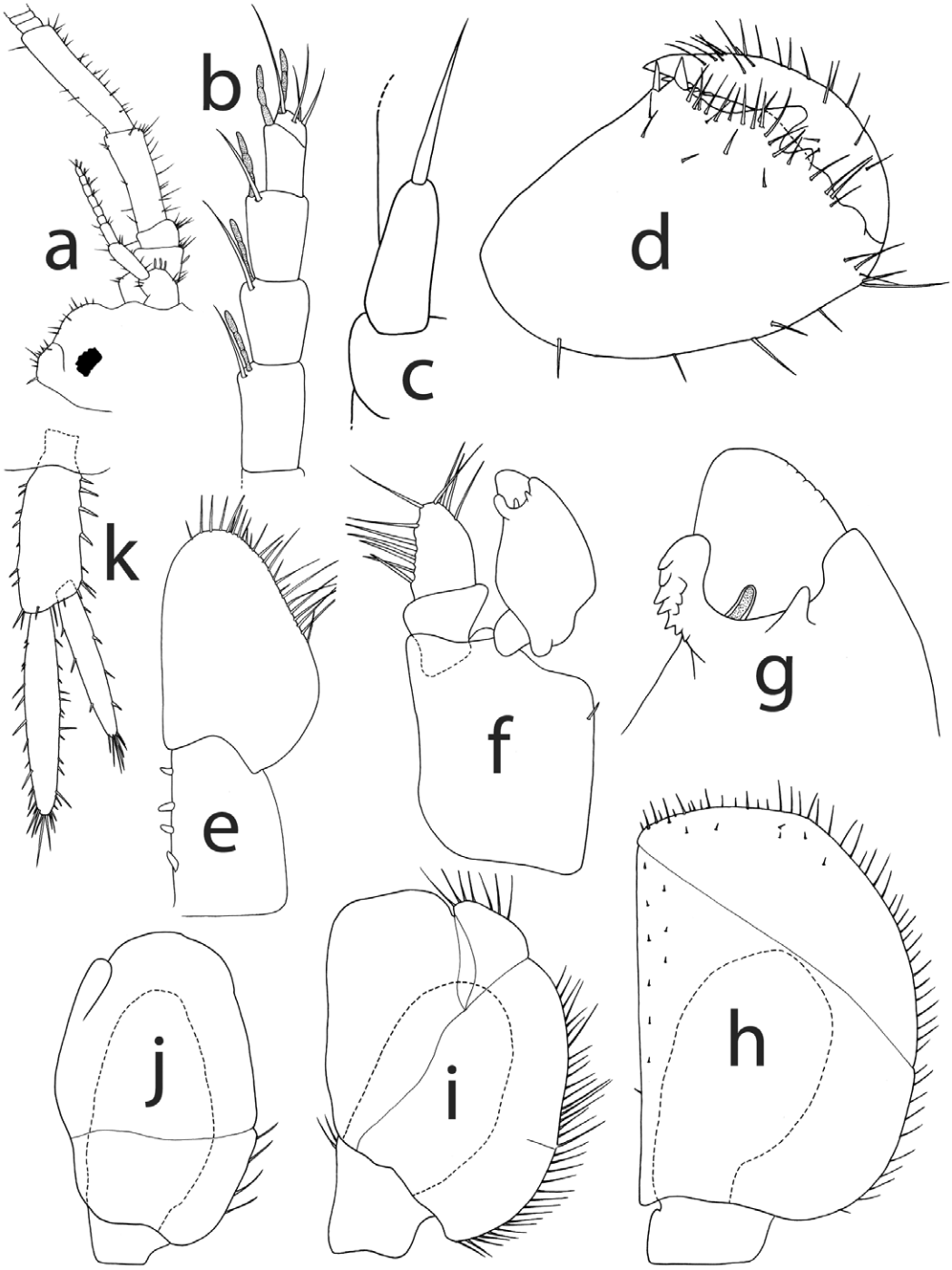

Figure 4. *Lirceus slayorum*, n. sp., Greathouse Springs, Washington Co., Arkansas: (a) head, antenna 1, antenna 2 peduncle (pigmentation omitted), (b) antenna 1 distal articles, (c) mandibular palp, (d) pereopod 1, propodus and dactylus, (e) pleopod 1, (f) pleopod 2, (g) pleopod 2 endopodite tip, (h) pleopod 3, (i) pleopod 4, (j) pleopod 5 and (k) uropod.

1♂3♀; Texas Co.: Bat Cave, from spring mouth of cave, L. Hubricht, 5 Jul 1940, 12♂♀; Boiling Springs, 5.5 mi. ENE Success, J. J. Lewis, S. L. Lewis, 14 Oct 2017, 12♂♀.

Type material: Syntypes 78♂♀ specimens (USNM 1254684) from Maxey Cave, Pulaski Co., Missouri, deposited in the Smithsonian Institution by Hubricht and Mackin (1949). The specimens from the type-locality were believed to be a subspecies of *Lirceus hoppinae* by Hubricht and Mackin (1949), however our analysis revealed that neither the morphology nor genetics were conspecific with that species. The subspecies is elevated to the status of new species. Genbank (NCBI) accession numbers of material sequenced from Boiling Springs, Texas County, Missouri, are 16S: OX383334; CO1: OX383325, OX383326; 28S: OX383344, OX383345; Fast2: OX383339, OX383340.

Diagnosis: This species is distinguished from *L. hoppinae* by the apex of the male second pleopod endopod, which is broadly rounded in *L. ozarkensis*, but subtriangular in *L. hoppinae*. The mandibular palp of *L. ozarkensis* possesses 1 article, whereas it is 3-merous in *L. hoppinae* and *L. bicuspidatus*, the allopatric neighbors in southwestern Missouri and adjacent Arkansas. *Lirceus slayorum* also has a 1-merous mandibular palp, but is separable by its pleopod 1 with retinaculae, which are absent in *L. ozarkensis*. The closest genetic relative of *L. ozarkensis* (indicated as MOTU 368 *Lirceus* undescribed species by Lewis, et al., Figure 8, 2023) is *L. louisianae. Lirceus ozarkensis* is readily separated from *L. louisianae* by the latter's lack of a mandibular palp.

Description: Length to 19 mm, body 2.6× as long as wide, pigmentation darkest on anterior part of head, pereonites with brown mid-line stripe, mottled light areas on either side blending into darker gray area on margins, pleotelson with stippled pattern of relatively large blotches of grayish pigment. Head with eyes distinct, lateral incisions prominent. Man-

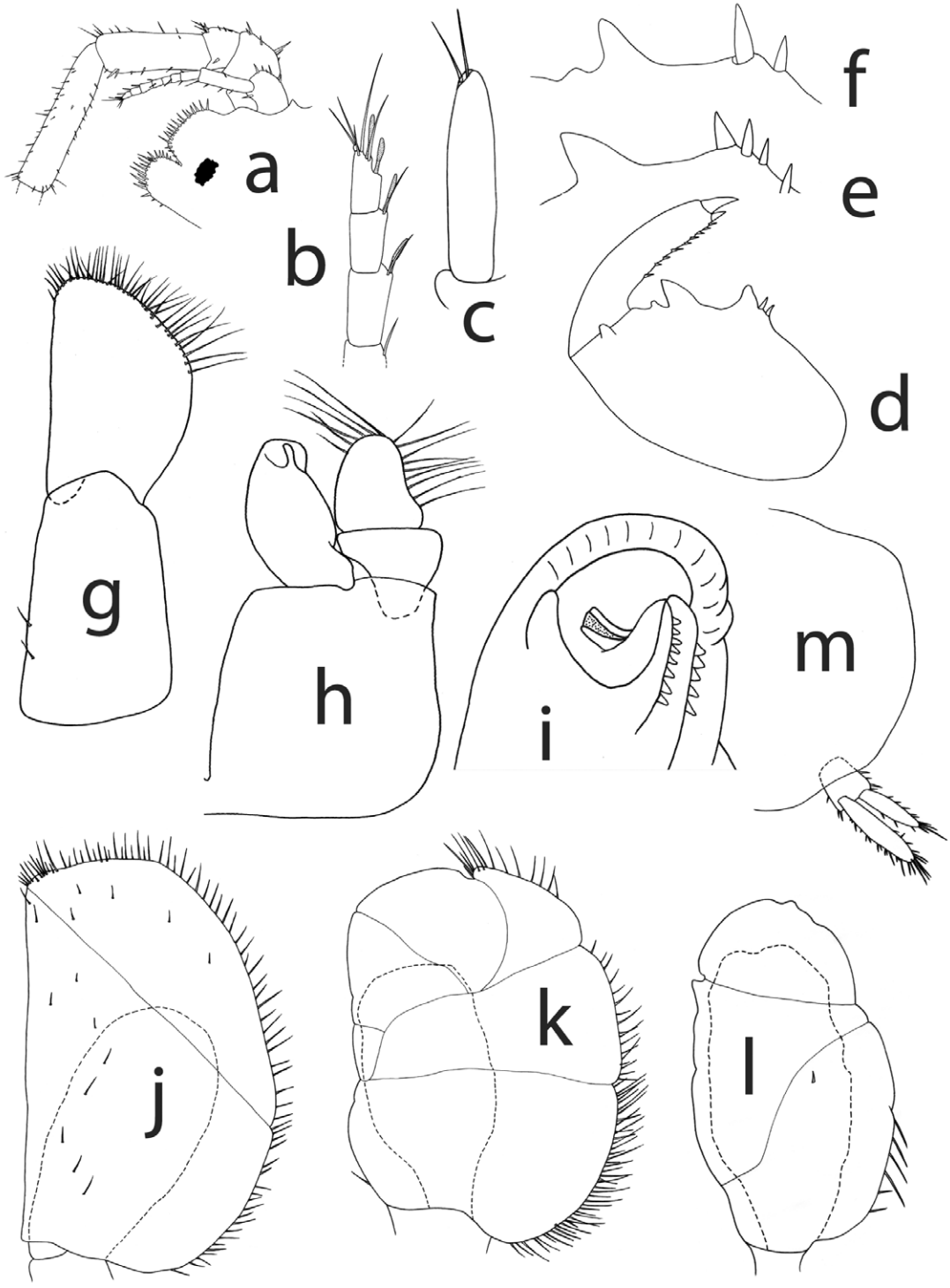

Figure 5. *Lirceus ozarkensis*, n. sp., Maxey Cave, Pulaski Co., Missouri: (a) head, antenna 1, antenna 2 peduncle (pigmentation omitted); (b) antenna 1 distal articles; (c) mandibular palp; (d) pereopod 1, propodus and dactylus (setation omitted); (e) same, palmar margin; (f) same, palmar margin; (g) pleopod 1; (h) pleopod 2; (i) same, endopodite tip; (j) pleopod 3; (k) pleopod 4; (l) pleopod 5, and (m) pleotelson and uropod.

dibular palp 1-merous. Antenna 1 flagellum of 6−7 articles, reaching to distal margin of penultimate article of antenna 2, distal four articles each bearing one aesthetasc (Fig. 5).

Pereopod 1, propodus about 1.6× as long as wide, palmar margin with proximal spine or subtriangular process, separated by wide cleft from subtriangular medial process ranging from about the same height in individuals with proximal spine or slightly higher if proximal process is present, separated by u-shaped cleft from low distal rounded knob; dactylus, flexor margin with 9−10 small spines increasing in size distally.

Pleotelson widest proximally, tapering distally, about 0.8× as long as wide, caudomedial lobe broadly rounded, uropodal sinuses modestly developed. Pleopod 1, protopod without retinaculae, exopod about 0.9× length of protopod, distolateral marginal setae decreasing in length distally. Pleopod 2, exopod distal article subovate, 1.4× as long as wide, apex broadly rounded, about 17 elongate setae along margin; endopod apex broadly rounded, rugose laterally; cannula distinct, slightly conical, tapering slightly distally, extending variably from perpendicular to obliquely to the axis of the endopod, arising from mesial wall of lateral process; lateral process relatively large, obstructing cannula in anterior aspect, dentate along medial and lateral margins; mesial process digitiform. Pleopod 3, exopod with many setae along lateral and apical margins, anterior surface sparsely setose with smaller setae. Pleopod 4, exopod with weak, difficult to discern false suture lines dividing lateral and apical margins into four parts; proximal section with >40 setae,

Figure 6. Panoramic photo (collage of 5 images) of Abernathy Spring, Polk County, Arkansas. The water emerges from a 30-inch diameter pipe in the upper right of the photo (red arrow). Approximately three meters of the spring downstream from the orifice the substrate is monopolized by a microbial mat, which is then replaced by a variety of emergent green plants in which the isopods occur. An 8-inch sieve and plastic containers are present in the lower right side of the photo for scale.

mesial section with 17 setae, distolateral section with 14 setae, apical margin without setae. Pleopod 5, exopod with 6 proximolateral setae proximal to weak sigmoid false suture and second distal transverse false suture.

Uropods up to 0.7× length of pleotelson; protopod flattened, endopod up to 1.4× longer than protopod.

Etymology: The name of this species refers to its occurrence in the Ozark Plateaus. Suggested vernacular name is the Ozark spring isopod.

Habitat and range: Lirceus ozarkensis occurs in southcentral Missouri in the western part of the Ozark Salem Plateau (Fig. 1). Hubricht and Mackin (1949) presented records from Laclede and Maries counties that remain unconfirmed, but seem reasonable. The type-locality was commercialized under the name Inca Cave, then acquired by the Missouri Department of Conservation in 2011 and designated Great Spirit Cave Conservation Area.

This species is known from springs and the entrance zone of caves. At Boiling Springs, Texas County, we found *Lirceus ozarkensis* in the entrance of a mostly water-filled cave by digging about 15 cm below the surface into gravel interstices. In this subsurface habitat *L. ozarkensis* was found with the stygobiontic species *Caecidotea salemensis* and *C. antricola*.

***Lirceus robisoni*, new species**

Lirceus ouachitaensis.—Lewis, 1983: 152.

Material examined: ARKANSAS: Montgomery Co.: Collier Springs, 5.2 mi. ENE Norman, H. W. Robison, 16 Jun 1979, 30♂♀; same locality and collector, 24 Aug 2018, 26♂♀; Ida Sublette Spring, Caddo Gap, H. W. Robison, 24 Aug 2018, 32♂♀; small rocky stream adjacent to parking area for Little Missouri Falls, 21.5 mi. ESE Mena, J. J. Lewis, S. L. Lewis, 13 May 2022, 2♂5♀; unnamed spring at Arkansas Game and Fish Commission boat launch on Caddo River, in Caddo Gap, H. W. Robison, 24 Aug 2018, 11♂♀; Polk Co.: Abernathy Spring, H. W. Robison, 21 Dec 2018, 17♂♀; same locality and collector, 23 Aug 2018, 4♂♀; same locality and collector, 16 Jun 1979, 100+♂♀; same locality, J. J. Lewis, S. L. Lewis, 13 May 2022, 44♂♀; Boxx Spring, on Forest Road 73, 1.2 mi. from state highway 8, H. W. Robison, 23 Aug 2018 7♂6♀; same locality and collector, 21 Dec 2018, 36♂♀.

Type material: Holotype ♂ (USNM 1607404), 17♂♀ paratypes (USNM 1607405; USNM 1608025), and 44♂♀ paratypes (USNM 1593460), from Abernathy Spring, 0.8 mi. west of the Polk-Montgomery Co. line, on the north side of Highway 8 (N34.46816 W93.94798), were deposited in the collection of the Smithsonian Institution. Genbank (NCBI) accession numbers for material sequenced from the type-locality at Abernathy Spring are 16S: OX383335, OX383336; CO1: OX383327, OX383328; 28S: OX383346; Fast2: OX383341.

Diagnosis: An eyed and pigmented species most closely related to *L. bicuspidatus*, from which *L. robisoni* is separated by the male second pleopod endopodite tip with the cannula extending parallel to the axis of the endopodite, and well beyond the margin of the tip, whereas in *L. bicuspidatus* the cannula extends obliquely and is nested among the endopodite tip processes. In *L. robisoni* the palmar margin of pereopod 1 has rounded processes, in large specimens with a shoulder on the medial process (Fig. 8), but not distinctly bi-cuspate as in *L. bicuspidatus*. The closest genetic relative of *L. robisoni* (indicated as MOTU 417 *Lirceus* undescribed species by Lewis, et al., Figure 8, 2023) is *L. bicuspidatus*.

Figure 7. Photo of a living *Lirceus robisoni*, approximately 9 mm in length, from Abernathy Spring, Polk County, Arkansas, illustrating the dorsal pigmentation pattern and proportions of the habitus and appendages.

Description: Length of males to 13.5 mm, ovigerous females to 6.6 mm, body 2.8× as long as wide; dorsal pigmentation darkest on anterior of head (Fig. 7), anterior and lateral margins of head and pereonites unmottled, central and posterior parts of head with mottling, pereonites with moderately pigmented longitudinal midline band with adjacent mottling, margins pigmented, but unmottled, pleotelson darkest in midline, stippled in appearance without pattern. Head with eyes prominent; lateral incisions closed, post-mandibular lobe not apparent, margin of head appears entire. Antenna 1 reaching to distal margin of penultimate article of antenna 2, flagellum of 6 articles, distal 4 each with one aesthetasc. Mandibular palp 3-merous (Fig. 8).

Pereopod 1, propodus about 1.6× as long as wide, palmar margin with prominent proximal spine or process and 1−2 smaller spines, medial process large, rounded or with shoulder in large specimens, separated by U-shaped cleft from lower rounded process; dactylus with subungual spine about half the length of unguis, smaller spines decreasing in size along flexor margin.

Pleotelson subtrapezoidal (Figs. 7 and 9), about 0.8× as long as wide, tapering posteriorly, caudomedial lobe broadly rounded, uropodal sinuses moderately produced. Pleopod 1 longer than pleopod 2, protopod with

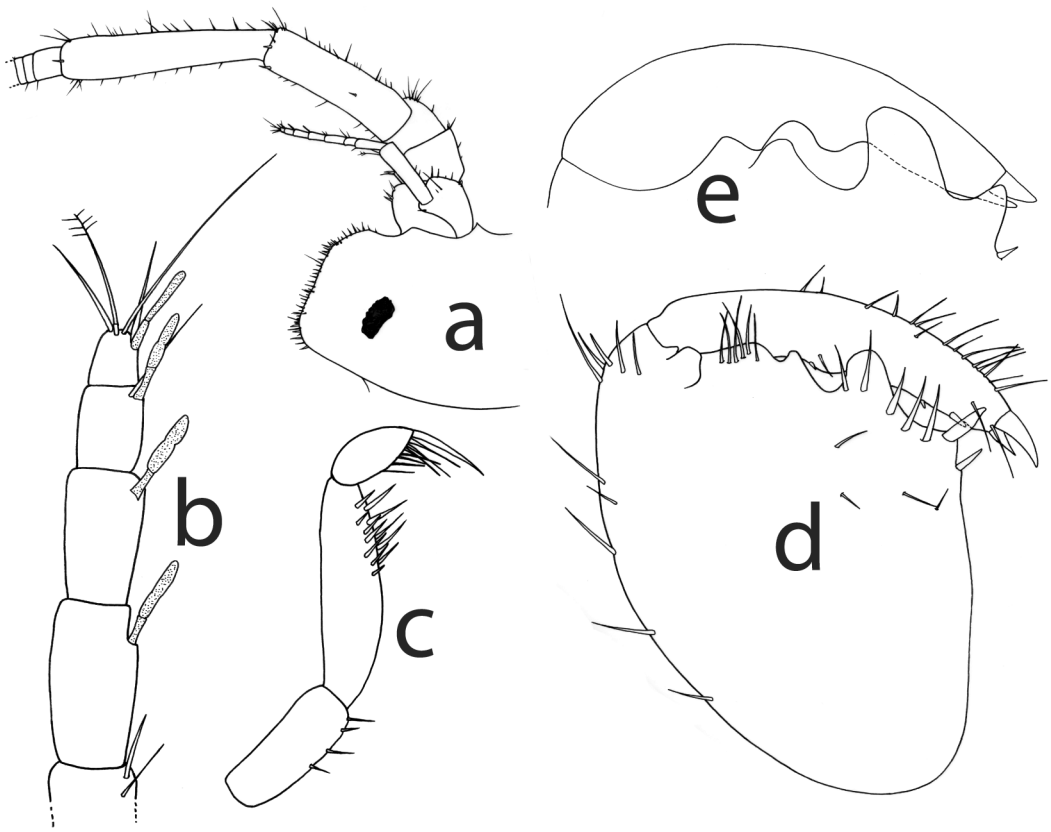

Figure 8. *Lirceus robisoni*, n. sp., Abernathy Spring, Polk Co., Arkansas: (a) head, antenna 1, antenna 2 peduncle (pigmentation omitted); (b) antenna 1 distal articles; (c) mandibular palp; (d) pereopod 1, propodus and dactylus (e) same, palmar margin of different specimen (setation omitted).

3 retinacula, exopod about 1.2× length of protopod, 0.6× as wide as long, setae longest on distolateral margin, decreasing in length slightly at apex (Fig. 9). Pleopod 2, protopod without setae, minute spines along distomesial margin; exopod proximal article without setae, distal article subovate, apex rounded, about 1.5× as long as wide, distal-lateral and apical margins with about 14 elongate setae; endopod, widest medially, tip cannula distinct, cylindrical, extending beyond margin of caudal process approximately parallel to the axis of the endopod; caudal process broadly rounded; lateral process extending diagonally, densely papillate/denticulate. Pleopod 3, exopod with many setae along lateral and apical margins, anterior surface sparsely setose with smaller setae. Pleopod 4, exopod with weak sigmoid false suture dividing lateral and apical margins into four parts; proximal section with >40 setae, mesial section with >20 setae, distolateral section with 13 setae, apical margin without setae. Pleopod 5, exopod with 2 mediolateral setae proximal to weak sigmoid false suture.

Uropods to 0.5× length of pleotelson, protopod flattened, mostly visible beyond margin of pleotelson in dorsal view, exopod and endopod slightly flattened; endopod about 1.5× length of protopod, exopod 0.9× length of endopod.

Etymology: Named in honor of Dr. Henry W. Robison, Professor Emeritus at Southern Arkansas University, collector of the type series of this species, as well as previously discovering *Caecidotea fonticulus* at Abernathy Spring (Lewis, 1983). Suggested vernacular name is Robison's spring isopod.

Habitat and range: Lirceus robisoni is known from six localities in the Ouachita Mountains on the north side of the Caddo Mountains, in Polk and Montgomery counties, Arkansas. Five of the localities are springs, along with one small (possibly spring-fed) stream. At the type-locality, the waters of Abernathy Spring emerge from the fractured Bigfork chert formation at the faulted contact with the underlying Womble shale (both Ordovician). A 30-inch (76 cm) diameter vertical pipe provides a well-like situation historically used as a domestic drinking water supply. Abernathy Spring discharges approximately 30 gallons per minute (Arkansas Geological Survey, 1937) at 16 °C (Wagner and Steele, 1980). McAllister (2020) described the site as a mineral spring, with iron (ferrous) carbonate the primary chemical constituent.

We visited Abernathy Spring on 13 May 2022. At that time the substrate for about the first three meters downstream from the spring orifice was covered with a thick, brownish-orange flocculent microbial mat that was not inhabited by isopods (Fig. 6). Beyond that point emergent plants filled the spring run and *L. robisoni* was common on the vegetation. The substrate was comprised of gravels in which were found both *L. robisoni* and the endemic stygobiontic *Caecidotea fonticulus* (Lewis, 1983).

***Lirceus hoppinae* (Faxon, 1889)**

Asellus hoppinae Faxon, 1889: 232, 237−238, plate II.—Mackin and Hubricht, 1938: 632.

Asellus incisus.—Van Name, 1936: 464−465

Mancasellus incises.—Mackin, 1940: 17.

Lirceus hoppinae hoppinae.—Hubricht and Mackin, 1949: 336, 343, 349; Williams, 1970: 73; 1972: 14.

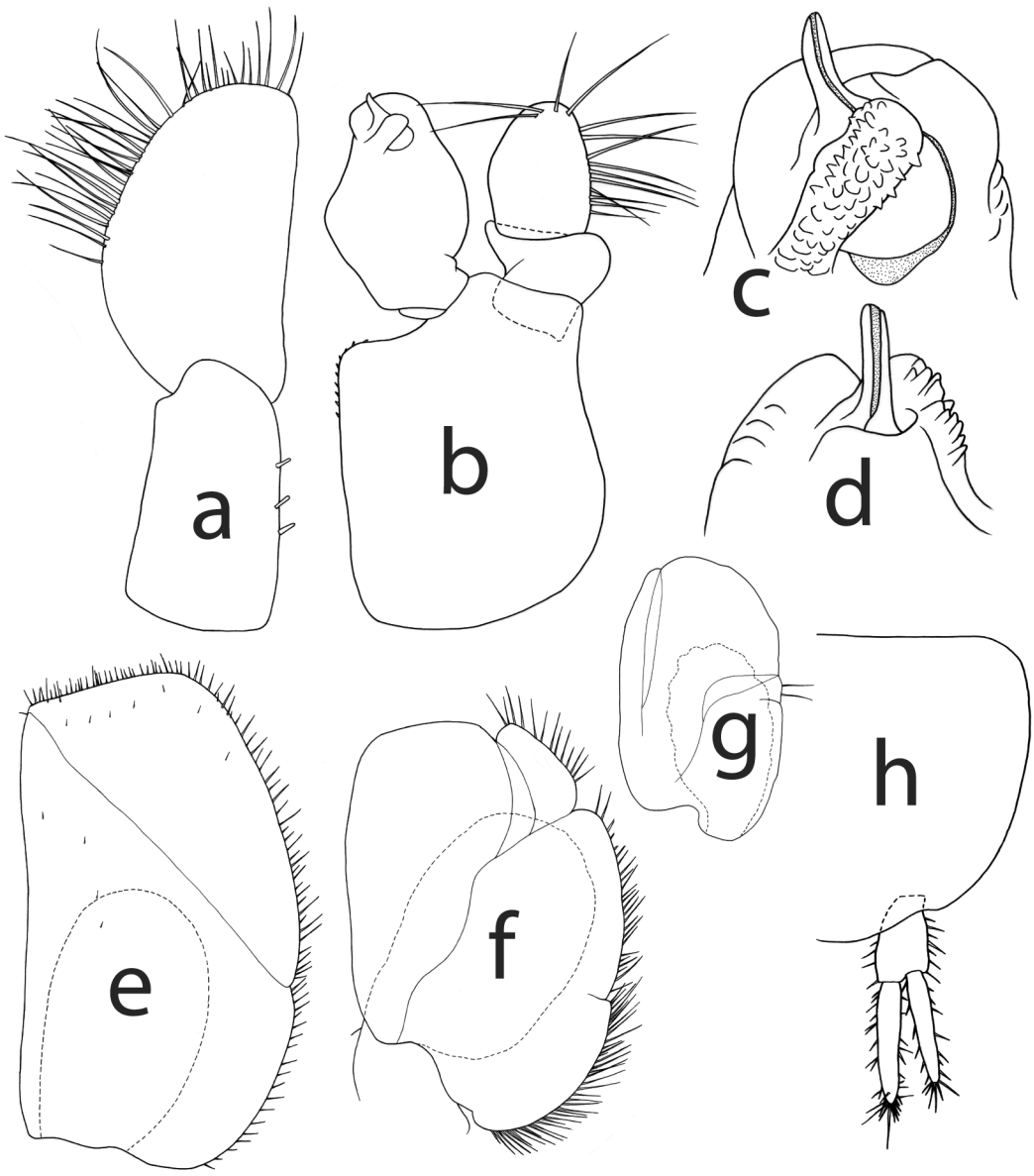

Figure 9. *Lirceus robisoni*, n. sp., Abernathy Spring, Polk Co., Arkansas: (a) pleopod 1; (b) pleopod 2; (c) pleopod 2 endopodite tip; (d) same, rotated laterad; (e) pleopod 3; (f) pleopod 4; (g) pleopod 5; (h) pleotelson and uropod.

Lirceus hoppinae.—Pennak, 1978: 446; Graening, et al, 2011: 61, 159.

Lirceus hoppinae sensu latu.—Graening, et al., 2007: 3, 9 [in part].

Material examined: ARKANSAS: Benton Co.: Big Spring, Bella Vista, L. Hubricht, 7 May 1940, 40♂♀. MISSOURI: Barry Co.: Mushroom Rock Cave, M. Sutton, 10 May 2002, 1♂1♀; spring near Dogwood Blossom Cave, M. Sutton, 11 Mar 2019, 1♂; Hidden Salamander Cave, M. Sutton, 2 Dec 2019, 1♀; Wet Foot Cave, M. Sutton, 2 Dec 2019, 1♂1♀; spring near Cobblestrewn Cave, M. Sutton, 2 Dec 2018, 1♀; Jasper Co.: Day's Cave, Sarcoxie, in mud under stones, R. Hoppin, date unknown, 4♂; same locality, L. Hubricht, 22 May 1942, 75♂♀; Newton Co.: Hearrell Spring, Neosho National Fish Hatchery, J. J. Lewis, S. L. Lewis, 16 Oct 2017, 20♂♀; Big Spring, Neosho, J. J. Lewis, S. L. Lewis, 16 Oct 2017, 1♂ 5♀; spring 1.4 mi. N of Tipton Ford, L. Hubricht, 9 May 1940, 58♂♀. OKLAHOMA: Ottawa Co.: Schifflet Cave, G. Graening, D. Fenolio, 6 Dec 2003, 4♂; Cave Springs Ranch Cave, G. Graening, D. Fenolio, 14 Dec 2003, 4♂.

Type material: Syntypes 4♂ (Faxon, 1889) collected by Ruth Hoppin from Day's Cave, Jasper Co., Missouri (N37.06988 W94.11871), in the collection of the Museum of Comparative Zoology (MCZ 4203), Harvard University, Cambridge, Massachusetts.

Diagnosis: The 3-merous mandibular palp separates the species from *L. slayorum*, with 1-merous mandibular palp. The pleopod 2 endopodite of *L. hoppinae* (Fig. 10a, b) has a prominent subtriangular caudal process with the elongate cannula extending at an oblique angle from the base of the papillate lateral process. In *L. slayorum* the cannula is shorter and nestled between lateral and mesial processes.

Habitat and range: The range of this species is restricted from that envisioned by Hubricht and Mackin (1949) as encompassed by three subspecies of *Lirceus hoppinae* to a smaller region of southwestern Missouri, northwestern Arkansas, and adjacent Oklahoma, corresponding to a portion of the Ozark Springfield Plateau (Fig. 1). The isopods inhabit springs and caves, usually near the entrance. The type-locality, Day's Cave (also known as Dowler or Sarcoxie cave) is in the Sarcoxie Cave and Spring Preserve owned by the Ozark Land Trust.

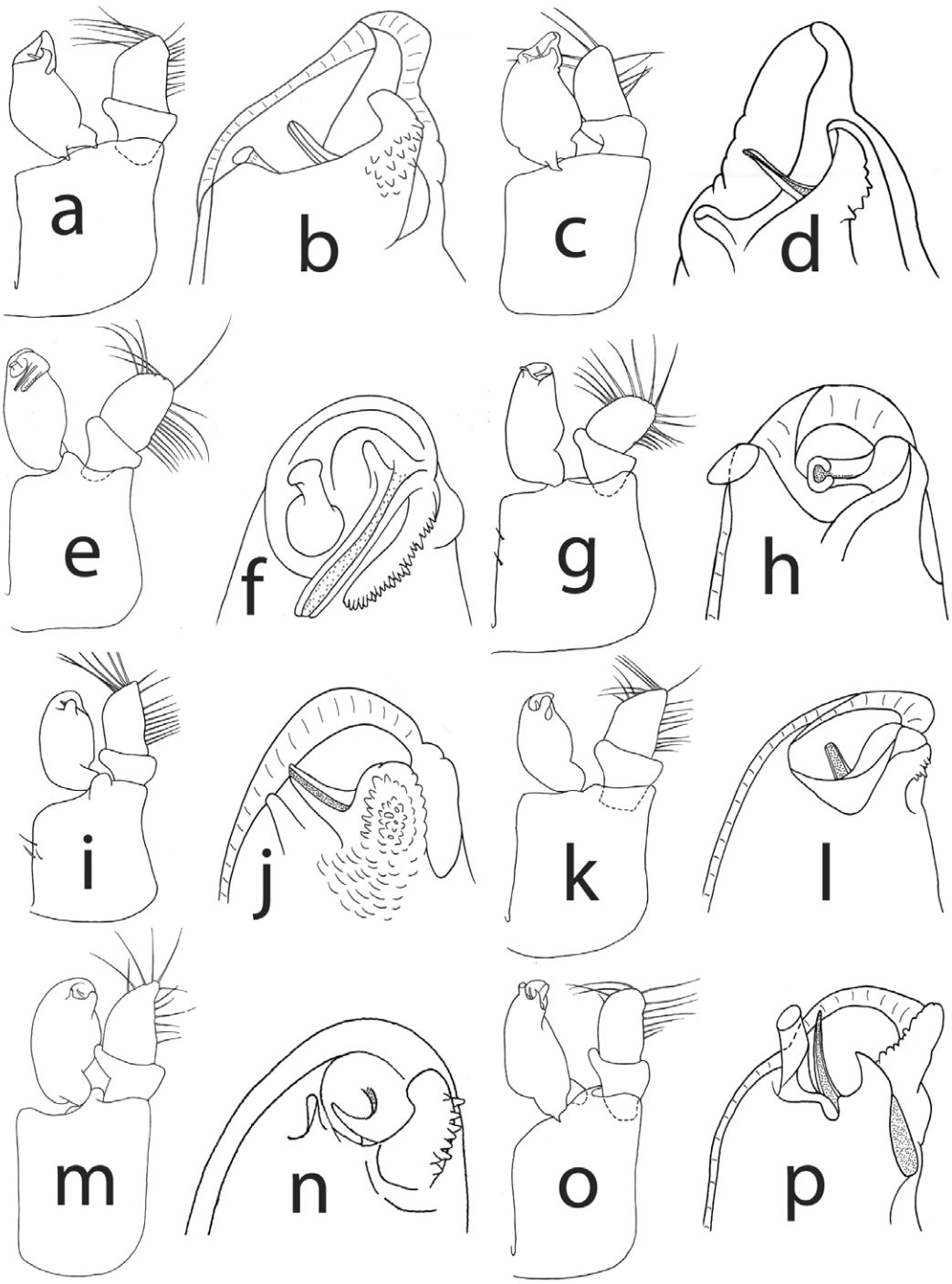

Figure 10. Pleopod 2 and endopodite tip of *Lirceus* species: (a-b) *L. hoppinae,* Day's Cave, Jasper Co., Missouri ; (c-d) *L. ouachitaensis*, tributary of Kiamichi River, Leflore Co., Oklahoma; (e-f) *L. bidentatus*, seep on Osage Creek, Boone County, Arkansas; (g-h) *L. megapodus*, spring 4 mi. NW of Hogan, Iron County, Missouri; (i-j) *L. bicuspidatus*, spring behind college chapel, Clarksville, Johnson County, Arkansas; (k-l) *L. garmani*, temporary stream, Cedar County, Missouri; (m-n) *L. louisianae*, seeps 0.6 mi. S of Junction City, Claiborne Parish, Louisiana; (o-p) *L. trilobus*, spring 3.2 mi. S Locust Grove, Mayes County, Oklahoma.

***Lirceus ouachitaensis* (Mackin and Hubricht, 1938)**

Mancasellus ouachitaensis Mackin and Hubricht, 1938: 632−633.

Lirceus hoppinae ouachitaensis.—Hubricht and Mackin, 1949: 337, 344; Williams, 1972: 14.

Lirceus ouachitaensis.— Graening, et al., 2007: 3, 9−10 [in part]; Graening, et. al, 2011: 159.

Material examined: ARKANSAS: Sevier Co.: Walnut Spring, 1.7 mi. ENE Horatio, off Arkansas State Highway 24, H. W. Robison, 19 Aug 2018, 6♂1♀. OKLAHOMA: Leflore Co.: tributary of Kiamichi River, Ouachita National Forest, J. G. Mackin, 30 Mar 1935, 21♂♀.

Type material: Syntypes 10♂♀ (USNM 108819) and 21♂♀ (USNM 108820) from a tributary of the Kiamichi River, near Big Cedar, LeFlore Co., Oklahoma, deposited in the Smithsonian Institution (Mackin and Hubricht, 1938).

Diagnosis: Distinct from other species of the Ouachitas by the absence of a mandibular palp. The pleopod 2 endopodite is narrow, subtriangular, cannula narrow, mesial process a short knob (Fig. 10c, d). This taxon was considered a subspecies of *Lirceus hoppinae* by Hubricht and Mackin (1949), but is morphologically and genetically distinct.

Habitat and range: Lirceus ouachitaensis occurs in the Ouachita Mountains in western Arkansas and eastern Oklahoma, where it occurs in creeks and springs. Hubricht and Mackin (1949) listed tributary streams in Latimer and Pushmataha counties (Fig. 1).

***Lirceus bidentatus* Hubricht and Mackin, 1949**

Lirceus bidentatus Hubricht and Mackin, 1949: 336, 344−345, 349; Williams, 1972: 14; Robison and Smith, 1982: 53; Robison and Allen, 1995: 47−48; Graening, et al. 2007: 2−3, 8; Robison, et al., 2008: 92; Graening, et al., 2011: 72, 159.

Material examined: ARKANSAS: Boone Co.: seepage area, Osage Creek at bridge, 1 mi. W Compton, M. E. Slay, C. Slay, 7 Mar 2009, 26♂♀; small seeps, 9 mi. SW Harrison, L. Hubricht, 8 Apr 1939, 18♂♀. Newton Co.: Hutchinson Waterfall Cave, 2.2 mi. ESE Compton, M. E. Slay, C. Bitting, C. M. Slay, 29 Dec 2004, 1♂2♀; Tight-N-Twisty Cave, 1.8 mi. ENE Compton, M. E. Slay, C. Brickey, 11 Dec 2004, 1♂.

Type material: Syntypes 18 ♂♀ (USNM 108813) from small seeps 9 mi. SW of Harrison, Boone Co., Arkansas (Hubricht and Mackin, 1949) deposited in the Smithsonian Institution.

Diagnosis: The extremely long, tubular cannula of the male second pleopod endopodite is unique in the genus (Fig. 10e, f), as well as bizarre and unmatched among other North American asellids.

Habitat and range: This species is endemic to a small area of northern Arkansas in the Boston Mountains, with a range of less than 5 kilometers. *Lirceus bidentatus* occurs in seeps, springs, and cave entrances.

***Lirceus megapodus* Hubricht and Mackin, 1949**

Lirceus megapodus Hubricht and Mackin, 1949: 337, 342−343, 348; Williams, 1972: 15.

Material examined: MISSOURI: Iron Co.: small spring 2 mi. N of Belleview, L. Hubricht, 29 Sep 1940, 54♂♀; spring 4 mi. NW of Hogan, L. Hubricht, 18 Jan 1942, 217♂♀; St. Francois Co.: Rock Spring, 1.5 mi. NE Doe Run, J. J. Lewis, S. L. Lewis, 10 Jun 2016, 1♂3♀.

Type material: Syntypes 217♂♀ (USNM 1254685) from a spring 4 mi. NW of Hogan, Iron Co., Missouri (Hubricht and Mackin, 1949) deposited in the Smithsonian Institution.

Diagnosis: Characterized by the enormous pereopod 1 propodus of adult males, which separates *Lirceus megapodus* from other species in the genus, as well as the elongate, laterally projecting tubular cannula of the second pleopod endopodite (Fig. 10g, h). The absence of retinaculae on the protopod of pleopod 1 is unusual, shared with *L. ozarkensis*. The molecular phylogeny of Lewis, et al., (Fig. 8, 2023) suggests that *L. megapodus* differs from other *Lirceus* of the Interior Highlands at the subgenus level.

Habitat and range: This species is endemic to the St. Francois Mountains in southeastern Missouri (Hubricht and Mackin, 1949), where it inhabits seeps and springs emerging from fissures in granitic bedrock (Fig. 1).

***Lirceus bicuspidatus* Hubricht and Mackin, 1949**

Lirceus bicuspidatus Hubricht and Mackin, 1949: 336, 345, 349; Williams, 1972: 14; Robison and Smith, 1982: 53; Robison and Allen, 1995: 47; Graening, et al. 2007: 2−3, 8; Robison, et al., 2008: 87, 92; Graening, et al., 2011: 72, 159.

Lirceus n. sp.—McDaniel and Smith, 1976: 58.

Material examined: ARKANSAS: Franklin Co.: creek at bridge on highway 21, no. 1, M. E. Slay, 26 Feb 2009, 23♂♀; Independence Co.: Foushee Cave Spring Run, M. E. Slay, 11 Mar 2010, 4♂2♀; same locality, M. E. Slay, J. Baxter, 25 Feb 2020, 6♂2♀; Foushee Cave, M. E. Slay, 14 Jun 2011, 15♂♀; same locality, M. E. Slay, J. Baxter, 25 Feb 2020, 3♂8♀; Johnson Co.: Bull Creek Flats Spring, 15 mi. NNW Clarksville, L. D. Leeds, 28 Dec 2020, 19♂♀; small creek W of the College Chapel, Clarksville, L. Hubricht, 28 Apr 1938, 86♂♀; Spadra Branch 1, M. E. Slay, 26 Feb 2009, 38♂♀; spring west of chapel, University of Ozarks, M. E. Slay, 4 Apr 2009, 22♂♀; same locality and collector, 26 Feb 2009, 29♂♀; Newton Co.: Dear Buster Cave, W. Baker, 28 May 2006, 2♂1♀; NW41bb Cave, W. Baker, 4 Mar 2006, 1♂1♀; seep at hillside cabin at Lost Valley Canoe and Cabin, M. E. Slay, C. M. Slay, 11 Nov 2003, 7♂2♀; Spring below collapsed cave, Yardelle, 18 Oct 2017, J. J. Lewis, S. L. Lewis, 5♂♀; Steel Creek Cave, G. O. Graening, D. Fenolio, 12 Dec 2004, 1♂1 juvenile; spring below Whitely School in Buffalo River Valley, M. E. Slay, 11 Nov 2008, 5♂2♀; Searcy Co.: spring on Kelly Creek, M. E. Slay, 25 Feb 2008, 3♂3♀; spring at mouth of Great Hurricane Cave, L. Hubricht, 22 Oct 1939, 42♂♀; West Spring Hollow, M. E. Slay, 25 Feb 2008, 3♂4♀, 1 juvenile; Stone Co.: Barkshed picnic area spring, M. E. Slay, 8 Mar 2010, 11♂3♀, 1 juvenile; Big Spring, M. E. Slay, K. Furr, 9 Mar 2010, 4♂10♀; Blanchard Springs Caverns spring run, M. E. Slay, 23 Aug 2008, 2♂2♀ +fragments; Branscum Spring, M. E. Slay, K. Furr, 9 Mar 2010, 8♂2♀; Mountain View, city park spring, M. E. Slay, 10 Mar 2010, 2♂1♀, 1 juvenile; Mountain View, city park stream, M. E. Slay, 10 Mar 2010, 16♂♀; Tarwater Spring, M. E. Slay, 11 Mar 2010, 1♂1♀; Mountain View, spring in stone amphitheater in city park, J. J. Lewis, S. L. Lewis, 14 May 2022, 17♂♀; unspecified site 2.5 mi. N Mountain View, on Arkansas 9, V. R. McDaniel, 29 Nov 1974, 9 juveniles.

Type material: Syntypes 78♂♀ (USNM 108871) from a small stream west of the college chapel, Clarksville, Johnson Co., Arkansas (Hubricht and Mackin, 1949) deposited in the collection of the Smithsonian Institution. This site is an intermittent spring about 100 meters west of the Munger-Wilson Memorial Chapel on the campus of the University of the Ozarks, located at N35.4775 W93.4689.

Diagnosis: This is the only Ozark *Lirceus* with two bicuspate processes on the palmar margin of pereopod 1 propodus. It is further separated from other Ozark species by the combination of the fused lateral incisions of the head, 3-merous mandibular palp and male pleopod 2 endopodite tip with prominent cannula terminating within the margin of the broadly rounded caudal process (Fig. 10i, j).

Habitat and range: The range of this species is restricted herein to the Boston Mountains of northern Arkansas, about half the area reported by Hubricht and Mackin (1949), who included the Ouachita Mountains (now identified as *L. robisoni*). Preliminary data from sequencing of the mitochondrial 16S gene suggests that this remains a simplification, i.e., *L. bicuspidatus* is a morphospecies comprised of multiple cryptic undescribed species not readily separable by features of the male pleopod endopodite tip. One of these is a troglomorphic population in Foushee Cave, Independence County, Arkansas (Fig. 11).

Lirceus bicuspidatus is an inhabitant of springs, spring-fed streams and caves. At the type-locality, the isopods are common when the water table is sufficiently high for the spring to flow. During dry times of the year the spring disappears, along with the isopods, which presumably retreat into the groundwater.

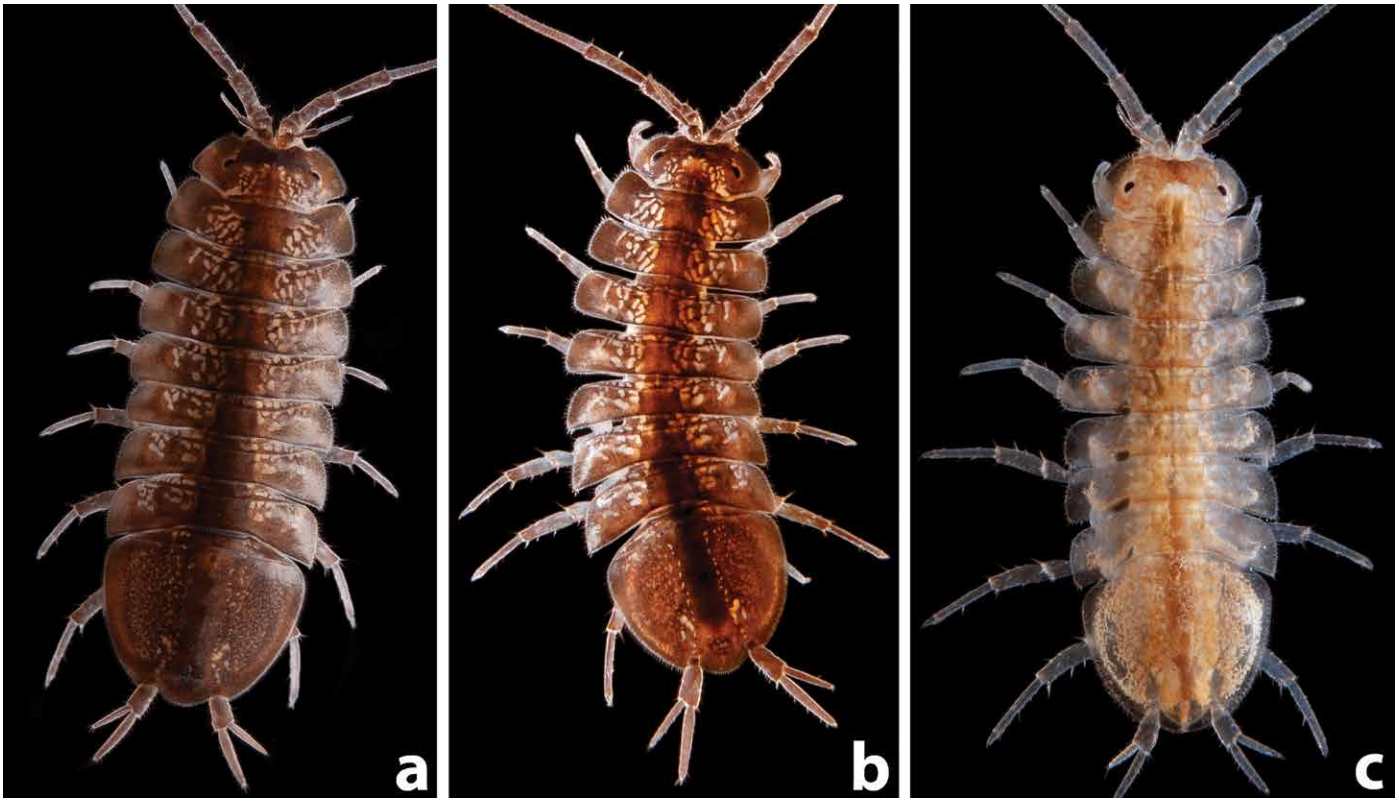

Figure 11. Dorsal pigmentation patterns in Arkansas *Lirceus bicuspidatus* populations: (a) type-locality at Clarksville, Johnson County; (b) Foushee Cave Spring, Independence County; (c) Foushee Cave. (photos by Michael Slay, The Nature Conservancy).

Lirceus garmani Hubricht and Mackin, 1949

Lirceus garmani Hubricht and Mackin, 1949: 337, 345−346; Black, 1971: 7; Williams, 1972: 14. Schultz, 1973: 349−364; Nickol, 1985: 326; Pennak, 1978: 446; Graening, et al., 2007: 3, 8−9; Graening, et al., 2011:159.

Mancasellus macrourus.—Fleming, 1938:310−313; Mackin and Hubricht, 1938: 632 [in part].

Lirceus germani.—Bass, 1994: 7.

Material examined: ARKANSAS: Fulton Co.: sluggish stream in roadside ditch next to Arkansas State Highway 62, 0.6 mi. SSE Flint Spring, J. J. Lewis, S. L. Lewis, 18 Jun 2016, 1♂ 5 juveniles. KANSAS: Bourbon Co.: seep 2.3 mi. S Bronson, L. Hubricht, 17 May 1942, 10♂♀; seep 2.2 mi. E Uniontown, L. Hubricht, 17 May 1942, 16♂♀; Franklin Co.: abandoned well, Wheeler Farm, 5.0 mi. SSE Ottawa, L. Hubricht, 31 Aug 1941, 2♀; spring on Dunkak Farm, 1.5 mi. NW Lane, L. Hubricht, 31 Aug 1941, 44♂♀; Johnson Co.: small temporary stream 1 mi. NE Clare, L. Hubricht, 31 Aug 1941, 14♂♀. MISSOURI: Cedar Co.: temporary stream 3.6 mi. E Cedar Springs, L. Hubricht, 17 May 1942, 42♂♀. OKLAHOMA: Mayes Co.: spring at girl scout camp, 3.2 mi. S Locust Grove, L. Hubricht, 22 May 1940, 15♂♀; Locust Grove spring, J. C. Stout, G. O. Graening, D. Fenolio, 21 Jan 2006, 4♂3♀; spring 3.7 mi. W Locust Grove, L. Hubricht, 31 Aug 1941, 64♂♀; stream in roadside park 0.5 mi. E Locust Grove, upstream of pipe spring, J. J. Lewis, S. L. Lewis, 12 Jun 2016, 12♂♀.

Type material: Syntypes 42♂♀ (USNM 1254682) from a temporary stream 3.6 mi. east of Cedar Springs, Cedar Co., Missouri (Hubricht and Mackin, 1949) deposited in the collection of the Smithsonian Institution.

Diagnosis: Lirceus garmani is separated from other Ozark *Lirceus* by the male second pleopod endopodite that appears two-lobed distolaterally, and the pereopod 1 propodus processes that descend in size distad (Fig. 10k, l).

Habitat and range: This species appears to have a broader range of acceptable habitats than other *Lirceus* occurring in the Interior Highlands. *Lirceus garmani* is primarily known from the Osage Plains region in eastern Kansas, eastern Oklahoma, and western Missouri, with sporadic records in northern Arkansas. The species occurs in springs, seeps, small creeks, and ponds. Black (1971) reported an occurrence in a cave. The Illinois record (Page, 1974) is an error.

***Lirceus louisianae* (Mackin and Hubricht, 1938)**

Mancasellus louisianae Mackin and Hubricht, 1938: 634.

Lirceus louisianae.—Hubricht and Mackin, 1949: 337, 342, 348; Williams, 1972: 15; Graening, et al., 2007: 3, 9; Patrick, 2003: 41; Pennak, 1978: 446.

Material examined: ALABAMA: Greene Co.: roadside ditch 0.8 mi. N Boligee, L. Hubricht, 11 Feb 1962, 13♂♀. ARKANSAS: Fulton Co.: Mammoth Spring, impounded lake below spring, J. J. Lewis, S. L. Lewis, 18 Jun 2016, 19♂♀; Ouachita Co.: Scale Springs, 14.2 mi. NE Camden, H. W. Robison, 23 Jul 2022, 3♂1♀. Phillips Co.: slough 0.5 mi. S Turner, L. Hubricht, 7 Apr 1941, 14♂♀. FLORIDA: Walton Co.: spring 1.5 mi. NE Grayton Beach, under stones, W. Farmer, 27 Dec 2016, 18♂♀. LOUISIANA: Claiborne Parish: seeps 0.6 mi. SE Junction City, L. Hubricht, 8 Apr 1941, 40♂♀; Natchitoches Parish: dead leaves in small creek below an artificial pond, 2 mi. S Saline, L. Hubricht, 19 Apr 1936, 2♂3♀. MISSISSIPPI: Oktibbeha Co.: ditch 6.8 mi. SW junction of state routes 25 and 12, on SR 25, W.G. Anding, 26 Feb 1968, 9♂♀. TEXAS: Nacogdoches Co.: permanent seep area, Nacogdoches, D.C. Rudolph, J.A. Matos, 16 Feb 1980, 3♂1♀.

Type material: Syntypes, 2♂ (USNM 74843), 3♀ (USNM 108807) from a small creek below an artificial pond, 2 mi. S of Saline, Natchitoches Parish, Louisiana (Mackin and Hubricht, 1939), deposited in the Smithsonian Institution.

Diagnosis: This species is separable from other *Lirceus* by a combination of characters: the triangular distal article of the exopod of the second pleopod and coiled appearance of the endopodite tip cannula arising from the papillate lateral process (Fig. 10m, n). In the Interior Highlands, *Lirceus louisianae* is readily separated from *L. bicuspidatus* and *L. ozarkensis* by its lack of a mandibular palp.

Habitat and range: The range of *Lirceus louisianae* is expanded herein from that of Hubricht and Mackin (1949) to encompass the lower Mississippi River drainage, from Louisiana to northern Arkansas, west to Texas and east to the panhandle region of western Florida. Records listed above include the first reports from Texas, Mississippi and Florida. Hubricht and Mackin (1949) included southern Illinois based on specimens from two localities in Union County. These specimens were examined and were not conspecific with *L. louisianae*. The discovery of *L. louisianae* in Mammoth Spring, Arkansas is the first report of this species from the Interior Highlands.

This species occurs in springs, seeps, small creeks, sloughs, and ditches. At Mammoth Spring, Arkansas, we found *L. louisianae* inhabiting gravels about 100 meters downstream from the rise pool.

***Lirceus trilobus* Hubricht and Mackin, 1949**

Lirceus trilobus Hubricht and Mackin, 1949: 336, 346, 349; Williams, 1972: 15; Graening, et al., 2007: 2−3, 10; Graening, et al, 2011: 159.

Material examined: OKLAHOMA: Mayes Co.: spring 3.2 mi. S Locust Grove, L. Hubricht, 22 May 1940, 29♂♀.

Type material: Syntypes 29♂♀ designated as woodland pools at a girl scout camp 3.2 mi. south of Locust Grove, Mayes Co., Oklahoma (Hubricht and Mackin, 1949) deposited in the Smithsonian Institution.

In jars of uncatalogued *Lirceus* from Oklahoma in the collection of the Smithsonian Institution we found two vials labeled “spring 3.2 mi. S of Locust Grove”. Each vial contained a different species. This locality was cited by Hubricht and Mackin (1949) for *L. garmani*. In the second vial, the uncatalogued collection was a distinct species that matches the description for *L. trilobus,* now catalogued as USNM 1254708. No vial with a label matching the wording of the type-locality provided by Hubricht and Mackin (1949) was found among Hubricht’s specimens in the Smithsonian collection. The actual collection site of the type specimens of *Lirceus trilobus* remains a mystery. Perhaps a labelling error occurred and the habitat was indeed a woodland pool, but at this point this question seems unlikely to be resolved. The property on which the type-locality of *L. trilobus* is located, Camp Scott, was closed after the murder of three girl scouts in 1977. We attempted to visit the type-locality, but were unable to gain access.

Diagnosis: The male second pleopod endopodite tip is unlike any other species of *Lirceus* in the Interior Highlands, and it is among the most complex of any species in the genus, with a narrow, elongate cannula extending parallel to the axis of the endopod surrounded by 3 anterior processes and caudal process (Fig. 10o, p)

Habitat and range: Lirceus trilobus is known only from the type-locality, in eastern Oklahoma.

SUMMARY AND CONCLUSIONS

During the course of this investigation, we examined 1825 specimens collected from 43 springs, 7 seeps, 18 caves, 1 well, and 14 small streams (including creeks and ditches). Every species, except *Lirceus louisianae*, occurred predominantly in cool-water habitats (springs, seeps and caves). With the description of 3 new species, there are now 11 species of *Lirceus* recognized from the Interior Highlands. Diversity undoubtedly remains underestimated by this number, e.g., with several populations of the morphospecies *L. bicuspidatus* (including one stygobiontic species) remaining to be described.

Hubricht and Mackin (1949) asserted that the genital pleopods were "so similar in different species that they were, with one exception [*Lirceus bidentatus*], useless as a means of separation". We found similarities in the morphology of the male second (genital) pleopod endopodite tips of the Interior Highlands *Lirceus*, including a lateral process that was digitiform, and usually papillate or dentate, along with a dominant broadly rounded or subtriangular apex. That said, there were many differences in the appearance of the genital pleopods, including great variation in the shape and length of the sperm transfer cannula, as well as the shape and proportions of the exopodites. These morphological differences are consistent with molecular phylogenetic evidence that strongly supported the diversity of the *Lirceus* fauna (Lewis, et al., 2023).

From a conservation standpoint, two species are extremely rare and vulnerable: *Lirceus trilobus*, known only from the type-locality; and *L. bidentatus*, known from a few sites within a range of less than five kilometers. Two spring inhabitants, *L. robisoni* and *L. megapodus*, are recorded from only a few localities confined to small ranges.

ACKNOWLEDGEMENTS

Funding for the preparation of this manuscript is gratefully acknowledged from a Visiting Scientist Grant from the Smithsonian Institution Office of Fellowships and Grants, The Nature Conservancy's Ozark Highlands Karst Program, and the Cave Research Foundation. Work at the Smithsonian Institution was hosted by Dr. Karen Osborn, Curator at the National Museum of Natural History. At the Smithsonian Museum Support Center, our work was coordinated by Museum Specialist Karen Reed, with other assistance graciously provided by Collection Manager William Moser, and Museum Specialists Geoff Keel, Chad Walter, Katie Ahlfeld, and Amanda Robinson. The loan of specimens from the Museum of Comparative Zoology, Harvard University, was facilitated by Adam Baldinger, Collection Manager. Finally, we acknowledge significant support provided for molecular phylogenetic analysis to which we refer herein by Dr. Florian Malard, Prof. Christophe J. Douady, Lara Konecny-Dupré and Nathanaëlle Saclier of the Laboratoire d'Ecologie des Hydrosystèmes Naturels et Anthropisés (LEHNA), Université Lyon 1, Villeurbanne, France. In preparation of the manuscript, Elizabeth Hofmann inked the drawings for finalization of the illustrations. Michael Slay, of The Nature Conservancy, took the excellent photos of living *Lirceus* and provided them for our use. And last but not least, we thank William Orndorff, Karst Program Director of the Virginia Natural Heritage Program, for preparing the range map for *Lirceus* of the Interior Lowlands.

REFERENCES

Arkansas Geological Survey, 1937, http://www.geology.arkansas.gov/docs/pdf/water/springs-in-arkansas.pdf

Bass, D, 1994, Community structure and distribution patterns of aquatic macroinvertebrates in a tall grass prairie stream ecosystem: Proceedings of the Oklahoma Academy of Science, v. 74, p. 3−10.

Black, J. H, 1971, Cave life of Oklahoma: A preliminary study (excluding Chiroptera): Oklahoma Underground, v. 4, nos. 1−2, p. 2−53.

Faxon, W., 1889, Crustacea, in Garman, S., Cave animals from southwestern Missouri: Bulletin of the Museum of Comparative Zoology, v. 17, no. 6, p. 237− 239.

Fleming, R. S., 1938, The larger Crustacea of the Nashville region: Journal of the Tennessee Academy of Science, v. 13, no. 4, p. 296−314.

Graening, G.O., D. B. Fenolio, and M. E. Slay, 2011, Cave Life of Oklahoma and Arkansas: Exploration and conservation of subterranean biodiversity: University of Oklahoma Press, Norman, 226 p.

Graening, G.O., M. E. Slay, D. B. Fenolio, and H. W. Robison, 2007, Annotated checklist of the Isopoda (Subphylum Crustacea: Class Malacostraca) of Arkansas and Oklahoma, with emphasis on subterranean habitats: Proceedings of the Oklahoma Academy of Science, v. 87, p. 1−14.

Hubricht, L., and J. G. Mackin, 1949, The freshwater isopods of the genus *Lirceus* (Asellota: Asellidae): American Midland Naturalist, v. 42, no. 2, p. 334−349. http://dx/doi/org/10.2307/2422012

Hunt, C. B., 1967, Physiography of the United States: W.H. Freeman and Company, San Franciso, 480 p.

Lefébure T., Douady C.J., Gouy M., and J. Gibert, 2006, Relationship between morphological taxonomy and molecular divergence within Crustacea: proposal of a molecular threshold to help species delimitation: Molecular Phylogenetics and Evolution, v. 40, p. 435−447. https://dx/doi.org/10.1016/j.ympev.2006.03.014

Lewis, J. J., 1983, *Caecidotea fonticulus*, the first troglobitic water slater from the Ouachita Mountains (Crustacea: Isopoda: Asellidae): Proceedings of the Biological Society of Washington, v. 96, no. 1, p. 149−153.

Lewis, J. J., S. L. Lewis, W. Orndorff, Z. Orndorff, F. Malard, L. Konecny-Dupré, N. Saclier, and C. Douady, 2023, The groundwater isopods of Virginia (Isopoda: Asellidae and Cirolanidae: Virginia Museum of Natural History, Special Publication 19, 214 p.

Mackin, J. G., 1940, A key to the Oklahoma species of the Family Asellidae: Proceedings of the Oklahoma Academy of Sciences, v. 20, p. 17−18.

Mackin, J. G., and L. Hubricht, 1938, Records of distribution of species of isopods in central and southern United States, with descriptions of four new species of *Mancasellus* and *Asellus* (Asellota, Asellidae): American Midland Naturalist, v. 19, p. 628−637. https://dx/doi.org/10.2307/2420477

McAllister, C. T., 2020, Abernathy Spring. Encyclopedia of Arkansas, https://encyclopediaofarkansas.net/entries/abernathy-spring-geological-feature-10612/

McDaniel, V. R., and K. L. Smith, 1976, Cave fauna of Arkansas: selected invertebrate taxa: Proceedings of the Arkansas Academy of Science, v. 30, p. 57−60.

Nickol, B. B., 1985, Epizootiology, in Crompton, D. W. T and B. B. Nickol, eds., Biology of the Acanthocephala: Cambridge University Press, p. 307−346.

Patrick, R., 2003, Rivers of the United States: Gulf of Mexico: John Wiley and Sons, v. 5, Part B, 272 p.

Pennak, R. W., 1978, Fresh-water invertebrates of the United States, second edition: John Wiley and Sons, New York, 803 p.

Racovitza, E. G., 1920, Notes sur les Isopodes: Archives de Zoologie Expérimentale et Générale, v. 59, v. 2, p. 28−66.

Rafinesque, C. S., 1820, Annual synopsis of new genera and species of animals, plants, etc. discovered in America: Annals of Nature, v. 1, p. 1−16. https://dx/doi.org/10.5962/bhl.title.106763

Robison, H. W., and K. L. Smith, 1982, The endemic flora and fauna of Arkansas: Arkansas Academy of Science Proceedings, v. 36, p. 52−57.

Robison, H. W., C. McAllister, C. Carlton, and G. Tucker, 2008, The Arkansas endemic fauna: An update with additions and deletions: Journal of the Arkansas Academy of Science, v. 62, p. 84−96.

Robison, H. W., and R. T. Allen, 1995, Only in Arkansas: A study of the endemic plants and animals of the state: University of Arkansas Press, Fayetteville, 121 p.

Schultz, T. W., 1973, Functional morphology of the oral appendages and foregut of *Lirceus garmani* (Crustacea: Isopoda): Transactions of the American Microscopical Society, v. 92, p. 349−3644. http://dx/doi.org/10.2307/3225239

Van Name, W. G., 1936, The American land and fresh-water isopod Crustacea: Bulletin of the American Museum of Natural History, v. 71, p. 1−535.

Wagner, G. H., and K. F. Steele, 1980, Chemistry of the spring waters of the Ouachita Mountains excluding Hot Springs, Arkansas: Arkansas Water Resources Research Center, University of Arkansas, Fayetteville, Publication 69, 57 p. + appendices.

Williams, W. D., 1970, A revision of North American epigean species of *Asellus*: Smithsonian Contributions to Zoology, v. 49, p. 1−79. http://dx/doi.org/10.5479/si.00810282.49

Williams, W. D., 1972, Freshwater Isopods (Asellidae) of North America: Biota of Freshwater Ecosystems, Identification Manual 7, U.S. Environmental Protection Agency, 45 p. https://dx/doi.org/10.5962/bhl.title.4017

Douglas M. Medville. Rock Pigeon Cave, Colorado: development and mineralogy. *Journal of Cave and Karst Studies*, v. 85, nos. 3/4, p. 102-115.
DOI:10.4311/2023ES0104

ROCK PIGEON CAVE, COLORADO: DEVELOPMENT AND MINERALOGY

Douglas M. Medville[1]

Abstract

The late Cretaceous Mancos Shale in western Colorado contains several vadose caves developed entirely within the shale. The largest of these, Rock Pigeon Cave, is over 300 m in length and contains a seasonal stream. The cave, and others like it, is hypothesized to develop as a result of the oxidation of disseminated pyrite in the shale by descending meteoric water with resulting sulfate ions reacting with the carbonate component of the shale to produce gypsum. The gypsum pries apart the shale, increasing its secondary porosity, and allows flowing water to remove shale particles via corrasion. As these particles are removed, they are transported down-gradient to an outlet, allowing continuous openings (cave passages) to develop. Extensive sulfate mineralization is observed within the cave and takes several forms: soft globular deposits on rocks at water level, a white to tan crust on shale surfaces, dry crusts on the passage floor following evaporation of pools, and needle and hair-like extrusions on passage walls. Powder X-ray diffraction (XRD) indicates that these deposits are a mixture of thenardite and blodite with lesser amounts of gypsum, hexahydrite, and konyaite.

Na^{+}, Mg^{2+}, and SO_4^{2-} ions in the entering stream are the source of the sulfate minerals at stream level and on the wetted slopes above. These come out of solution as the cave stream and pools evaporate with sulfates precipitating as saturation is reached. Fibrous, needle-like sulfates on walls above the wetted zone are a result of crystallization by evaporation: fluids containing sulfate ions are extruded and evaporate at the rock/air interface. Other minerals, e.g., deposits containing goethite and jarosite, are seen on passage walls as reaction products from oxidation of pyrite in the shale.

INTRODUCTION

Cave passages in fissile shales are usually found in settings where stream erosion in solutional caves incises into shale beds within or below limestones or where surface streams remove shale particles, resulting in shelter caves (Palmer, A., 2007). Vadose caves found entirely within shales and containing active stream or streambeds, while rare, have been reported for an area in north-central Wyoming (Medville, D., 2018) and are also found in western Colorado (this paper).

The occurrence of caves in shales is infrequent due to the conditions to be met for cave development to take place:

- Soils above the shale should contain swelling clays that allow dolines to develop, enhancing the movement of meteoric water to the unweathered shale below.
- Pyrite in the shale is required for reaction with surface and ground water, producing sulfate ions in sufficient quantity to react with calcite in the shale, producing gypsum that, in turn, fractures the shale, increasing its porosity and producing openings that water can flow through.
- A gradient is needed for water to move through openings in the shale to an outlet, allowing shale particles to be removed.
- An arid climate where evaporation exceeds precipitation is needed. If the climate is too wet, although pyrite will oxidize and produce sulfate ions, water moving through the shale may keep ionic concentrations too low for gypsum to precipitate and mechanically wedge the shale apart. This will prevent the development of small voids that can subsequently be enlarged via corrasional processes.

These conditions are met in the study area discussed in this paper: an exposure of soil mantled Mancos Shale in western Colorado. The area lies within the U.S. Bureau of Land Management's Gunnison Gorge National Conservation Area and contains sparse vegetation, deeply incised arroyos, and numerous karst-like features including dolines, blind valleys, and cave entrances. Mean annual precipitation is 30 cm (rain equivalent), and mean annual evaporation is 51 cm (U.S. Department of Agriculture, 2018). Mean annual temperature is 10.5 °C.

METHODS

Bulk mineral analysis of cave wall material was conducted using a Pananalytical X'Pert Pro XRD diffractometor for powder XRD analysis. Continuous scans over a 40-minute period were carried out between 6° and 69° 2θ positions with a step size of 0.017°. Counting peaks provided a semi-quantitative measure of the quantities of mineral components in the samples with peak intensities used to determine the relative proportions of minerals.

Scanning electron microscopy was conducted using a TESCAN-VEGA-3 Integrated Mineral Analyzer (TIMA) coupled with four PulseTor silicon drift EDX detectors for elemental analysis of shale and sulfate minerals at 50 µm-100 µm scales. X-ray counting peaks were consistent with those seen in XRD diffractograms for minerals of interest: primarily

[1] 10701 Pinewalk Way, Highlands Ranch CO 80130, medville@centurylink.net

gypsum, thenardite, and blodite. Stable sulfur isotope measurements were conducted at the University of Waterloo Environmental Isotope Laboratory using a Costech Instruments Elemental Analyzer (CHNS-O ECS 4010) coupled to an Isochrom Continuous Flow Stable Isotope Ratio Mass spectrom. $\delta^{34}S$ results with respect to the Canyon Diablo Troilite meteorite standard were reported in per mil (‰) units. Temperature and humidity readings in the caves were measured using a Protmex model 6508 digital temperature humidity m accurate to 0.1 °C and 0.1 % RH. A Hanna Instruments model HI98100 m was used to measure cave and surface water pH.

Water samples were collected in pre-washed 250 ml polyethylene bottles that were filled underwater until no air remained. The bottles were placed in containers cooled to 10 °C (cave water temperature) until they were mailed to testing laboratories, usually between 24 and 48 hours after collection. For the samples collected, National Environmental Methods Index Standard Methods (SM) were followed: SM4500 H B for pH; SM 2320 for carbonate, bicarbonate, and alkalinity (as $CaCO_3$); SM 3120 for Ca, Mg, K, S, Cl, and Fe; and SM 4500 Cl E for Chloride. EPA 353.2 was used for nitrate. These parameters were used as inputs to PHREEQC (Parkhurst, D.L. and C.A. J. Appelo, 1999); the USGS hydrogeochemical modeling software for calculating ion activities and saturation indexes with respect to the various minerals in the water samples taken. Soil compositional analysis was carried out at the Colorado State University Soil, Water, and Plant Testing Laboratory using Inductively Coupled Plasma Optical Emission Spectrometry (Perkin-Elmer Optima 7300V). Methods used to calculate soil pH, alkalinity, sulfates, cations, and Sodium Adsorption Ratio are described in Miller, R.O. et. al., 2013.

RESULTS AND DISCUSSION

Geologic Setting

The late Cretaceous Mancos Shale outcrops over a 1600 km^2 area between Grand Junction and Montrose, Colorado. The regional outcrop of the Mancos and the study area are shown in Figure 1. The study area is in the upper part of a tributary to Loutsenhizer Arroyo, itself a tributary to the Uncomphagre River, 10 km to the northwest. The area is 0.6 km northeast of the axis of the northward plunging Montrose Syncline. Local dip is about 2 degrees to the southwest.

The Mancos Shale reaches a maximum thickness of nearly 600 m (Hansen, W. R., 1971) and generally consists of calcareous silts with minor limestone, marlstone, bentonite, concretions, and sandstone beds. These rocks represent muddy shelf deposits, and typically

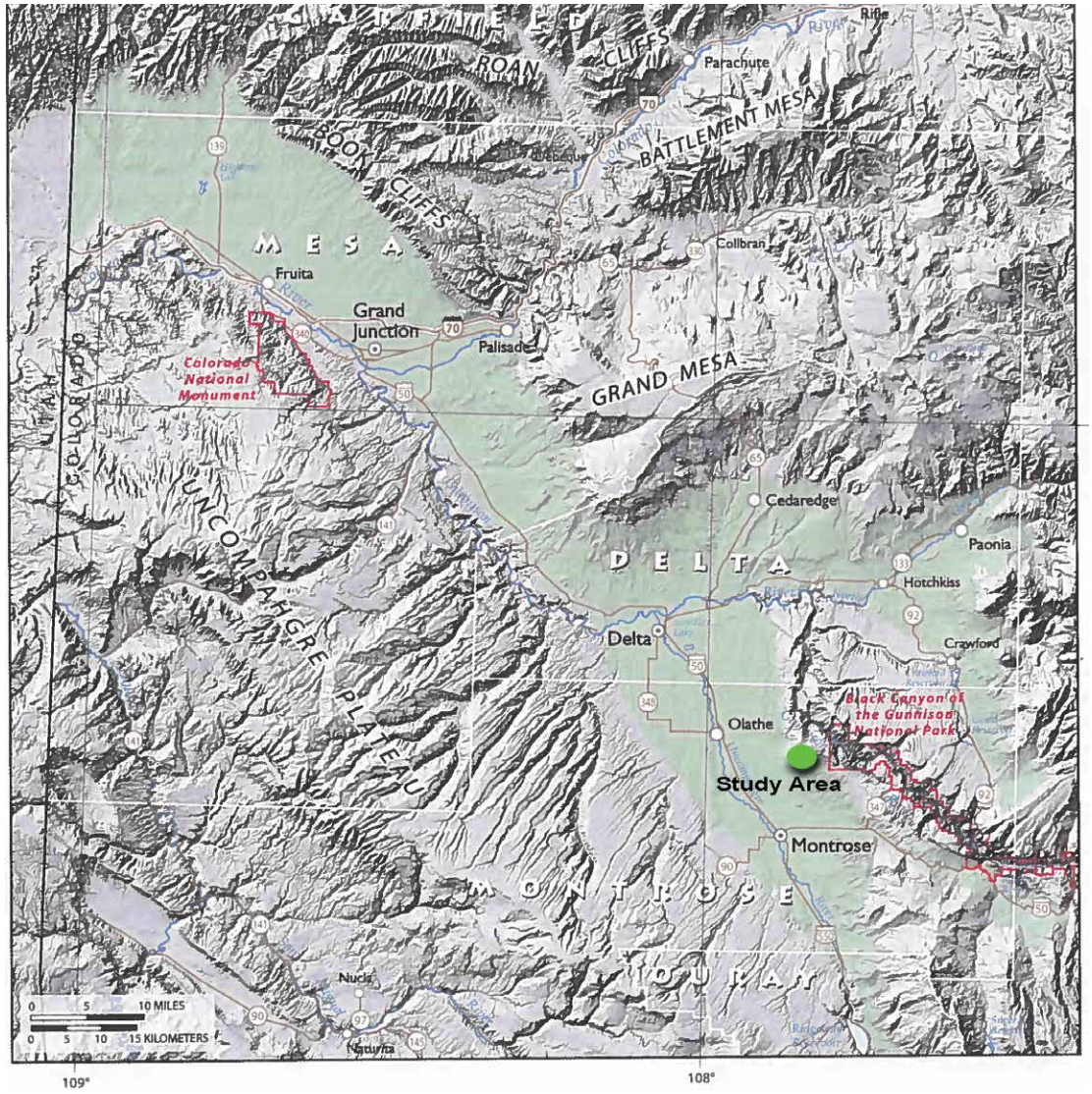

Figure 1. Study area location, Mancos Shale outcrop shown in green. (Source: White, J.L. and C. Greenman, 2008)

form badland-style topography. The local topography is developed on the Niobrara member of the Mancos: a dark gray calcareous shale with a thickness of 230 m to 250 m. The upper Mancos weathers to a pale yellowish-orange or brown color, defined as those portions of Mancos that have undergone significant changes related to weathering processes, chiefly pyrite oxidation to iron hydroxide minerals (Kellogg, K. et. al., 2004; Noe et. al., 2007; U.S. Department of Energy, 2011; White, J.L. et.al., 2014; Noe, D.C., et. al., 2015).

Mancos soils in the study area consist of Wisconsonian age terrace and pediment deposits, primarily a sandy silt. The soils contain soluble Ca^{2+}, Mg^{2+}, Na^{+}, and K^{+}, as well as gypsum and hydrated Na and Mg sulfates (Whittig, et. al., 1982, Evangelou, et. al., 1984).

The average composition by volume of Mancos soils is 35% clay, 55% silt and 10% sand (Tuttle, M.L., et. al., 2014). The soils mantle the shale beneath and consist of barren or nearly barren outcroppings of gypsiferous and saline shale and some soil material (U.S. Department of Agriculture, 1967). Clays in the Mancos soils are a combination of illite, kaolinite, and up to 15cm thick lenses of montmorillonite, a smectite-group sodium phyllosilicate clay that swells when wetted and desiccates when dried.

The montmorillonite component of the Mancos soils results in a pebbly, adobe-like appearance with shallow desiccation cracks and 2-3 m deep soil dolines in gullies, overlying and aligned with cave passages below (Fig. 2). The soil dolines allow meteoric water to penetrate the regolith, ultimately reaching the unweathered shale below where pyrite oxidation can take place.

Two to three m beneath the local regolith, the weathered Mancos transitions to a darker gray to black unweathered shale where the larger Mancos caves are found. The mean unweathered shale composition based on XRD of nine wall samples taken in six caves in the Mancos is 33 % quartz, 29 % muscovite, and 18 % calcite. The remaining 20 % consists of dolomite, gypsum, and several clays.

Cave Development

The Mancos Shale was deposited in a deep water, anoxic environment and contains significant quantities of disseminated framboidal pyrite. Pyrite oxidation in the weathered zone of the shale creates sulfuric acid that reacts with available calcite in the shale to form gypsum. The gypsum crystallizes along bedding planes in the shale, wedging and

Figure 2. Aligned dolines on Mancos soils.

prying it apart (White, J.L. and C. Greenman, 2008). Also, microfracturing in the shale allows an increase in oxygen influx, accelerating the chemical weathering of both pyrite and carbonate in the shale and increasing its secondary porosity (Gu, X. et.al., 2020). Subsequent dissolution of the gypsum and disaggregation of shale particles via granular removal by meteoric water (i.e., corrasion) result in the development of small subsurface voids. As surface water flows through voids in the fractured shale, micron-scale transportable particles are moved down-gradient to outlets that allow the water to emerge on the surface, carrying with it clay particles from the decomposed shale. Over time, initial voids coalesce and enlarge, allowing humanly enterable passages to develop. Headward erosion (i.e., sapping of the shale) at the down-gradient end of the initial conduit can also result in passage enlargement.

Although the processes differ, the resulting voids can have the same general morphology as caves found in carbonate rock: sinuous, vadose canyon-like passages that under-drain small valleys and contain seasonally flowing water. This process has been observed in the Cretaceous Cody Shale in the Bighorn Basin in north-central Wyoming (Medville, D., 2018) and in the Mancos Shale in western Colorado as described in this paper.

The upper Mancos contains about 1% pyrite (U. S. Department of Energy, 2011). Sulfate ions resulting from pyrite oxidation react with calcium derived from carbonates in the shale to produce gypsum under evaporative conditions. A common reaction is:

1. $CaCO_3 + H^+ + SO_4^{2-} + 2H_2O \leftrightarrow CaSO_4 \cdot 2H_2O + HCO_3^-$

The source of the H^+ can be mildly acidic meteoric water (H_2CO_3), which disassociates to H^+ and HCO_3^- ions. The H^+ reacts with the CO_3^{2-} in the calcite to yield Ca^{2+} and bicarbonate ions:

2. $H^+ + CaCO_3 \rightarrow HCO_3^- + Ca^{2+}$

Figure 3. Orange Goethite-containing deposit on passage wall.

The Ca^{2+} reacts with SO_4^{2-} to produce gypsum per reaction (1). Discussions of pyrite oxidation, expansion of pyritic shales, and formation of gypsum are discussed in several reports and papers, e.g., Palmer, A., 2007, Penner, E. et. al., 1972, Nordstrom, D. K., 1982.

With twice the molar volume of calcite[2], gypsum is precipitated on shale surfaces in both starburst and fibrous forms. Reaction-induced swelling resulting from gypsum emplacement can lead to microfracturing of the shale, increasing its secondary porosity and enabling surface water to move through it and remove particles via corrasion (Gu et. al., 2020). Dissolution of gypsum interbeds on cave passage walls will also increase secondary porosity, further increasing the occurrence of open spaces between shale beds.

Pyrite in the shale is oxidized by a combination of meteoric water and atmospheric oxygen. Iron in the pyrite precipitates as goethite, an oxyhydroxide seen on cave passage walls and illustrated in Figure 3.

3. $4FeS_2 + 15O_2 + 10H_2O \rightarrow 4FeO(OH) + 8H_2SO_4$

Reaction (3) is a summary of several intermediate reactions involving microbially catalyzed oxidation of ferric sulfides to ferrous and then ferric sulfates, then ferric hydroxide and then dehydration to FeO(OH). Details are provided in (Penner, E., et. al., 1972; Nordstrom, D.K., 1982, Medville, D., 2018).

Iron can also precipitate as ferric sulfate as per reaction (4).

4. $4FeS_2 + 15O_2 + 2H_2O \rightarrow 2Fe_2(SO_4)_3 + 2H_2SO_4$

If potassium is available from the illite clay component in the shale, ferric sulfate can convert to jarosite as per reaction (5).

[2] Volume change from calcite to gypsum is 2.01. Molar mass gypsum/density gypsum = 172.17 g/mol / 2.32 g/cc = 74.21 cc/mol gypsum. Molar mass calcite/density calcite = 100.09 g/mol / 2.71 g/cc = 36.92 cc/mol calcite. 74.21/36.92 = 2.01.

5. $3Fe_2(SO_4)_3 + 12H_2O \rightarrow 2KFe_3(SO_4)_2(OH)_6 + 5H_2SO_4$

In the cave studied (Rock Pigeon Cave), samples were taken of gypsum crystals on shale near the upper entrance. These samples had $\delta^{34}S$ values of −22.03 ‰ and −19.19 ‰, respectively; consistent with the results of a previous study (Tuttle, M.L. et. al., 2014) where the average $\delta^{34}S$ values from microscopic pyrite in the Mancos Shale was −20 ‰. That study concluded that the source of gypsum formation during incipient weathering of the Mancos Shale was from calcite dissolution as a result of acid produced during pyrite oxidation.

The light $\delta^{34}S$ values are taken as evidence for microbial sulfur isotope fractionation of Cretaceous sulfates when they were reduced to sulfides (FeS_2), which, when oxidized following lowering of the water table, produced sulfate ions that are also light in ^{34}S, as seen in the gypsum samples taken in this study and in the pyrite samples taken in an earlier study (Medville, D., 2018).

Although the Mancos Shale is calcareous, its calcite component does not contribute to cave development as a result of dissolution. The mean calcite content for shale samples taken from the walls of five Mancos caves was 17 %, consistent with a previous study (U.S. Department of Energy, 2011) where a 20 % mean calcite content for Mancos samples was obtained.

While dissolution of the carbonate component of the shale contributes indirectly to passage enlargement via conversion to gypsum, it is not the primary factor in cave development. If, as is the case with the Mancos Shale, the rock is mainly insoluble, dissolution is limited to removing soluble grains from a continuous matrix of insoluble material and is slowed if the insoluble content is more than about 20-30% (Palmer, A., 2007).

The insoluble content of the upper members of the Mancos is about 80 %, consisting of clays, quartz, and muscovite. With contact between aggressive water and calcite grains inhibited by the presence of insoluble material, dissolution is limited. To date, there is no observational evidence of carbonate dissolution in the caves, e.g., rounded, smooth rock surfaces, solution scallops on passage walls, secondary deposition of calcite.

Rock Pigeon Cave

Of the 12 known caves in the Mancos that reach shale bedrock, Rock Pigeon Cave, with 322 m in length and passage up to 15 m in height, is the largest known to date. A map of the cave showing locations where samples were taken for XRD is shown in Figure 4. XRD results are given in Table 1.

The cave is in the Niobrara member of the Mancos, described as a dark-gray to light-gray, calcareous to very calcareous, fissile to sub-platy shale with freshly exposed bedding planes speckled with small white forams and coccoliths (Noe, D.C., et. al., 2015). When viewed under SEM, shale samples taken at the cave's upper entrance show both framboidal pyrite and coccoliths, consistent with the description of this member.

The cave's upper entrance (Fig. 5) is developed at the distal end of a 15 m-deep gully; an infeeder to the 30 m-deep northern branch of Loutsenhizer Arroyo. The unnamed gully in which the cave is found drains an area of 1.8 square km. The entrance is a 7 m-high canyon-like opening 10 m below the local surface.

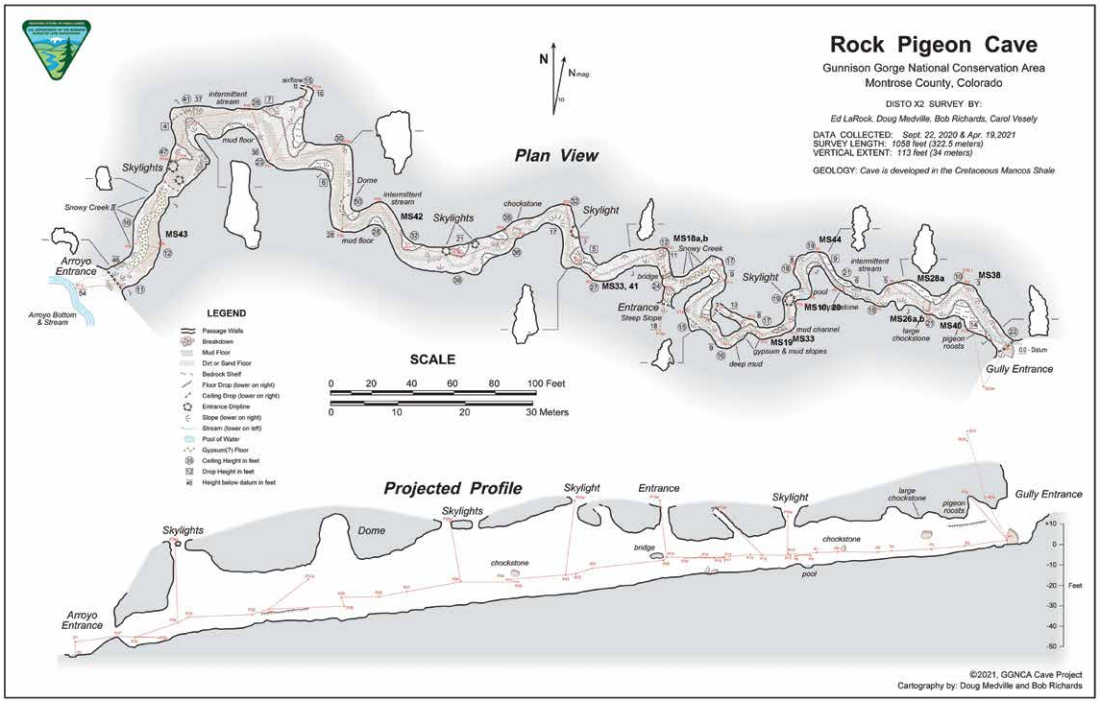

Figure 4. Map of Rock Pigeon Cave with XRD sampling locations.

The cave consists of a single passage that meanders beneath the gully above. Joint-controlled passage orientation is not evident in the cave. The passage has a uniform gradient of 2.6°, the same as that of the 0.67 km long arroyo that carries the stream that flows through the cave

Figure 5. Upper Rock Pigeon Cave entrance with abandoned drainage above.

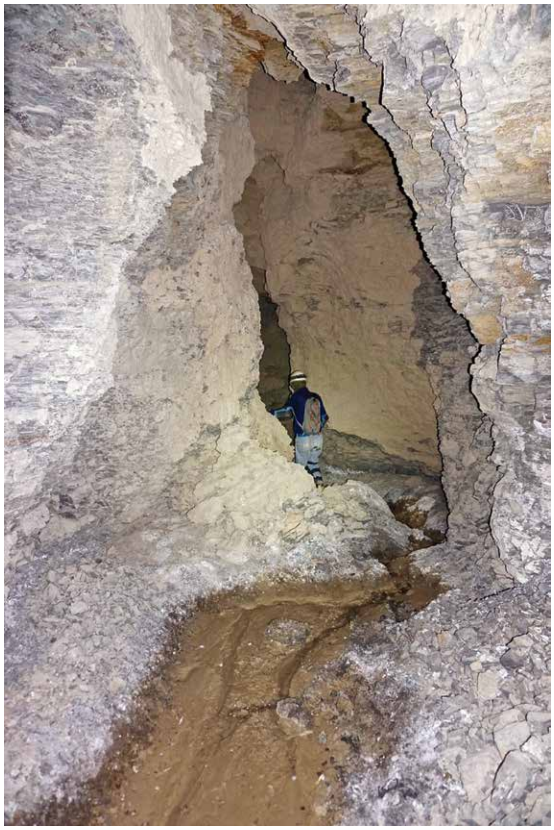

Figure 6. Representative passages in Rock Pigeon Cave.

(measured discharge = 0.03 cms). The stream flows for most of the year; drying up between mid-August and mid-October.

The source of the stream is primarily small seeps along the gully with a minor contribution from meteoric water. The cave stream emerges at the cave's lower entrance in a branch of Loutsenhizer Arroyo.

Throughout the cave, the average passage height is 7 m and where seen, consists of a flat horizontal surface in the shale with no apparent change in lithology. The passage floor consists of shale-derived particles forming mud flats containing a shallow braided stream channel. Slopes of damp and disaggregating shale along and below vertical passage walls are seen through much of the cave. A Photograph of representative cave passage is shown in Figure 6.

The cave has the appearance of a beheaded remnant of a formerly longer cave that would have originated some distance up-gully from the current upper entrance, perhaps at an elevation accordant with the elevation of the current paleo-gully floor above the cave. At present, cave evolution and physical enlargement appear to be actively continuing with wall and ceiling spalling taking place.

With an absence of organic material and speleothems in the cave that can be dated, quantitative methods; e.g. $^{230}Th/^{234}U$ decay and carbon-14 dating, are not applicable. A minimum age, however, can be estimated using passage dimensions and local/regional stream and river incision rates. In a series of rainfall-runoff simulations carried out by USGS (Elliott, J.G. et. al., 2007), an incision rate of 0.5 mm/year for gully slopes in excess of 20° was estimated. The simulations were carried out in several small plots 3.4 km SE of the cave in gullies similar to the one containing Rock Pigeon Cave. This incision rate is equivalent to a mass loss of 700 g m^{-2} a^{-1} (Tuttle, M. L. et. al., 2014). The cave's lower entrance, at grade with the branch of Loutsenhizer Arroyo into which it drains, is 3.3 m high. If the initial discharge into the arroyo floor was at current ceiling elevation, an age estimate of 3300 mm/ 0.5 mm per year = 6,600 years is obtained. This is a minimum estimate that places the cave's origin in a periglacial, post-Pleistocene environment.

Water Chemistry

Two water samples were taken in April 2021: one from the gully stream entering the cave 100 m above the cave's upper entrance and another inside the cave, 200 m below the upper entrance. As expected, water chemistry for both samples were similar: pH was 8.1 and 8.3, conductivity was 18400 and 18970 μmhos cm^{-1}, and total dissolved solids were 12270 and 12430 mg L^{-1}, respectively.

Both samples were high in sulfates (6600-7350 mg L^{-1}) and sodium (3900- 4400 mg L^{-1}) with lesser concentrations of Mg (336-426 mg L^{-1}) and calcium (169-205 mg L^{-1}). These and other parameters were entered into PHREEQC. Modeling results indicated that the cave pool water was slightly supersaturated with respect to calcite (SI = +0.49) where SI is the log Saturation Index = log ion activity product - log solubility product. The water was undersaturated with respect to gypsum (SI = -0.3) and halite (SI=-4.86). Surface water results were similar: for $CaCO_3$, the SI was +1.86, for gypsum, it was -0.5, and for halite, it was-5.06. Neither thenardite nor blodite SIs were reported for the samples. This was not unexpected: a stream was flowing through the cave, pools were not evaporating, and sulfate evaporites were not being deposited. Since subaqueous deposits were observed under unusually dry conditions when only isolated pools were present, the extent to which the concentration of various species increase as a function of pool evaporation remains to be determined.

Estimates of the relationship between degree of evaporation and ion concentration have been obtained in previous studies. In a study carried out by the USGS in Elephant Skin Wash, 4 km east of the cave, the evaporation of surface water was simulated using PHREEQC (Tuttle, M. L. et. al., 2014). In the simulated evaporation of one liter of solution from a surface pond, blodite did not precipitate (1.5 grams) until 99.98 % of the solution evaporated and mirabilite only precipitated (also 1.5 grams) when 99.3 % of the solution evaporated.

SI as a function of evaporation was also simulated in a study of the evaporation of brines in shallow playas in Spain (Cabestero, O., et. al., 2018). In that study, PHREEQC was used to simulate the increase in brine concentration as evaporation increased. SIs for blodite and thenardite were negative until 84 % of the brine was evaporated. In actual samples taken in the playa, SIs remained negative even as blodite, thenardite, and other species were observed to precipitate.

In Rock Pigeon Cave, PHREEQC was used to simulate the evaporation of pool water. Results were consistent with those of the previous studies in that all species remained in solution even as the simulated pool water evaporation approached 100 % (Fig. 7).

Precipitation of Sulfate Minerals

Mancos soils contain 0.3 % wt gypsum-equivalent salts, of which 0.2 % wt are extractable; primarily calcite, gypsum, Na_2SO_4, and NaCl (Tuttle, M.L. et. al., 2014). Weathering of the soil (pedogenesis) is marked by a significant decrease in bulk density and an increase in porosity as the shale disaggregates. The porosity increase enables water to move through the soil and redistribute dissolved sulfate ions derived from in situ weathering (Merkler, D., et. al., 2006).

On average, 90 % of precipitation in the immediate area infiltrates the soil, carrying with it salts dissolved at the surface (Elliott, J.G., et. al., 2007). As evaporation takes place, efflorescent sulfate crusts form on the surface of the soil. These may consist of sulfate evaporite species including gypsum ($CaSO_4{\cdot}2H_20$), thenardite (Na_2SO_4), mirabilite ($Na_2SO_4{\cdot}10H_2O$), glauberite $Na_2Ca\ (SO_4)_2$, and blodite ($Na_2Mg\ (SO_4)_2{\cdot}4H_2O$). Soluble salt cations, e.g., Ca^{2+}, Na^{+}, Mg^{2+}, K^{+}, and anions, e.g., SO_4^{2-} diffuse into solution and are carried into the cave by the entering stream. As a result of evaporation, these solutions can become supersaturated with respect to one or more ions with resulting sulfate precipitation (Onac, B. and P. Forti, 2011).

In Tausoare Cave in Romania, crystallogenesis of sulfate minerals is hypothesized to occur as a result of flooding events where sulfate-enriched water in the cave stream imbue the sediments with the sulfate anion (Onac, B.P., et. al., 2001). This process also applies to Rock Pigeon Cave where, as the stream and pools evaporate, ionic concentrations increase until sulfates are deposited on surfaces including the water/rock interface at pool level, at the high water line through most of the cave, on the passage floor as crusts, and possibly subaqueously.

In Rock Pigeon Cave, both calcium and sodium minerals are observed. Gypsum occurs as 5-10 mm wide starburst crystals on dry rock surfaces and as fibrous fillings between shale beds. Sodium sulfates detected via powder XRD include (a) thenardite, the dehydration product of mirabilite, (b) the hydrated sodium-magnesium salt blodite, (c) hexahydrite ($MgSO_4{\cdot}6H_2O$), and (d) the uncommon hydrated double salt konyaite ($Na_2Mg\ (SO_4){\cdot}5H_2O$), found in evaporated cave water. These sulfates are evident throughout the length of the cave. They are both exogenous, i.e., derived from water entering the cave and endogenous, i.e., from in situ pyrite oxidation taking place within the shale walls of the cave. The sulfates take several forms:

A. Globular precipitates

Soft globular clusters 7-12 mm in diameter are seen at the margins of the cave stream and in evaporating pools. The sulfates are the result of increased ionic concentration as pools evaporate with subsequent crystallization of the observed

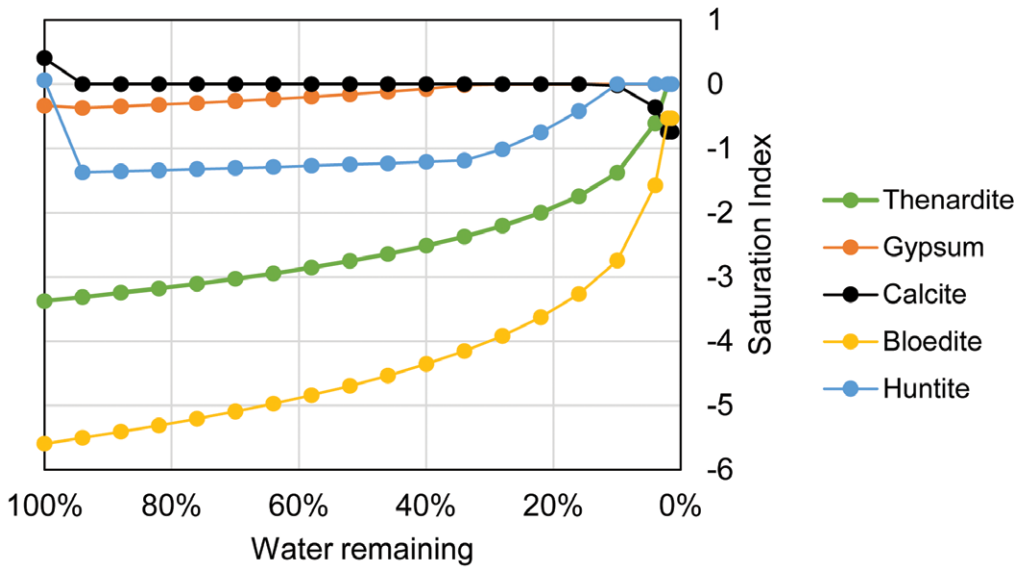

Figure 7: Simulation of evaporating cave water using PHREEQ.

minerals. They present as white to yellow/tan precipitates without a nucleation core and are typically roughly rounded cruciform shaped assemblages up to three cm in diam (Figs. 8 and 9).

When placed in distilled water, the clusters dissolve within 15-20 minutes with no insoluble residue remaining, i.e., there does not appear to be any nucleation around a central insoluble core. These evaporites are only found at and immediately above the cave stream and pools. Similar sulfate speleothems have been found to appear seasonally in Tausoare Cave in Romania as environmental conditions in that cave seasonally changed (Onac et. al., 2001) as is observed in Rock Pigeon Cave.

Five samples of the sulfate deposits found at water level were taken at 50 m intervals through the cave. The principal constituents of the crust are thenardite (μ = 54.2 %) and blodite (μ = 38.0 %). Three of the samples contained

Figure 8. Globular thenardite/blodite precipitates, 2-3 cm diam.

Figure 9. Globular precipitates at cave stream water level.

Table 1. Rock Pigeon Cave XRD results.

Sample	Description	Percentage													
		muscovite	quartz	kaolinite	calcite	dolomite	gypsum	jarosite	goethite	illite	thenardite	blodite	halite	hexahydrite	konyaite
MS10	Red wall material	...	26	13	...	...	49	8	4	...	...	...	...	...	...
MS18a	Damp shale on floor	21	49	8	11	11	...	...	...	...	...	...	...	...	...
MS18b	Sulfate globules	...	...	...	...	...	...	...	...	...	53	47	...	...	...
MS19	Red wall material	...	...	49	31	...	...	13	...	...	7	...	...	...	...
MS20	Red wall material	35	28	28	5	...	...	...	4	...	...	...	...	...	...
MS23	Dry shale	30	43	8	4	9	6	...	...	...	...	...	...	...	...
MS26a	Dry shale above sulfates	...	42	34	5	7	...	...	...	12	...	...	...	...	...
MS26b	Damp shale below sulfates	...	46	12	2	9	...	...	...	31	...	...	...	...	...
MS28a	Wall sulfate at high water line	...	28	10	2	4	8	...	...	10	29	9	...	...	...
MS33	Wall needles, filaments	...	9	11	1	4	16	...	...	23	20	16	...	...	...
MS37	Twig coatings above cave	...	...	...	...	...	...	...	...	5	18	75	2	...	...
MS38	Crystals on dry shale at entrance	...	9	...	...	...	91	...	...	...	...	...	...	...	...
MS40	Sulfate globules	...	...	...	...	...	5	...	...	...	49	38	...	8	...
MS41	Sulfate globules	...	...	...	...	...	6	...	...	...	59	25	...	12	...
MS42	Sulfate globules	...	...	...	...	...	...	...	...	...	48	52	...	...	...
MS43	Sulfate globules	...	...	...	...	...	4	...	...	...	62	28	...	6	...
MS44	Wall needles, filaments	...	36	...	...	4	8	...	...	...	44	9	...	...	...
MS45	Crust from evaporated cave water	...	...	...	...	...	...	...	...	...	36	10	...	...	54

gypsum (μ=5 %) and also hexahydrite (μ = 8.7 %). A representative diffractogram for one of the samples (sample MS 18b in Table 1) is shown in Figure 10.

When viewed under SEM, the blodite appears as euhedral tabular crystals (Fig. 11). The accompanying EDX spectrum is consistent with expected energy peaks for blodite. Thenardite is also visible in SEM images, both as bipyramidal and needle shaped forms (Fig. 12).

None of the samples contained the hydrated sulfate mirabilite. To determine whether mirabilite is stable under the temperature and RH conditions in the cave, 15 temperature and relative humidity readings were taken throughout the cave. Air temperature varied from 16.5 °C to 18.6 °C (mean= 17 °C) and RH varied from 45 % to 57 % (mean = 48 %). Figure 179(B) in Hill and Forti (1997) plots the stability of mirabilite and thenardite as a function of temperature and RH. This figure is reproduced in Figure 13 with a data point added for the mean observed conditions in Rock Pigeon Cave (blue square) where in that cave environment, thenardite, but not mirabilite, was found to be stable.

B. Subaqueous white deposits

Subaqueous deposits have been observed in the seasonal evaporation of saline lakes in Spain, Turkey, and elsewhere (del Buey et. al., 2021; Cabestrero, O. et. al., 2018; Mees, F. et. al., 2011; Sonmez, I., 2010; Mutlu, H. et. al., 1999; Sonnenfeld, P., 2003). These papers describe conditions under which sulfate minerals, e.g., blodite, thenardite, epsomite, mirabilite, and gypsum nucleate subaqueously as brines in saline and hypersaline lakes evaporate. Similar deposits have been observed in Rock Pigeon Cave where, in isolated evaporating pools, rounded, cruciform shaped white material has been observed both above and below pool level (Fig. 14). In this figure, the subaqueous parts of these deposits are seen where the color changes from white to gray.

Although the appearance of this material is the same as the globular precipitates seen just above water level, as illustrated in Figures 8 and 9, it was only observed once, in September, 2020, during a drought and when no surface water entered the cave and isolated pools in the cave were evaporating. Although observed, samples under these conditions were not taken.

Sulfate minerals that nucleate subaqueously in evaporating playas occur in brines having salinities of 160 to 340 g L^{-1} (Cabestrero, O. et. al., 2018). However, the salinity of pool water samples taken in Rock Pigeon Cave, measured when water was flowing through the cave, was only 4 g L^{-1}. Pool water salinity under evaporative conditions when the sub-

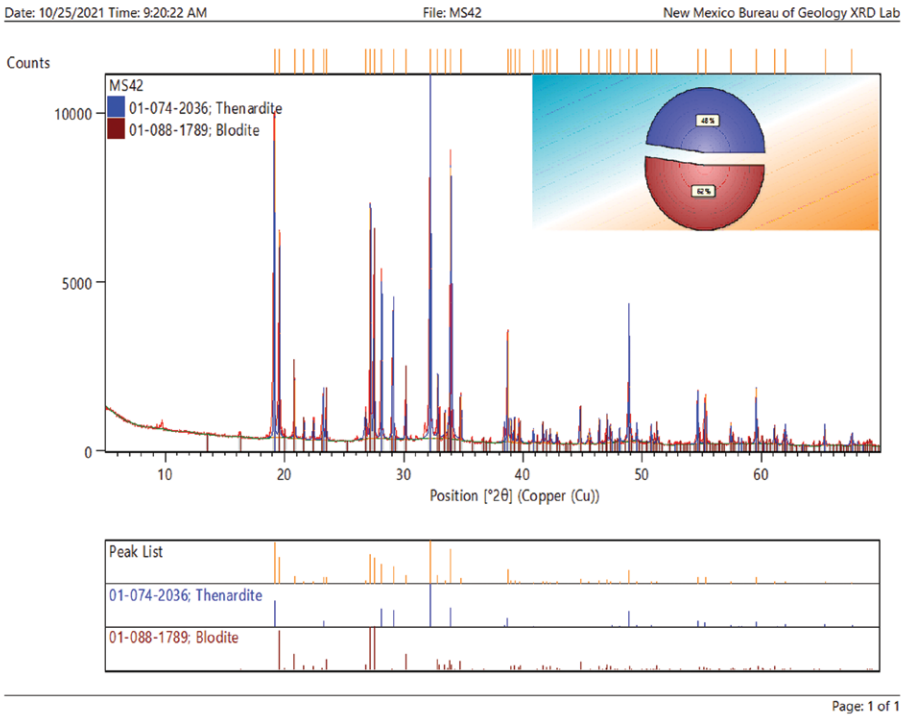

Figure 10. Diffractogram for water-level globular precipitates (sample MS42).

aqueous deposits exist has not been measured since these conditions were only seen once, during drought.

C. Coatings on shale

A prominent 3-5 mm thick coating on damp, partially decomposed shale slopes along passage walls is observed through much of the cave. Figure 15 shows this coating, up to a m above stream level and extending from stream level to a point where the disaggregating shale slope meets the dry vertical passage wall above. This may represent a high water mark for the cave stream. Figure 16 is a representative sample of the material, showing a partial crust. The composition of the crusts: half sulfates and carbonates, half quartz and clays, is a result of the difficulty of separating the sulfates from the underlying shale on which they are deposited. The composition of this material (sample MS28a) is listed in Table 1.

The sulfate component of the crusts is interpreted as being the result of deposition following evaporation of water in the cave stream and pools at and below the top of shale slopes.

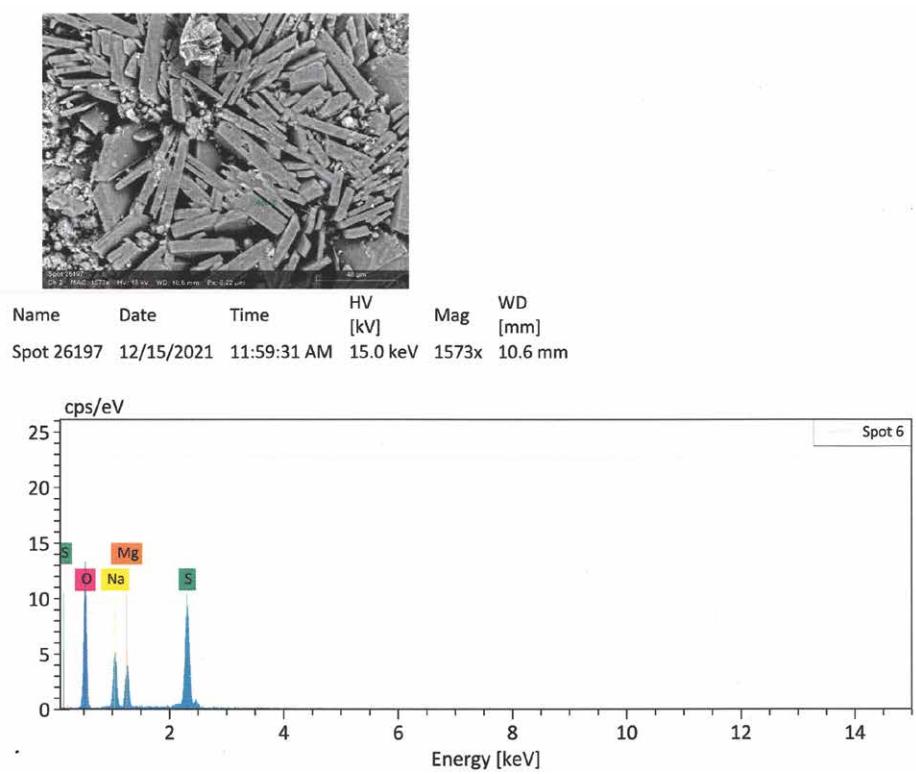

Figure 11. Tabular blodite with EDX spectrum.

D. Crusts on passage floors

The gully stream above the cave's upper entrance does not flow into the cave under drought conditions and the only water remaining in the cave under those conditions is seen as isolated pools. Under these conditions, last observed in September 2020, a dry crust covers the passage floor (Fig. 17).

Although samples of the dry floor crust were not taken, to simulate the formation of this crust, 500 ml of cave water was gradually evaporated until a smooth hard residue remained (Fig. 18).

The composition of this crust as per powder XRD (Fig. 19) is a mix of 38% thenardite, 10% blodite, and 54% konyaite ($Na_2Mg(SO_4)_2 \cdot 5H_2O$) with a distinctive 2θ 7.5 degree peak on the difractogram for the konyaite. Although thenardite and blodite were expected to be present, the presence of konyaite was not.

The hydrated double salt konyaite was first identified in 1984 (van

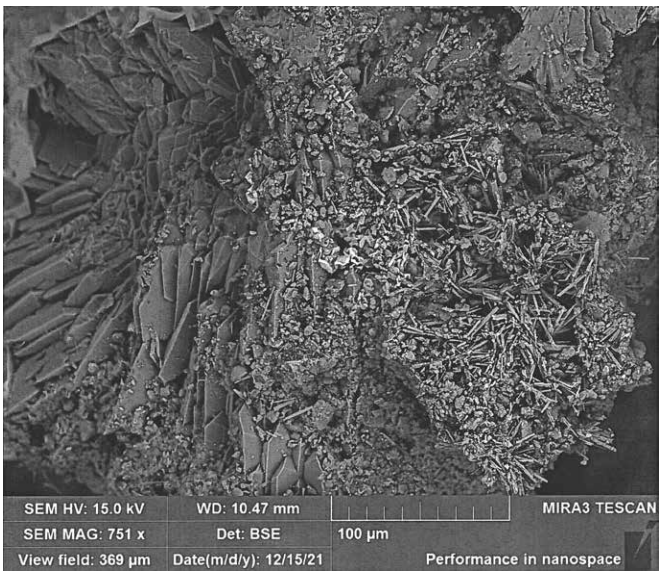

Figure 12. SEM image of bipyramidal thenardite (left) and needle thenardite (right).

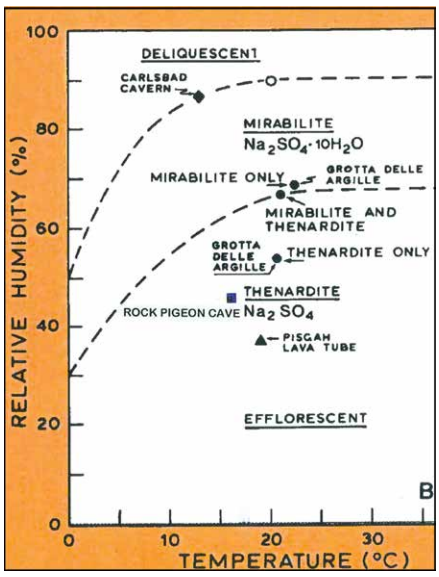

Figure 13. Stability of mirabilite and thenardite as a function of temperature and relative humidity (from Hill, C. and P. Forti, 1997, Fig. 179B).

Doesburg, J. et. al, 1982) and to date has only been documented in one other cave: Tausoare Cave in Romania (Onac, B.P., et. al., 2001). Whether konyaite will be present in crustal material in Rock Pigeon Cave, however, remains to be seen. Ambient conditions in the cave (17 °C, 45 % RH) differ from those in which the simulated crustal material was produced (20 °C, 25 % RH) and this may influence the crystallization of konyaite.

Figure 14. Subaqueous deposits (sulfates?) in cave pool.

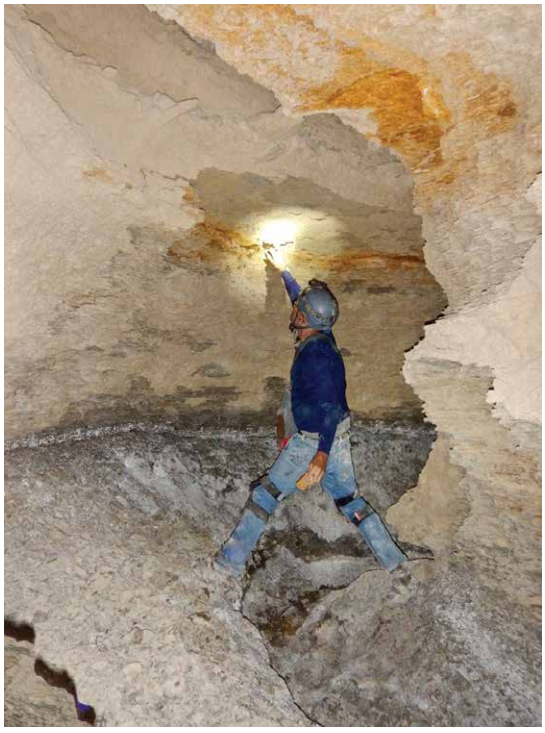

Figure 15. Sulfate coatings on damp shale slopes.

Figure 16. Sulfate coating on damp shale, 3cm diam.

E. Evaporites on passage walls

Needles, beards, and hair-like growths are observed on dry passage walls 1-2 m above the high water line in the cave (Fig. 20). These ephemeral minerals appear seasonally and are not the result of evaporation of sulfate-saturated water flowing through the cave.

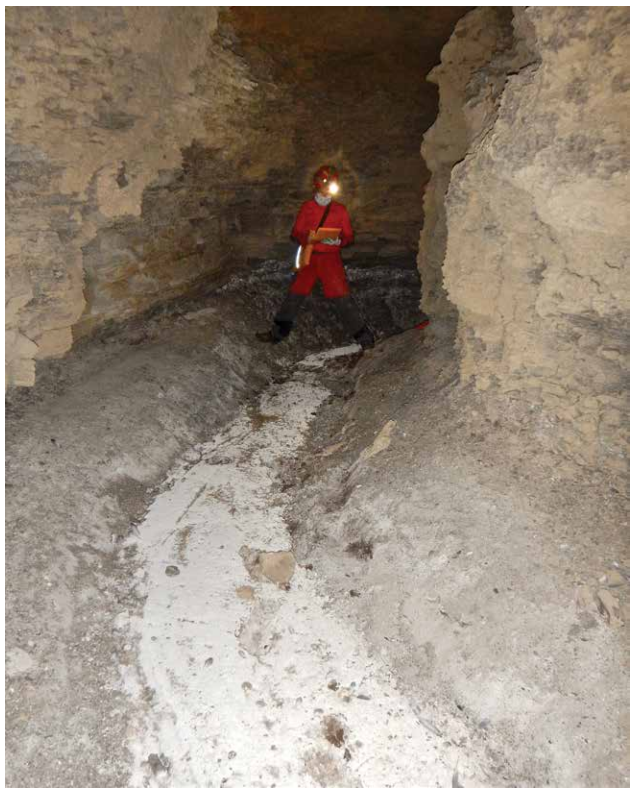

Figure 17. Dry crust on passage floor.

Figure 18. Simulated crust from evaporated cave stream water.

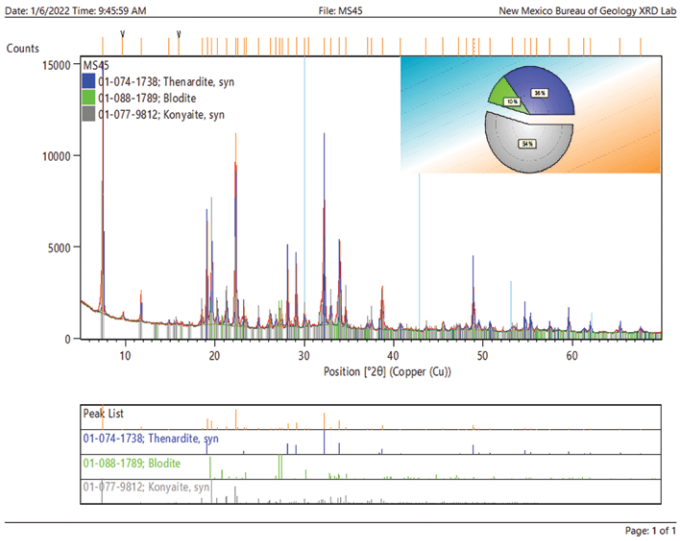

Figure 19. Diffractogram for crusted material derived from evaporated cave stream water.

Figure 20. Mixed sulfates on passage wall.

In a sample taken (MS33), the composition of this material was 16 % gypsum, 20 % thenardite, 16 % blodite and 5 % carbonates (calcite and dolomite). The remaining material, probably derived from the shale wall, consisted of 9 % quartz and 34 % clays: kaolinite and illite.

The needles develop as a result of evaporation of salt-rich fluids at the rock/air interface, producing salt efflorescences (De Waele, J. et.al., 2017). Precipitation-derived surface water within the shale reacts with pyrite to produce sulfate ions. These react with calcium ions derived from the carbonate component of the shale to produce gypsum.

Pressure created by hydration of the gypsum results in the extrusion of the needles from the passage walls. Cations in the clays in the shale, particularly Na^+ and Mg^+ derived from illite and montmorillonite, combine with SO_4^{2-} from in situ pyrite oxidation to produce the thenardite and blodite components of the observed mixed-sulfate needles.

CONCLUSIONS

This paper provides a preliminary assessment of the development and mineralogy of a relatively large vadose cave in a Cretaceous shale. Conditions required for this type of cave to develop involve a semi-arid to arid climate, the presence of swelling soils (montmorillonite) that enhance the movement of surface water through the regolith, pyrite in the shale to create sulfate ions, and sufficient calcite in the shale to allow it to react with the sulfate ions. The resulting gypsum wedges apart the shale beds and increases secondary porosity, allowing shale particles to be removed from initial openings, thus enlarging these openings on a granular basis via water flowing to a lower outlet, i.e., corrasion. Because the combination of these conditions occurs infrequently, vadose caves are rarely found in shale bedrock.

Ions from soluble salts found in Mancos soils are carried into these caves by entering streams. Evaporation of these salt-containing fluids on clay and rock surfaces result in the precipitation of sodium sulfate salts such as thenardite, blodite, and hexahydrite. Gypsum is also precipitated and being less soluble than the sulfates, comes out of solution first. As pools in the caves evaporate and ion concentrations increase to a point where saturation indeces become positive, these salts come out of solution, forming sulfate crusts on passage floors. The subaqueous precipitation of sulfates in cave pools is also observed, consistent with subaqueous crystallization seen in evaporating hypersaline lakes. Finally, following occasional precipitation events where meteoric water reaches the shale and reacts with minerals within, the slow evaporation of the resulting salt-rich water at the rock/air interface on passage walls results in efflorescences, primarily mixed-sulfate minerals.

ACKNOWLEDGEMENTS

The work described in this paper was carried out under a Research Agreement with the U.S. Bureau of Land Management office in Grand Junction, CO, administered by Dr. Madeline (Nikki) Grant-Hoffman. X-Ray diffraction analyses were conducted by the XRD laboratory at the New Mexico Bureau of Geology and Mineral Resources in Soccoro, NM. Laboratory Manager Kelsey McNamara provided valuable insights in interpreting the results obtained. Scanning electron microscopy and energy dispersive spectroscopy of shale and mineral samples was carried out at the Colorado School of Mines with Prof. John Spear and also with Prof. Katharina Pfaff at the CSM Automated Mineralogy Laboratory. Richard Heemskerk at the Environmental Isotope Laboratory, University of Waterloo, Ontario did the stable sulfur isotope analysis of the gypsum samples collected in caves. Valuable review comments on earlier drafts of this paper were made by Dr. Carleton Bern at the USGS Colorado Water Science Center in Lakewood, CO. Dr. Bern also carried out the simulation of cave water evaporation using PHREEQC. Ed LaRock provided field support and made insightful observations about structural geology and geologic setting both in the area and in the cave. Finally, photographic documentation of features in the cave and in survey and cartography were conducted by Bob Richards and Carol Vesely.

REFERENCES

Cabestrero, O., P. del Buey and M. Esther Sanz-Montrero, 2018, Biosedimentary and geochemical constraints on the precipitation of mineral crusts in shallow sulphate lakes: Sedimentary Geology v. 366, p. 32-46.

Cline, A.J., C. Spears, F. Mehaffey, et. al., 1967, Soil Survey Delta-Montrose Area, Colorado: U.S. Department of Agriculture Soil Conservation Service, 73 p.

De Waele, J., C. Carbone, L. Sanna, M. Vattano, E. Galli, F. Sauro and P. Forti, 2017, Secondary Minerals from Salt Caves in the Actama Desert (Chile): a hyperarid and hypersaline environment with potential analogies to the Martian subsurface: International Journal of Speleology: v. 46, p. 51-66.

del Buey, P., M. Esther Sanz-Montero, O. Braissant, O. Cabestrero, and P.T. Visscher, 2021, The role of microbial extracellular polymeric substances on formation of sulfate minerals and fibrous Mg-clays: Chemical Geology v. 581, p. 1-16. https://doi.org/10.1016/j.chemgeo.2021.120403

Elliott J. G., J.R. Herring, G.P. Ingersoll, J. Kosovich, and J. Fahy, 2007, Rainfall-Runoff and Erosion Data from the Mancos Shale Formation in the Gunnison Gorge National Conservation Area, Southwestern Colorado, 2003-2006: U.S. Geological Survey Open-File Report 2007-1002G, 68 p.

Evangelou, V. P., L. D. Whittig, and K. K. Tanji, 1984, Dissolved Mineral Salts Derived from Mancos Shale: Journal of Environmental Quality, v.13, issue 1, p.146-150.

Gu X, D. Rempe, W. Dietrich, A. Joshua West, T-C Lin, L. Jin, and S. Brantley, 2020, Chemical reactions, porosity, and microfracturing in shale during weathering: The effect of erosion rate: Geochimica et Cosmochimica Acta, v. 269, p. 63-100.

Hansen, W.R., 1971, Geologic Map of the Black Canyon of the Gunnison River and Vicinity, Western Colorado, U.S. Geological Survey Miscellaneous Geologic Investigations Map I-584, 2 sheets, scale 1:31,680.

Hill, C. and P. Forti, 1997, Cave Minerals of the World, 2nd Edition: Huntsville, Alabama, National Speleological Society, 463 p.

Kellogg, K., W. Hansen, K. Tucker, and D. Paco Van Sistine, 2004, Geologic Map Gunnison Gorge National Conservation Area, Delta and Montrose Counties, Colorado, U.S. Geological Survey Scientific Investigations Map 2825, scale 1:45 000, 1 sheet.

Miller, R.O., R. Gavlak, and D. Horneck, 2013, Soil, Plant and Water Reference Methods for the Western Region, Western Coordinating Committee on Nutrient Management, WERA-103.

Medville, D., 2018, Speleogenesis of Caves in a Cretaceous Shale: Bighorn Basin, Wyoming: Journal of Cave and Karst Studies, v. 80, p. 66-80.

Mees, F., C. Castaneda, J. Herrero, E. Van Ranst, 2011, Bloedite sedimentation in a seasonally dry saline lake (Salada Mediana, Spain): Sedimentary Geology v. 238 issues 1-2, p. 106-115.

Merkler, D., N. McMillan, and B. Buck, 2006, Salt Mineralogy of Las Vegas Wash, Nevada: Morphology and Subsurface Evaporation: Soil Science Society of America Journal, v. 70, p. 1639-1651.

Noe, D.C., J. L. White, and M. Nelson, 2015, Geologic Map of the North Delta quadrangle, Delta County, Colorado: Colorado Geological Survey Open File Report 15-09, scale 1: 24 000, 1 sheet, 9 p. text.

Noe, D.C., M.L. Morgan, P.R. Hanson, and S. M. Keller, 2007, Geologic Map of the Montrose East Quadrangle, Montrose County, Colorado: Colorado Geological Survey Open-File Report 07-02, scale 1: 24 000, 2 sheets, 101p.

Nordstrom, D.K., 1982, Aqueous Pyrite Oxidation and the Consequent Formation of Secondary Iron Minerals. Chapter 3 *in* Kittrick, A., D.S. Fanning, and L.R. Hossner, eds., Acid Sulfate Weathering, v. 10, Soil Science Society of America, p. 56-77

Onac, B. P., W. B. White, and I. Viehmann, 2001, Leonite [$K_2Mg(SO_4)_2 \cdot 4H_2O$], konyaite [$Na_2Mg(SO_4)_2 \cdot 5H_2O$] and syngenite [$K_2Ca(SO_4)_2 \cdot H_2O$] from Tausoare Cave, Rodnei Mts., Romania. Mineralogical Magazine, February 2001, v. 65(1), p. 103-109.

Onac, B. P. and P. Forti, 2011, Minerogenetic mechanisms occurring in the cave environment: an overview: International Journal of Speleology, v. 40, p. 79-98.

Palmer, A., 2007, Cave Geology: Dayton, Ohio, Cave Books, 454p.

Parkhurst, D.L. and C.A.J. Appelo, 1999, User's Guide to PHREEQC (version 2); A Computer Program for Speciation, Batch-Reaction, One-Dimensional Transport, and Inverse Geochemical Calculations: U.S. Geological Survey Water Resources Investigation Report 99-4259, 312p.

Penner, E., W.J. Eden, and P.E. Grattan-Bellew, 1972, Expansion of Pyritic Shales: Canadian Building Digest, Division of Building Research, National Research Council Canada, 6p.

Sonmez, I., 2010, Actual Bloedite mineral Precipitation in a Seasonal Lake in Cankiri-Corum Basin: Bulletin of the Mineral Research and Exploration, v. 140, p. 35-53.

Sonnenfeld, P., 2003, Evaporites, *in* R. A. Meyers, ed., Encyclopedia of Physical Science and Technology (third edition): San Diego, California, Academic Press, p. 653-671.

Tuttle, M.L., J. Fahy, J. Elliott, R. Grauch and L. Stillings, 2014, Contaminants from Cretaceous black shale I. Natural weathering processes controlling contaminant cycling on Mancos Shale, southwestern United States, with emphasis on salinity and selenium: Applied Geochemistry v. 46. p. 57-71. https://doi.org/10.1016/j.apgeochem.2013.12.010

U.S. Department of Agriculture, 2018, Final Watershed Plan and Environmental Assessment for the Lower Gunnison Project: Figure 3.2-1.

U.S. Department of Energy, 2011, Natural Contamination from the Mancos Shale: Report ESL-RPT-2011-1, 78 p.

van Doesburg, J., L. Vergouwen, van der Plas, L., 1982. Konyaite, $Na_2Mg(SO_4)_2 \cdot 5H_2O$, a new mineral from the Great Konya Basin, Turkey: American Mineralogist, v. 67, p. 1035-1038.

White, J.L., R. MacLean and C.J. Carroll, 2014, Geologic Map of the Whitewater Quadrangle Mesa County, Colorado, Colorado Geological Survey Open File Report 14-09, scale 1:24 000, 2 sheets, 42 p text.

White, J.L. and C. Greenman, 2008, Collapsible Soils in Colorado: Denver, Colorado, Colorado Geologic Survey Publication EG-14, 108 p.

Whittig, L. D., A. E. Deyo and K. K. Tanji, 1982, Evaporite mineral species in Mancos Shale and Salt Efflorescence, Upper Colorado River Basin: Soil Science of America Journal, v. 46, issue 3, p. 645-651.

GUIDE TO AUTHORS

The *Journal of Cave and Karst Studies* is a multidisciplinary journal devoted to cave and karst research. The *Journal* is seeking original, unpublished manuscripts concerning the scientific study of caves or other karst features. Authors do not need to be members of the National Speleological Society, but preference is given to manuscripts of importance to North American speleology.

LANGUAGES: The *Journal of Cave and Karst Studies* uses American-style English as its standard language and spelling style, with the exception of allowing a second abstract in another language when room allows. In the case of proper names, the *Journal* tries to accommodate other spellings and punctuation styles. In cases where the Editor-in-Chief finds it appropriate to use non-English words outside of proper names (generally where no equivalent English word exist), the *Journal* italicizes them. However, the common abbreviations i.e., e.g., et al., and etc. should appear in roman text. Authors are encouraged to write for our combined professional and amateur readerships

CONTENT: Each paper will contain a title with the authors' names and addresses, an abstract, and the text of the paper, including a summary or conclusions section. Acknowledgments and references follow the text. Manuscripts should be limited to 6,000 words and no more than 10 figures and 5 tables. Larger manuscripts may be considered, but the *Journal* reserves the right to charge processing fees for larger submissions.

ABSTRACTS: An abstract stating the essential points and results must accompany all articles. An abstract is a summary, not a promise of what topics are covered in the paper.

STYLE: The *Journal* consults The Chicago Manual of Style on most general style issues.

REFERENCES: In the text, references to previously published work should be followed by the relevant author's name and date (and page number, when appropriate) in brackets. All cited references are alphabetical at the end of the manuscript with senior author's last name first, followed by date of publication, title, publisher, volume, and page numbers. Geological Society of America format should be used (see http://www.geosociety.org/documents/gsa/pubs/GSA_RefGuide_Examples.pdf). Please do not abbreviate periodical titles. Web references are acceptable when deemed appropriate. The references should follow the style of: Author (or publisher), year, Webpage title: Publisher (if a specific author is available), full URL (e.g., http://www.usgs.gov/citguide.html), and the date the website was accessed in brackets. If there are specific authors given, use their name and list the responsible organization as publisher. Because of the ephemeral nature of websites, please provide the specific date. Citations within the text should read: (Author, Year).

SUBMISSION: Manuscripts are to be submitted via the PeerTrack submission system at http://www.edmgr.com/jcks/. Instructions are provided at that address. At your first visit, you will be prompted to establish a login and password, after which you will enter information about your manuscript and upload your manuscript, tables, and figure files. Manuscript files can be uploaded as DOC, WPD, RTF, TXT, or LaTeX. Note: LaTeX files should not use any unusual style files; a LaTeX template and BiBTeX file may be obtained from the Editor-in-Chief. Table files can be uploaded as DOC, WPD, RTF, TXT, or LaTeX files and figure files can be uploaded as TIFF, AI, EPS, or CDR files. Extensive supporting data may be placed on the Journal's website as supplemental material at the discretion of the Editor-in-Chief. The data that are used within a paper must be made available upon request. Authors may be required to provide supporting data in a fundamental format, such as ASCII for text data or comma-delimited ASCII for tabular data.

DISCUSSIONS: Critical discussions of papers previously published in the *Journal* are welcome. Authors will be given an opportunity to reply. Discussions and replies must be limited to a maximum of 1000 words and discussions will be subject to review before publication. Discussions must be within 6 months after the original article appears.

MEASUREMENTS: All measurements will be in Systeme Internationale (metric) except when quoting historical references. Other units will be allowed where necessary if placed in parentheses and following the SI units.

FIGURES: Figures and lettering must be neat and legible. Figure captions should be on a separate sheet of paper and not within the figure. Figures should be numbered in sequence and referred to in the text by inserting (Fig. x). Most figures will be reduced, hence the lettering should be large. Photographs must be sharp and high contrast. Figures must have a minimum resolution of 300 dpi for acceptance. Please do not submit JPEG images.

TABLES: See http://caves.org/pub/journal/PDF/Tables.pdf to get guidelines for table layout.

COPYRIGHT AND AUTHOR'S RESPONSIBILITIES: It is the author's responsibility to clear any copyright or acknowledgement matters concerning text, tables, or figures used. Authors should also ensure adequate attention to sensitive or legal issues such as land owner and land manager concerns or policies and cave location disclosures.

PROCESS: All submitted manuscripts are sent out to at least two experts in the field. Reviewed manuscripts are then returned to the author for consideration of the referees' remarks and revision, where appropriate. Revised manuscripts are returned to the appropriate Associate Editor who then recommends acceptance or rejection. The Editor-in-Chief makes final decisions regarding publication. Upon acceptance, the senior author will be sent one set of PDF proofs for review. Examine the current issue for more information about the format used.

Journal of Cave and Karst Studies

Volume 85 Numbers 3-4 December 2023

CONTENTS